Naval Research Laboratory

Stennis Space Center, MS 39529-5004

NRL/MR/7320--10-9205

Validation Test Report for the ADvanced CIRCulation Model (ADCIRC) v45.11

Cheryl Ann Blain

Ocean Dynamics and Prediction Branch
Oceanography Division

Robert S. Linzell

QinetiQ North America
Technology Solutions Group
Stennis Space Center, Mississippi

Philip Chu
Chris Massey

Ocean Dynamics and Prediction Branch
Oceanography Division

February 26, 2010

REPORT DOCUMENTATION PAGE

Form Approved
OMB No. 0704-0188

1. REPORT DATE *(DD-MM-YYYY)*	**2. REPORT TYPE**	**3. DATES COVERED** *(From - To)*
26-02-2010	Memorandum Report	

4. TITLE AND SUBTITLE

Validation Test Report for the ADvanced CIRCulation Model (ADCIRC) v45.11

5a. CONTRACT NUMBER

5b. GRANT NUMBER

5c. PROGRAM ELEMENT NUMBER
0602435N

6. AUTHOR(S)

Cheryl Ann Blain, Robert Linzell,* Philip Chu, and Chris Massey

5d. PROJECT NUMBER

5e. TASK NUMBER

5f. WORK UNIT NUMBER
73-6263-09-5

7. PERFORMING ORGANIZATION NAME(S) AND ADDRESS(ES)

Naval Research Laboratory
Oceanography Division
Stennis Space Center, MS 39529-5004

8. PERFORMING ORGANIZATION REPORT NUMBER

NRL/MR/7320--10-9205

9. SPONSORING / MONITORING AGENCY NAME(S) AND ADDRESS(ES)

Office of Naval Research
875 North Randolph Street
Arlington, VA 22203-1995

10. SPONSOR / MONITOR'S ACRONYM(S)

ONR

11. SPONSOR / MONITOR'S REPORT NUMBER(S)

12. DISTRIBUTION / AVAILABILITY STATEMENT

Approved for public release; distribution is unlimited.

13. SUPPLEMENTARY NOTES

*QinetiQ North America, Technology Solutions Group, Stennis Space Center, Mississippi 39529

14. ABSTRACT

The Validation Test Report for the ADvanced CIRCulation Model, ADCIRC, v45.11 addresses the prediction of barotropic 2D and 3D currents, water levels and inundation. Validation efforts address 1) the wetting and drying capability, 2) the prediction of surge, inundation and surge-induced currents, 3) the prediction of two- and three-dimensional currents and water levels in a bay, and 4) the prediction of three-dimensional tidal currents in the wake of an island. Lastly, a simulated real-time exercise with the model is conducted during the international sea trial, MREA07, and is used to evaluate the developed enabling software as well as the prediction of 2D barotropic currents. Generally, model predictions of evaluated products are reasonably accurate and realistic for truly barotropic applications. More work is needed to better assess the impact of boundary condition specification on predictive capability and to determine the model sensitivity to the 3D turbulence closure formulation and parameter selection.

15. SUBJECT TERMS

ADCIRC	Inundation	Currents	Finite elements	Delaware Bay	LaSpezia Bay
Storm surge	Tides	Barotropic dynamics	Hurricane Katrina	Rattray Island	MREA07

16. SECURITY CLASSIFICATION OF:			**17. LIMITATION OF ABSTRACT**	**18. NUMBER OF PAGES**	**19a. NAME OF RESPONSIBLE PERSON**
a. REPORT	**b. ABSTRACT**	**c. THIS PAGE**			Cheryl Ann Blain
Unclassified	Unclassified	Unclassified	UL	112	**19b. TELEPHONE NUMBER** *(include area code)* (228) 688-5450

Standard Form 298 (Rev. 8-98)
Prescribed by ANSI Std. Z39.18

TABLE OF CONTENTS

1. Summary of ADCIRC, v45.11, Features

The Advanced CIRCulation Model has seen tremendous evolution since the last transitioned version, v36.01. The code has been translated into the FORTRAN 90 language standard and the two-dimensional and three-dimensional codes, once separate, are now contained within a single unified code. The 2D and 3D unified code is completely parallelized using the MPI protocol and *metis* domain decomposition. The code structure itself is modular with individual subroutines containing global dimensioning, cold and hotstart initialization, parameter specification, wind forcing, harmonic analysis, three-dimensional calculations, and the main time stepping loop. Furthermore, the code has become multi-algorithmic with options for selecting various implementations of the conservative or non-conservative Generalized Wave Continuity Equation (GWCE) and/or momentum equation formulations.

Other notable additions to the ADCIRC v45.11 model code are options to use a predictor-corrector time stepping algorithm, a spatially varying GWCE parameter (Tau0), a nonlinear hybrid bottom friction relationship and a wetting and drying algorithm has been significantly improved. Under appropriate dynamical conditions the predictor-corrector time stepping option allows time steps up to ten times larger than the default explicit time stepping, thereby decreasing the computational cost of a particular simulation. Significant improvements to the wetting/drying capability, including the option of a nonlinear hybrid bottom friction relationship, have been implemented to improve realism, performance and stability of the model when wetting and drying are important. Options to specify a spatially varying GWCE parameter (Tau0) have resulted in better mass conservation and stability for highly advective flows.

A complete description of the theoretical basis for ADCIRC v44.xx and above is given in http://adcirc.org/adcirc_theory_2004_12_08.pdf. The online User's manual for v45.11 is found at http://adcirc.org/document/ADCIRC_title_page.html. Below are detailed descriptions of the latest ADCIRC code features including wetting and drying, a hybrid nonlinear bottom friction relationship, predictor-corrector time stepping and the spatially variable GWCE parameter specification.

a. The Wetting and Drying Algorithm

The wetting and drying scheme is based on a simplified one-dimensional momentum balance between gravity and pressure which accounts for the physics of the flow, along with some empirical rules to help ensure stability. Based on some predetermined criteria (to be discussed later), the wetting and drying ultimately involves classifying elements as either wet, which means there is a sufficient amount of water over that element, or dry meaning that element does not have enough water over it to be a part of the active computational area.

When wetting and drying of elements is to be used, ADCIRC initializes the elevation at all nodes such that the total water depth, H_j at node j, is greater than or equal to H_0, the minimum specified water depth. The total water depth, H_j, at node j, is defined to be the bathymetric depth, z_j relative to mean sea level (MSL) plus the sea surface elevation, η_j relative to MSL, see f igure 1.1.

Manuscript approved September 18, 2009.

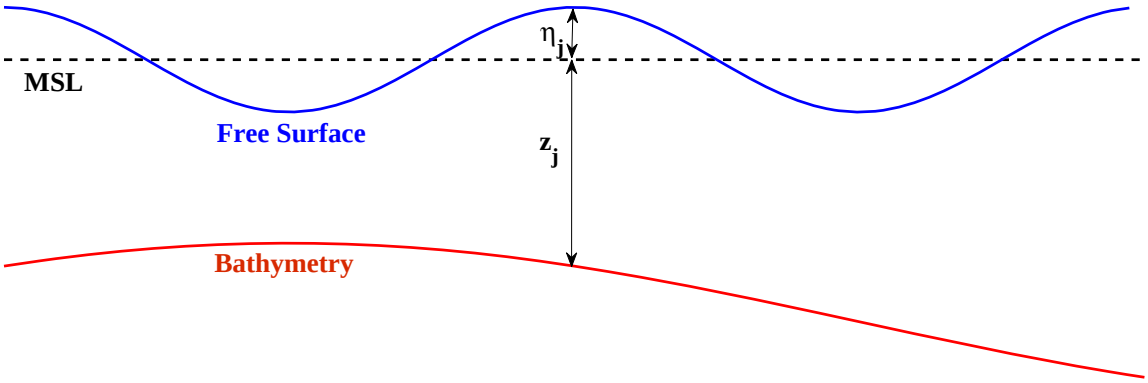

Figure 1.1 Profile of bathymetry, *z*, and free surface elevation, η, relative to mean sea level (MSL).

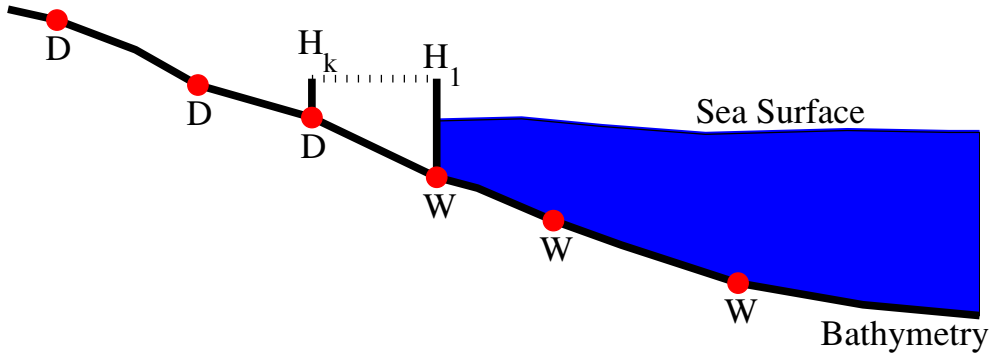

Figure 1.2. Wet/Dry interface acts as a no normal flow barrier. Red dots marked with a ``D'' indicate dry nodes and red dots marked with a ``W'' indicate wet nodes.

The wetting and drying algorithm can be broken down into two main components, the first is a drying phase and the second is a wetting phase. The drying phase is based on nodal criteria. During this phase, the total water height, *H*, at all active nodes are examined to determine if there is enough water present for them to stay active, if not, those nodes are dried, see figure 1.3a The threshold value between a classification of wet or dry, is based on a total water depth greater than or equal to H_0. If the total water depth is at or below H_0 then

the node is classified as dry. Furthermore, if the total water depth at the now dry node has fallen below an absolute minimum water depth, H_{absm}. = $0.8H_0$, then elevations are reset such that the total water height is H_{absm}. Thus newly dried nodes will have a total water depth that is bounded below by H_{absm} and above by H_0. This variance in water height can explain some of the asymmetry observed during re-wetting phases along a front. This will be elaborated on in the discussion of results (Section 3).

The second phase of the wetting and drying algorithm is the wetting phase, see figure 1.3b for a flow chart illustration. It is in this phase that we evaluate the simplified momentum balance between gravity and pressure,

$$gH\frac{\partial \eta}{\partial x} = \tau_b = C_D v \tag{1}$$

where g is acceleration due to gravity. Upon rearrangement of (1) we get

$$v = \left(\frac{g}{\tau_k}\right)\frac{\partial \eta}{\partial x} \tag{2}$$

where $\tau_k = \frac{C_D}{H}$. We will refer to τ_k as a bottom stress coefficient.

In the wetting phase of the wetting and drying algorithm, instead of individual nodes being considered, dry elements are examined. An element is considered wet only if all its nodes are wet. All dry elements that have exactly two wet nodes are examined to determine if they should become wet and thus force their one dry node to become wet. Let's assume that we have an element with two wet nodes, label them 1 and 2 and only one dry node, label it k. Before wetting can occur, the total water column height at the two wet nodes must be greater than or equal to $H_{off} = 1.2H_o$. Using the higher value for wetting than for drying reduces the chances of re-wetting nodes that have just dried, which could result in instabilities due to nodes turning on and off. Let us assume that both of the wet nodes meet this criterion. Now the simplified momentum balance is employed to determine if there is enough water to wet the element. First the wet node with the largest elevation will be used in the computation, without loss of generality assume it is local node number one, H_1. The velocity that would result in the water moving from node 1 to node k is computed using a discrete form of equation (2),

$$v_{wet} = g\left(\frac{\Delta \eta}{\Delta x}\right)\frac{1}{\tau_{kwet}} \tag{3}$$

with $\Delta\eta = \left(\eta_1 - \eta_k\right)$, Δx the distance between node 1 and k and a bottom stress coefficient, τ_{kwet}, computed using either a quadratic or hybrid nonlinear bottom friction relationship for C_D with the velocity set at the prescribed minimal velocity allowed, $v = v_{\min}$, and $H = H_1$.

If $v_{wet} \geq v_{\min}$ then the element is reclassified as wet and is added to the computational domain. Notice that the simplified momentum balance does not take into account any directionality of flow. Thus, one could (and does) have cases where the flow is being forced toward one direction and wetting is occurring in another direction(s). We will see evidence of this in the first case study presented in Section 3.

There are a few additional empirical rules that make up the wetting and drying algorithm which deal mostly with weir overtopping. These rules are not effected by H_o and $v_{\min}$ and thus will not be discussed here.

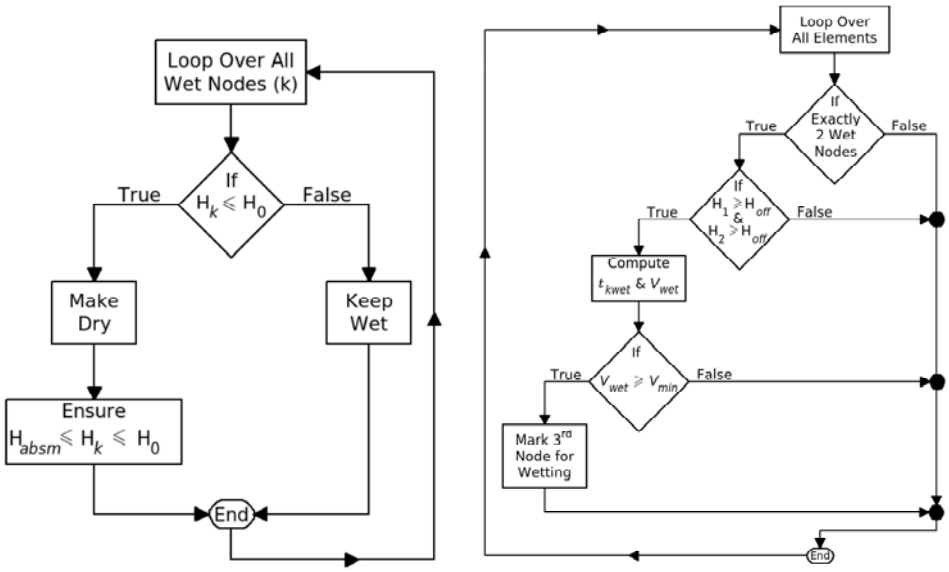

Figure 1.3. Decision tree for (a) drying a wet node and (b) wetting a dry element.

When dry elements are made wet, the water required to fill that element is just added to the overall water mass in the active computational area. Likewise, when a wet element is made dry, whatever amount of water was left in the now dry element is just removed from the total water mass. This has immediate negative consequences when coupling ADCIRC solutions with wetting and drying to a set of transport equations. Some might muse that since many of the domains have an open boundary, e.g., the open ocean or a river, that is actively forcing the simulation, then how important is accounting for mass balance? The answer depends on the application. If one primarily interested in high water mark values from a hurricane storm surge, such mass imbalances would not be important. But for modeling small-scale non-extreme events, such as tidal flooding and drying, the lack of mass conservation may be detrimental especially when transport processes are of great importance. Furthermore, as we will see in the cases studies presented in Section 4 the sudden addition or subtraction of water mass during the solution process can produce near shocks in the velocity solutions. These shocks can be strong enough to cause model instabilities so severe as to result in premature model termination.

Practically, wetting and drying within the ADCIRC model is invoked with a parameter specification of NOLIFA, the parameter controlling the nonlinear finite amplitude terms, equal to 2 or 3. Under wetting and drying values of the minimum water depth, H_o, represent the nominal water depth at a node for it to be considered dry, typically 0.01 – 0.1 m. Additional parameters, NODEDRYMIN, NODEWETMIN, and VELMIN, are also required to activate wetting and drying. See the online user's manual for details on their specification (http://adcirc.org/document/ADCIRC_title_page.html) and see Section 3a for a discussion of the sensitivity of these parameters on the performance of the wetting and drying

algorithm.

b. Nonlinear Bottom Friction Relationships

Important to the physical wetting and drying process is the discrete representation of bottom friction. ADCIRC has an option for three types of bottom friction,

$$\tau_b = C_D v \tag{4}$$

defined by the choice of the drag coefficient C_D. The first choice for bottom friction coefficients is a linear friction relationship $C_D = c_f$, the second one is a quadratic friction relationship,

$$C_D = c_f \|v\| \tag{5}$$

and the third is a hybrid nonlinear bottom friction which results from using a depth dependent drag coefficient,

$$C_D = \max\left\{ C_{D\min}\left(1+\left(\frac{H_{break}}{H}\right)^{\theta}\right)^{\frac{\gamma}{\theta}}, 10^{-4} \right\} \tag{6}$$

where C_{Dmin} is either of the previously defined linear or quadratic friction drag coefficients, v is the water velocity, and H is the total water column depth. The depth dependent drag coefficient was introduced into ADCIRC in the report by Luettich and Westerink (1995) and is discussed in detail in that report. In brief, when in deep water, $H > H_{break}$, the drag coefficient approaches C_{Dmin}, the standard linear or quadratic drag coefficient relationships. However, when in shallow water, $H < H_{break}$, C_D approaches $C_{D\min}\left(H_{break}/H\right)^{\gamma}$. According to Luettich and Westerink (1995) the exponent θ determines how rapidly C_D approaches each asymptotic limit, while the exponent γ determines the rate at which the friction coefficient increases as the water depth decreases. Using the hybrid nonlinear bottom friction case when wetting and drying means that the friction coefficients will be higher than those computed when using the standard linear or quadratic option. The suggested default values for ADCIRC's hybrid nonlinear bottom friction are $H_{break} = 2m$, θ =10, γ = 1.3333, and c_f = 0.0030.

The choice of nonlinear bottom friction is determined by the value of NOLIBF in the *fort.15* parameter file. NOLIBF = 1 results in the standard nonlinear quadratic friction law, equation (5), while NOLIBF = 2 invokes the hybrid nonlinear bottom friction formulation of equation (6).

c. Predictor-Corrector Time Stepping

Currently, non-linear applications with ADCIRC have stability issues unless a severe Courant number restriction is imposed. The Courant number is defined as

$$C_\tau = \frac{c\Delta t}{\Delta x} \tag{7}$$

where $c = \sqrt{gh}$ is the linear wave celerity, Δx is minimum node spacing and Δt is the time step. In practice, we have found that for deep ocean flows, a practical upper bound of the Courant number (C_r) is 0.5 in order to maintain stability; however, an even tighter constraint

(e.g. $C_r << 0.1$) must be imposed if the simulation includes barrier islands, constricted inlets, or wetting and drying of near-shore elements. In order to relax this restriction, an alternative time-marching procedure was proposed that treats the non-linear terms implicitly (Kolar et al., 1998).

Within the standard ADCIRC model semi-implicit time marching algorithm, linear terms are evaluated implicitly and the non-linear terms explicitly. At the past and present time levels in ADCIRC, elevation and velocity values are known (either from initial conditions or previous calculations). The original algorithm takes the elevation and velocity values for the past ($k-1$) and the present (k) and uses them to calculate the values for the future ($k+1$) time level for the linear terms. However, the non-linear terms are evaluated using only the elevation and velocity values at the present time level (k). Kolar et al. (1998) hypothesized that the stability constraint stems primarily from this explicit evaluation of non-linear terms. A predictor–corrector time-marching algorithm is introduced to evaluate the non-linear terms implicitly. The predictor stage, which is equivalent to the original algorithm, evaluates the non-linear terms using values from the present. Predicted future values, called $k*$, and the already-known present (k) and past ($k-1$) values are then used to obtain corrected values for the future ($k+1$) time level. The corrector stage can be repeated as many times as necessary until convergence. In all applications to date, a single iteration of the corrector stage appears to be sufficient.

Through the use of time weight coefficients, users have the option to distribute the relative contribution of the non-linear terms over the three time levels. Comprehensive 1D studies by Dresback and Kolar (2001) and accompanying 2D studies (Dresback et al. 2004) have shown that optimal coefficients are problem dependent, but that near-optimal results for any domain are found by centering the GWCE time weights at k (meaning that the time weights for the non-linear terms are weighted equally between $k+1$ (or $k*$), k, $k-1$) and centering the non- conservative momentum time weights at $k + ½$ (meaning that the terms are weighted equally between k and $k+1$ (or $k*$)). Practically, the predictor-corrector time marching is activated through the use of a negative value for the time step, DTDP.

d. Spatially Variable GWCE Parameter, Tau0

The Generalized Wave-Continuity equation (GWCE) formulation used in the ADCIRC model contains the parameter, τ_o or Tau0, that serves as a weighting between the primitive continuity and the wave portions of the GWCE equation (Kinnmark, 1996). A value for τ_o equal to zero results in a pure wave equation while a value of 1 for τ_o leads to the primitive continuity equation. The value selected for τ_o strikes a balance between stability and mass conservation. A pure primitive continuity formation ($\tau_o = 1$) results in an unstable solution whereas $\tau_o = 0$ leads to the greatest mass imbalance. ADCIRC now provides an option to specify spatially variable values of this weighting coefficient so as to minimize mass conservation issues in shallow water regions or in regions where wetting and drying is likely to occur.

Spatially variable values of τ_o are automatically determined and invoked using a flagged value for τ_o that is negative. Under the spatially variable τ_o option, the value is specified as follows:

$$\text{Depth} \geq 10.0,\ \tau_o = 0.005$$

$$\text{Depth} < 10.0,\ \tau_o = 0.020$$

This approach leads to smaller mass errors in the shallower waters while maintaining stability over deeper waters.

2. Testing Strategy

Objectives of an ADCIRC, v45.11, model application are to represent two-dimensional and three-dimensional currents, water levels and inundation extent under barotropic dynamical conditions in coastal regions. Barotropic dynamics are present when the density-driven component of the flow is minimal or non-dominant. There are many circumstances in the coastal ocean wherein barotropic conditions prevail.

The validation test cases selected aim to span the range of possible applications of the ADCIRC model under these circumstances in order to evaluate the model's ability to predict realistic and accurate coastal dynamics. Furthermore, many of the test cases are identified with established or published benchmark test cases. In most instances field measurements are available and descriptions of the test cases can be found in the literature. Table 1 presents the matrix of validation test cases and the component of the barotropic flow under evaluation.

Table 1. Description of the Validation Test Cases for ADCIRC v45.11.

Test Case	Testing Parameters				
	Physics	Elevation	Wetting/Drying	Currents	Dimensionality
Idealized Beaches	inundation	✓	✓		**2D**
Hurricane Katrina	storm surge, inundation	✓	✓	✓	**2D**
Delaware Bay	tides and winds	✓		✓	**2D** and **3D**
Rattray Island	tides			✓	**3D**
MREA07	Software	✓		✓	**2D** and **3D**

3. Validation Test Results – Wetting and Drying

a. Parameter Sensitivity Analysis

To gain a greater understanding of how the control parameters H_o and $v_{\min}$ effect the wetting and drying process, the simplified momentum, equation (3), is analyzed through a series of experiments.

Recall that the discrete wetting velocity, given in equation (3), must be greater than or equal to the minimum velocity set by the user, $v_{wet} \geq v_{\min}$, in order for wetting to occur. For simplification, the standard nonlinear bottom friction relation (4) is assumed. This assumption will not alter the main analysis shown below. To determine the relational effects that $v_{\min}$ has on v_{wet} we differentiate equation (3) with respect to $v_{\min}$,

$$\frac{\partial v_{wet}}{\partial v_{\min}} = g\left(\frac{\Delta\eta}{\Delta x}\right)\left(\frac{-1}{v_{\min}\tau_{kwet}}\right) = -\frac{v_{wet}}{v_{\min}} \tag{8}$$

Since, $v_{wet} \geq 0$ and $v_{\min} > 0$, the negative sign on the derivative implies an inverse relationship between $v_{\min}$ and v_{wet}, namely, decreasing the value of $v_{\min}$ would have the effect of increasing the computed wetting velocity. The result is two paths to easier wetting of the element. First we have a smaller velocity threshold to overcome with a decreased value of $v_{\min}$. Secondly, the decrease in $v_{\min}$ also results in a higher computed velocity, as a result of the decreased drag coefficient from τ_{kwet}.

In order to determine the effects H_o has on v_{wet}, we will differentiate v_{wet} with respect to H_o. But first v_{wet} must be expressed in terms of H_o. Assume that we have a dry element that has two wet nodes and one dry node that has never been wet. This is to ensure that its total water depth is H_o. Without loss of generality, assume that local node number 1 is a wet node with the largest elevation and the dry node is local node number *k*. Since node 1 is wet we know that $H_1 \geq H_{absm} = 0.8H_0$ and in order for node *k* to be considered for wetting, $H_1 \geq H_{off} = 1.2H_0$. Furthermore, since node *k* is dry and has never been wet, it's elevation has been set such that $H_k = H_0$ therefore $\eta_k = H_0 - z_k$. In order for wetting to occur, $\Delta\eta = \eta_1 - \eta_k$ must be greater than 0, otherwise $v_{wet} = 0$. The elevation at local node 1 can be written as $\eta_1 = H_1 - z_k$ and H_1 can be written as $H_1 = H_0 + \delta_{h1}$, where δ_{h1} is a function of elevation, η. In fact, since $H_1 \geq 1.2H_0$ we know that $\delta_{h1} \geq 0.2H_0$. Combining these we can write $\eta_1 = H_0 + \delta_{h1} - z_1$, which we use in decomposing $\Delta\eta$, namely,

$$\Delta\eta = \eta_1 - \eta_k = \delta_{h1} + (z_k - z_1) \tag{9}$$

Again for the sake of convenience, a nonlinear bottom friction term is assumed instead of the hybrid nonlinear one. The discrete wetting velocity, equation (3) as

$$
\begin{aligned}
v_{wet} &= g\left(\frac{\Delta\eta}{\Delta x}\right)\frac{1}{\tau_{kwet}} \\
&= \frac{g}{\Delta x}\left(\eta_1 - \eta_k\right)\left(\frac{H_1}{c_f v_{\min}}\right) \\
&= \frac{g}{\Delta x c_f v_{\min}}\left(\delta_{h1} + (z_1 - z_k)\right)\left(H_0 + \delta_{h1}\right)
\end{aligned}
\tag{10}
$$

Now in order to determine the relational effects of H_o and v_{wet}, we differentiate equation (10) with respect to H_o to obtain

$$
\frac{\partial v_{wet}}{\partial H_0} = \frac{g}{\Delta x c_f v_{\min}}\left(\delta_{h1} + (z_k - z_1)\right) \tag{11}
$$

Now, by assumption, $\Delta\eta > 0$ so that $\delta_{h1} + (z_k - z_1) > 0$. Therefore the nonnegative derivative in equation (11) indicates a direct relationship between H_o and v_{wet}, namely increases in H_o mean increases in v_{wet}. Using the hybrid nonlinear bottom friction only alters the magnitude of the relationship, not the sign of the derivative. Overall an increase in H_o means that initially it is harder to wet an element, however, once the wetting begins, further wetting should be easier to obtain. A larger H_o requires water to pile up higher along the wet edge of the dry element, see figure 1.2. The resulting higher water level increases the forward velocity of the water because the change in elevation, $\Delta\eta$ expressed in equation (9) would also increase because $\delta_{h1} \geq 0.2H_0$.

The effects of H_o and $v_{\min}$ on the WAD algorithm's performance, can also be examined by considering the behavior of v_{wet} in terms of $\Delta\eta$. We will graphically show the effects that H_o and $v_{\min}$ have in terms of a required change in elevation, $\Delta\eta$, that is large enough to enable wetting to occur, i.e. so that $v_{wet} \geq v_{\min}$. This analysis is important when considering how to select appropriate values for the parameters H_o and $v_{\min}$ given a particular mesh and topography. The bathymetric gradients shown in equation (9) can be figured out in advance and the user can get an estimate of how much water has to build up before wetting can occur for given parameter choices.

For this analysis we assume that the total water depth at the wet neighbor node, $H_1 = 1.2H_o$, is the minimal allowable value for wetting to occur. For a mesh with a nodal spacing of 500*m* we show in figure 2.1a the contours of the required elevation changes for both the nonlinear and the hybrid nonlinear bottom friction cases. Notice that the slopes of the contours in figure 2.1a are both positive with respect to $v_{\min}$, however their curvature is different. The nonlinear bottom friction case has a positive curvature while the hybrid nonlinear bottom friction case has a negative curvature. This is pointed out to support our rational for performing the analysis using the less complicated nonlinear bottom friction case.

Furthermore, the nonlinear bottom friction case allows for smaller H_1 values, hence smaller H_o, than the hybrid nonlinear bottom friction case for the same required change in elevation. Thus as expected, the nonlinear bottom friction case allows wetting to occur more easily. Mesh element size acts as a linear multiplier on the elevation change required for wetting to occur. The smaller the mesh size the easier wetting can occur. This can be clearly observed in figure 2.1b where for the hybrid nonlinear bottom friction case, the effects that H_o and $v_{\min}$ have on a required elevation change of $0.1m$ are shown for meshes with element sizes of $\Delta x =$ 500, 250, and 125 m.

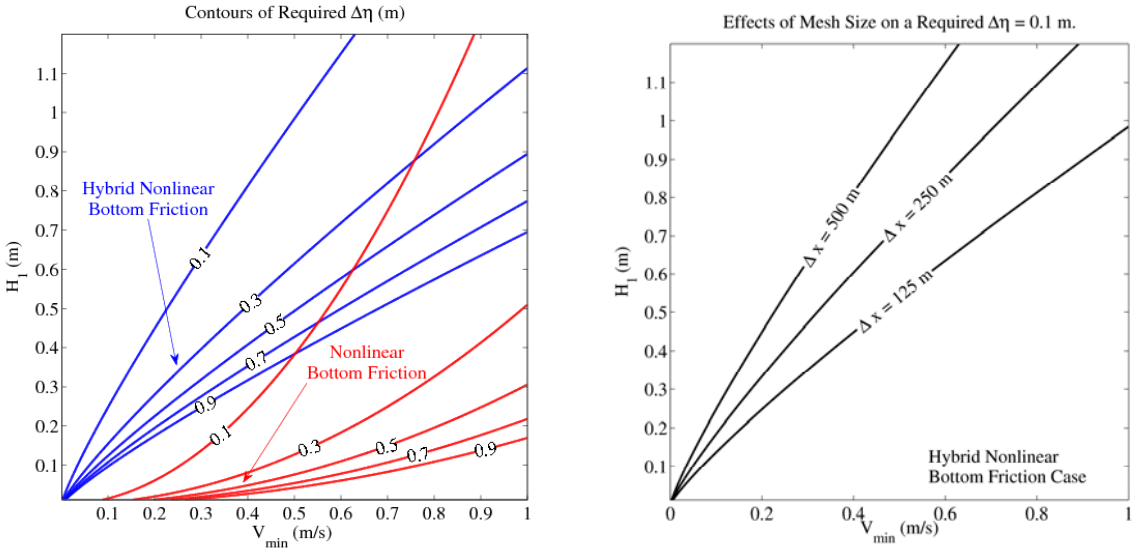

Figure 2.1: Wetting and drying parameter sensitivity analyses comparing (a) the required change in elevation relative to $v_{\min}$ and H_o using nonlinear bottom friction and hybrid nonlinear bottom friction relationships and (b) the effect that mesh spacing has on the required elevation change.

As was shown by Dietrich et al. (2004, 2006), an increasing value of the free parameter H_o also increases the mass balance errors. The impact that H_o has on global mass balance is addressed via a test case in two dimensions, the *Enclosed Circular Basin*, presented in Section 3.2.

For all wetting and drying test cases, the 2D depth integrated formulation of ADCIRC, version 45.11, is applied. The pertinent input parameter values (fort.15) are specified below. If the input values deviate from those listed here, the change will be noted under the description of each test problem. The ADCIRC model input file (fort.15) parameter specifications are:

IM = 0 - Model selection parameter
NOLIBF = 2 - Bottom friction term selection parameter
NOLIFA = 2 - Finite amplitude term selection parameter
NOLICA = 0 - Spatial derivative convective selection parameter
NOLICAT = 0 - Time derivative convective term selection parameter
NWP = 0 - Variable bottom friction and lateral viscosity option parameter
NCOR = 0 - Variable Coriolis in space option parameter
NTIP = 0 - Tidal potential option parameter
NWS = 2 - Wind stress and barometric pressure option parameter
NRAMP = 1 - Hyperbolic Tangent Ramp Function Option
TAU0 = -0.020 - Weighting factor in GWCE
0.35 0.30 0.35 = Time weighting factors for the GWCE equation
FFACTOR,HBREAK,FTHETA,FGAMMA = 0.0030 2.0 10 1.33333
ESL = 0.50 - Lateral eddy viscosity coefficient
CORI = 0.0 - Coriolis parameter

Setting IM = 0 enables a barotropic 2D depth integrated run using the original GWCE and momentum equation formulations. Setting NOLIBF = 2 enables the hybrid nonlinear bottom friction calculation. Setting NOLIFA = 2 enables the wetting and drying algorithm. Specifying NRAMP = 1 enables a hyperbolic tangent ramping function, see equation (12) that is used to ramp up the input values from an initial factor of zero to nearly 96 percent of the specified input by the end of the ramp duration, given by the input variable DRAMP.

$$RAMP = \tanh\left\{\left(2.0 * IT * DT / (865400. * DRAMP)\right)\right\} \tag{12}$$

where *IT*DT* is the elapsed time in seconds of the simulation, and *DRAMP* is the effective duration of the ramp given in days.

A complete description of these and all other ADCIRC input variables is given on the ADCIRC website, http://www.adcirc.org.

b. Enclosed Circular Basin

The enclosed circular basin of Xie et al. (2004) is used to examine the non-conservative nature of the ADCIRC wetting and drying algorithm. The physical domain is a 120*km* by 120*km* square with a circular basin of radius 30*km* located at the center, see figure 2.2a. The domain is discretized using structured right triangular elements formed by diagonally cutting uniform squares of size 600 meters. The bathymetry/topography set up is the same as in Xie et al. (2004) where the depth at the center of the bowl is 9.0 meters and decreases linearly to 1.0 meter at the land/sea interface along the rim of the bowl. The land elevations begin with a value of -0.25 meters at the rim and change linearly with a constant slope of -1/7500 to the exterior boundaries. The outer most boundaries were set to a mainland boundary type with no normal flow as an essential boundary condition and free tangential slip allowed. The same wind forcing as Xie et al. (2004) derived from a Holland (1980) axis-symmetric hurricane model were used to force the run. Note a correction to equation 11 in Xie et al. (2004) where the wind drag C_d coefficients should have been

$10^3 C_d = 0.62 + 1.56\left|\vec{V}_w\right|^{-1}$ for wind speeds $1 \le \left|\vec{V}_w\right| < 10\, m/s$. Wind fields were supplied every 30 minutes to ADCIRC for a period of 54 hours, see figure 2.2b for storm center locations relative to the computational domain. The simulation was for 54 hours using a 6 hour ramp period for the wind forcing and a time step of 5.0 seconds. A series of experiments is performed in which the wetting and drying control parameters H_o and $\nu_{\min}$ are varied. The values presented are for H_o = (0.1, 1.0, 5.0) meters and for $\nu_{\min}$ = 0.01, 0.05, 0.1, 0.2, 0.5, 1.0) meters per second.

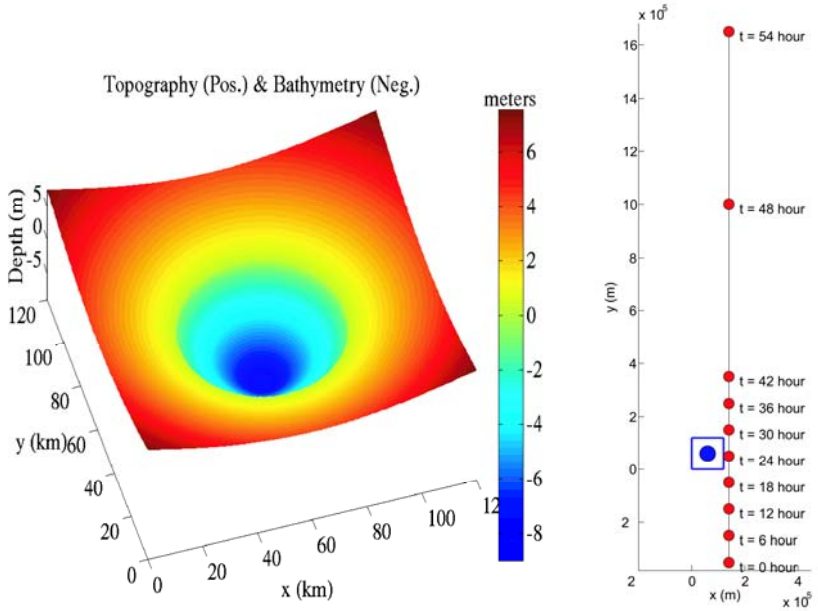

(a) (b)

Figure 2.2. The (a) topography/bathymetry of the enclosed circular basin and (b) the storm track locations, in red, relative to the computation domain shown in blue.

In figure 2.3, a series of contour plots showing the wet/dry interface for various values of $\nu_{\min}$ at times 18 hours, 24 hours, and 54 hours into the simulation (rows) and various H_o values (columns). In each of these images the original coastline of the basin is drawn as a frame of reference from which to view the progress of the wetting and drying front. The first two rows show the initial wetting phase of the simulation while the last image shows what should be a drying phase with all the water returning to the original basin under minimal winds. Examining the images at the 18 hour mark, we see that by increasing H_o the drying front, along the northeast border of the basin, moves further toward the bowl's center away from the original coastline. This is to be expected, due to the drying criteria of the WAD algorithm. The effects of H_o on the wetting front, along the southwest portion of the basin, are more complicated to analyze. For the smallest H_o, the wetting front is more diffuse and less advanced away from the bowl's center than the $H_o = 0.5m$ case. We

attribute this behavior to the fact that the smaller H_o allows the water to meander around the concentric rings of bathymetry more than higher values of H_o whose wetting fronts are more in line with the direction of the wind forcing. By comparing the contours at the 18 hour mark, for $H_o = 0.1m$ and $H_o = 1.0m$, we notice that for higher H_o, the wetting front takes longer to begin advancing. This is because higher H_o values require more water to build up behind the wetting front before allowing the wetting front to advance. At the 18 hour mark for the cases with $H_o = 1.0m$, the water levels are still building and have not started to propagate outside the basin. By examining the 24 hour mark for all H_o values, as well as the 18 hour mark for $H_o = 0.1m$ and $H_o = 0.5m$, we see that for increasing H_o values, that once the water begins to move, the wet/dry front moves further and is more focused in the direction towards which the winds are actually blowing. At the 54 hour mark, we again see that for increased H_o values, the faster the drying process acts. In fact for the smallest H_o value, there is still a large area of land that is inundated, even though the wind forcing is negligible. The case for $H_o = 1.0m$ and $V_{\min} = 0.2\,m/s$ at the 54 hour mark seems to have settled to an equilibrium solution outside the original basin, for which we do not have a clear explanation.

The effects of $v_{\min}$ on the wetting front can be seen clearly in the plot for $H_o = 0.1m$ at 24 hours, with the wetting front being further advanced for decreasing values of $v_{\min}$, as predicted by our previous analysis. Again, a smaller value of $v_{\min}$ results in a larger, more diffuse wetting front. This same effect is observed for the other H_o values at 24 hours and for the 18 hour mark with $H_o = 0.1m$ and $H_o = 0.5m$.

In figure 2.4 are shown the time series of elevation at three nodal points, whose locations are depicted in (a), for $H_o = 0.5m$ and $1.0m$ and for a fixed $v_{\min} = 0.05\,m/s$. When a node dries, the elevation solution is represented using a value of $0.0m$ to better distinguish between wet and dry locations. Notice that for all locations the final elevations are near H_{absm}, which means the final water elevations are higher than the initial water elevation even though the domain is closed and the water is by this time nearly at rest. This is a direct consequence of the nodal drying criteria in the WAD algorithm. Notice that for node 1 (figure 2.4b) located in the center of the basin in the deepest water, the elevation solution is relatively smooth, with oscillations occurring only when the water level has settled in around H_{absm}. Also, note that node 1 never dries and that the elevation solution for the case with $H_o = 1.0m$ returns to H_{absm} faster than in the case when $H_o = 0.5m$. At node numbers 51 and 10252, the elevation solutions (figures 2.4c and 2.4d) both experience periods of drying and then re-wetting. The higher H_o values result in drying occurring faster, and in the case of node 10252, results in wet/dry oscillation during the first 6 hours of the simulation. For both of these locations, the maximum elevation reached during a wetting phase is not affected significantly by the value of H_o, see figure 2.4c around 24 hours and figure 2.4d around 28 hours. However, during the final drying stage, after 40 hours, both of

these nodes experience larger oscillations in elevation around H_{absm} than node number 1 during the same time, for $H_o = 1.0m$. These oscillations are possibly due to the drying of neighboring nodes.

Figure 2.5 contains a time series plot of the total number of wet nodes in (a) and in (b) the corresponding computed total water volume in the domain for both values of H_o. Obviously, the WAD is not mass conserving even after all the water settles back into the basin. The total water height is now bounded between H_{absm} and H_o resulting in a higher resting elevation. Notice that for the $H_o = 0.5m$ case wetting began outside the basin earlier, wetted more nodes, and took longer to drain back into the basin than the $H_o = 1.0m$ case. This is again due to the wetting criteria in the WAD, where the smaller H_o allows for more meandering along the concentric bathymetry rings.

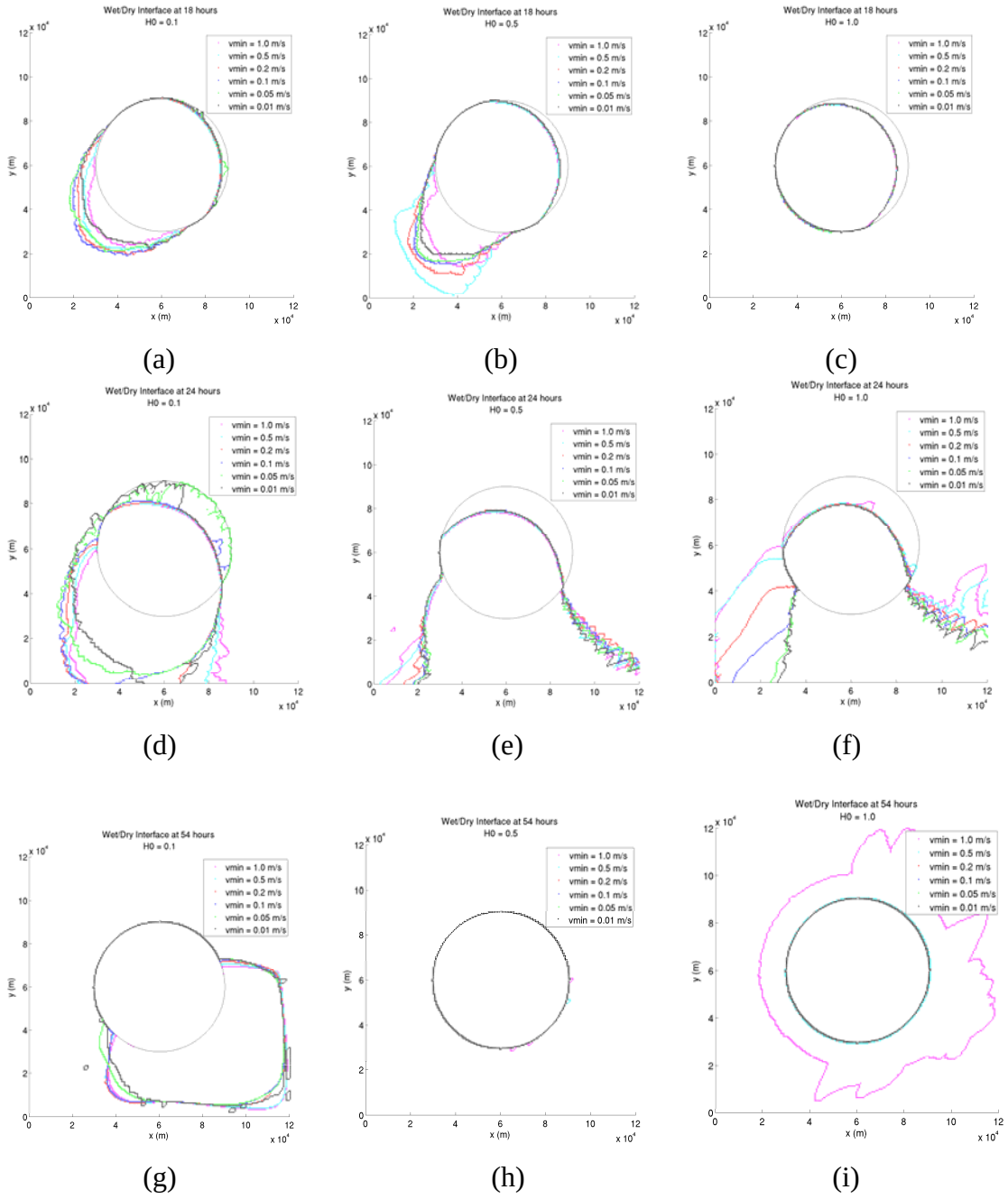

Figure 2.3. Contours of the wetting and drying front at 18, 24 and 54 hours (rows) into the simulation, using different H_o values (columns), and different $v_{\min}$ values represented by different color contours lines. The original coastline of the basin (in black) is included as a frame of reference.

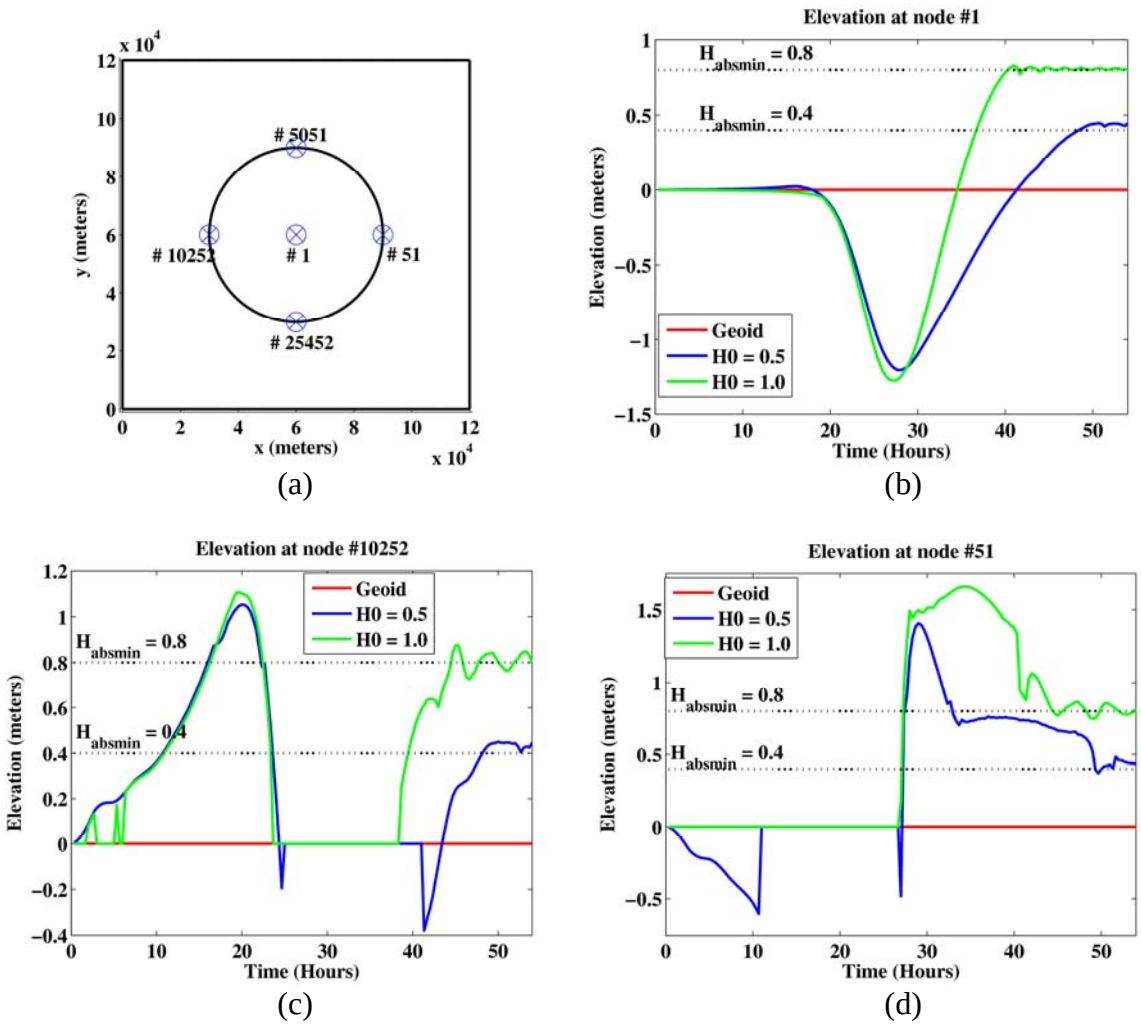

Figure 2.4. The (a) location of nodal points along the enclosed circular basin with their time series elevations (b-d) relative to the geoid, using $H_o = 0.5$ and $H_o = 1.0$ with $\nu_{\min} = 0.05$.

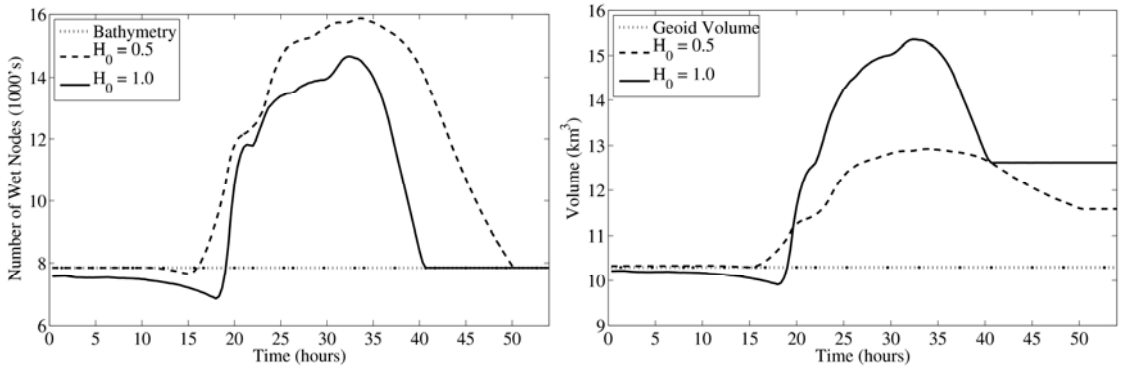

Figure 2.5. In (a) the number of wet nodes and in (b) the computed total volume of water during the simulation for two H_o values, $H_o = 0.5$ and $H_o = 1.0$, with $\nu_{\min} = 0.05$.

c. Idealized Inlet

The impact of the WAD algorithm's two free parameters on the velocity solution for a tidally dominant simulation is investigated using an idealized inlet, such as that used by Veeramony and Blain (2001) and Kapolnai et al. (1996). The idealized inlet is forced at the offshore boundary by an M_2 tide. It is shown that while the point-wise time series of elevations are smoothly varying with minimal noise, the velocity solutions are noisy and have near shock-like characteristics. These shock-like features are due to the wetting and drying of rows of elements at a time, which result in relatively large additions/subtractions of water mass to the computational domain. Even for realistic scenarios, mesh nodes can be aligned along bathymetry contours or equivalently along the land/sea interface. So here we examine how the free parameters for wetting and drying impact the shock-like features that can develop in the velocity solution.

For the idealized inlet shown in figure 2.6 the bathymetry varies linearly from 13 meters at $y = 0.0km$ to approximately -1.06 meters above sea level at $y = 33.0km$ and is independent of x. Two meshes are considered and shown in figure 2.7 along with the location of five recording stations that transverse the land/water interface. The first mesh is highly structured, in which regular divisions of equilateral triangular elements are arranged in regular rows and columns. These elements have edge lengths that range from $1000m$ at the open boundary, to $62.5m$ near the opening of the inlet. For this mesh, the arrangements of nodes in rows that follow bathymetry contours results in entire rows of elements wetting/drying simultaneously. To verify that the resulting simultaneous additions/subtractions of large amounts of mass to the simulation are the cause of the shock-like features in the velocity solution, a second unstructured mesh is designed. For the second unstructured mesh, the nodes are not arranged in orderly rows and columns. Therefore, it is not as susceptible to entire rows of elements wetting/drying simultaneously. This mesh has roughly the same size elements as the regular mesh. Station number 1 is located on land, station 2 is at the zero bathymetry contour, and stations 3, 4, and 5 are located in water of increasing depth, respectively. The run is forced with an M_2 tide of constant magnitude $0.3048m$ along the open boundary for 8 days. A 4-day effective ramp was applied to the forcing and a 4 second time step was required as defined by the CFL condition. No other forcing functions were applied. The hybrid nonlinear bottom friction option was again applied for this simulation.

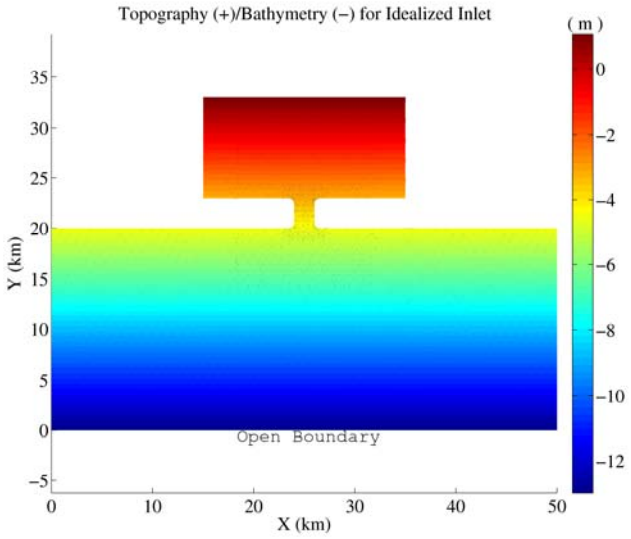

Figure 2.6. The bathymetry contours in meters for the idealized inlet case. Positive values are land values while negative values are water.

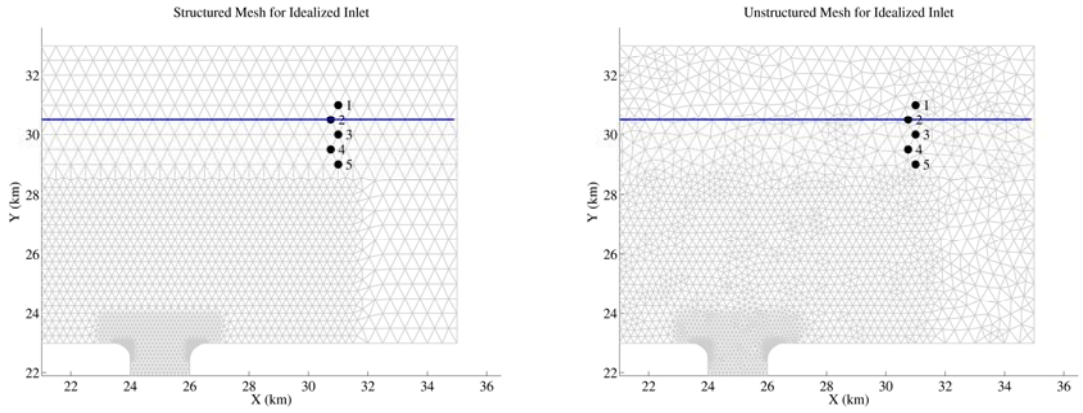

(a) (b)

Figure 2.7. A close up of (a) the structured mesh and (b) the unstructured mesh showing point locations (1-5) for the idealized inlet case. The blue line is the zero meter contour of bathymetry.

Figure 2.8 shows the time series of total water depth, *H*, in meters and the velocity components, *u* and *v* in *m/s* at all five stations. The first observation and one most frequently cited in others' works, i.e., Luettich and Westerink (1999), Dietrich et al. (2004, 2006}, is that the total water depth varies smoothly in a cyclic pattern following the tidal forcing. The velocity solutions are also cyclic, but they are locally very noisy. Our analysis will be confined to the dominant component of the velocity, the *v*-component. In figure 2.9, the *v*-component of velocity is examined over a 6 hour period to see details of the (a) wetting phase and (b) the drying phase. During the wetting phase, stations 3, 2, and 1 all become wet

in succession. Notice that just before each station turns from dry to wet, the *v*-component of velocity at the stations behind it (in deeper water), begins to level off or decrease. Once the forward station wets, the deeper stations increase dramatically in value in a near shock-like manner. Stations in water deeper than station 5 (not shown), and the dip and surge pattern continues to be exhibited for several rows of elements behind the wetting station. A similar dip and surge pattern is exhibited during the drying phase which is shown in (b).

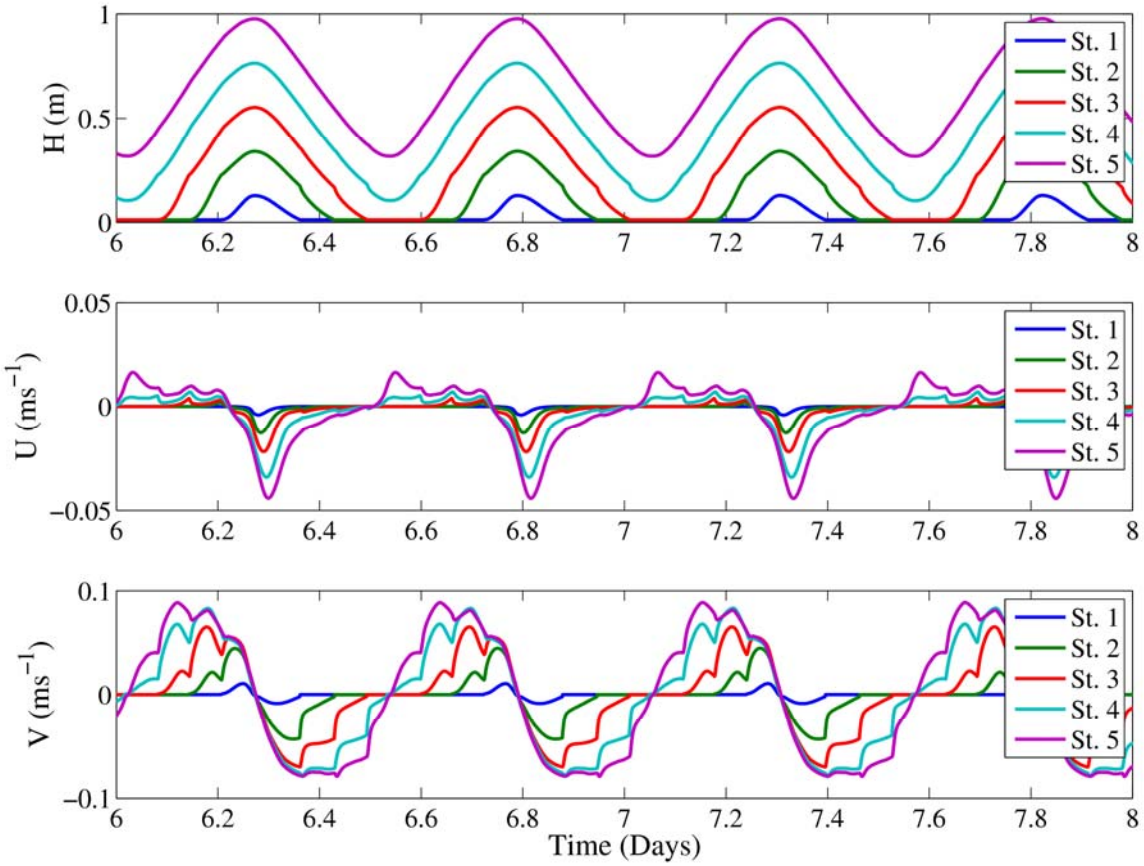

Figure 2.8. Time series of total water depth, *H*, horizontal velocities, *u*,*v*, at five stations.

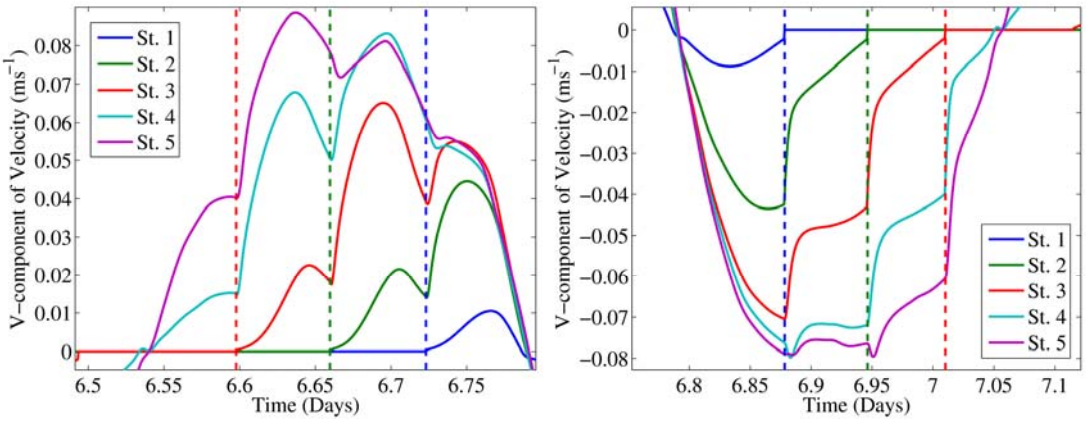

Figure 2.9. A 6 hour time series of the *v*-component of velocity, at five stations during (a) a wetting phase and (b) a drying phase. The colored dashed lines indicate when the stations either wetted or dried.

The effects of varied H_o values on the dip and surge characteristics in *v* and in $\frac{dv}{dt}$ at station 5, are shown in figure 2.10. Other stations have similar results. The results for the unstructured mesh are also included for comparison purposes. For increasing values of H_o, the magnitude of the dip and subsequent surge becomes more severe. In comparison, notice how the unstructured mesh leads to a much smoother velocity solution. This is a result of fewer elements becoming wet/dry at the same time, in contrast to the row by row wetting/drying in the uniform mesh case. The influence of the parameter $V_{\min}$ is negligible on the dip and surge feature observed in the velocity solution for a fixed $H_o = 0.1m$, as shown in figure 2.11. In fact the elevation curves for the case of $v_{\min} = 0.005\, m/s$ and $v_{\min} = 0.01\, m/s$ lay on top of one another.

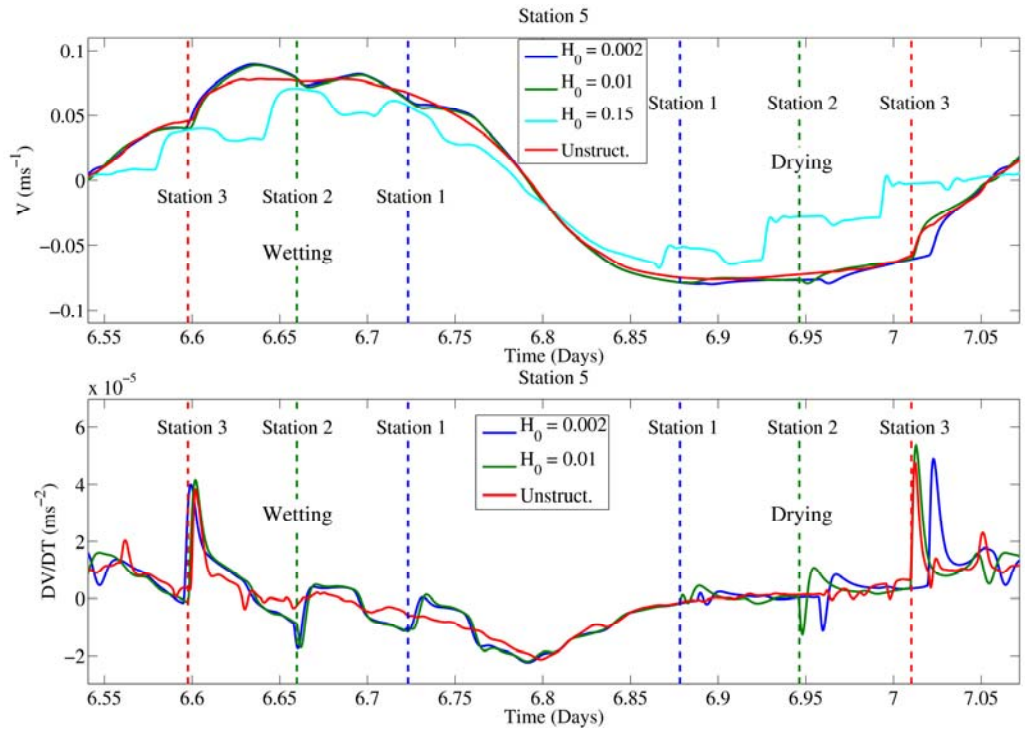

Figure 2.10. A 6 hour time series at station 5, of the *v*-component of velocity and of the discrete time rate of change of *v*, for different values of H_o over the structured mesh. The velocity response over the unstructured mesh for $H_o = 0.01$ is also included. The colored dashed lines indicate when the station either wetted or dried for the case of $H_o = 0.01$.

The dip and surge pattern observed in the *v*-component of velocity, is a result of what amounts to a temporary no-normal flow boundary condition imposed by the WAD algorithm along the wet/dry front. Along the wet/dry front, an artificial barrier is in place that holds the water back until it reaches a critical height dictated by H_o and $v_{\min}$. While the barrier is in place, water levels are increasing behind it during a wetting phase and the flow pattern is diverted due to the no-normal flow condition. Hence, we see a leveling off and/or decrease in the *v*-component of velocity (in this case), until the water level reaches the critical threshold and the barrier is removed, there-by allowing water to surge forward. With the regular mesh, we have a series of temporary barriers arranged in rows that are encountered one after the other as inundation occurs, but with the unstructured mesh this is not the case. During the drying process, water levels decrease gradually until the cutoff value of H_{absm} is reached, after which time the water mass is removed from the computation. This sudden removal of water mass causes the shock-like condition seen in the drying phases in the *v*-component of velocity. The height of the artificial barriers is controlled principally by H_o and that is why we see the most influence on the dip and surge pattern from varying H_o.

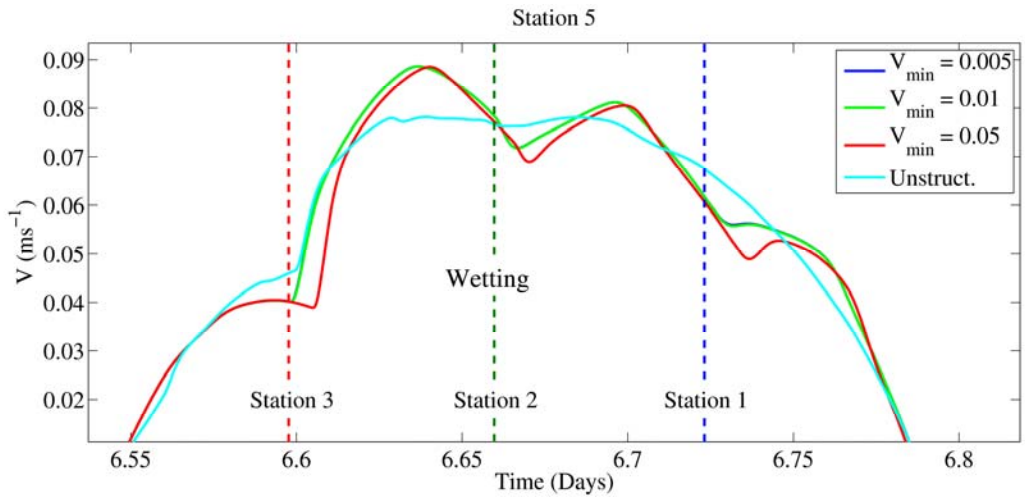

Figure 2.11. A 6 hour time series of the *v*-component of velocity, at station 5 for a wetting phase with varied values of $v_{\min}$. Note that the results for cases $v_{\min} = 0.01$ and $v_{\min} = 0.005$ are virtually indistinguishable. The colored dashed lines indicate when the stations wetted for the case of $v_{\min} = 0.01$.

The variability of $\frac{dv}{dt}$, the acceleration, demonstrates the influence of the wetting/drying of nearby elements on the velocity solution. Of particular importance is how noisy the values of $\frac{dv}{dt}$ are immediately following a wetting/drying of a row of elements. Not only are the velocity solutions experiencing sudden changes but so too are the values of $\frac{dv}{dt}$. These sudden changes can lead to instabilities during the solution process. The authors' own experiences confirm that instabilities in the WAD are almost always first observed in the velocity solution step.

d. Gently Sloping Beach

While the wetting and drying algorithm performs well in tidal regions that have simple bathymetric slopes, there are limitations when the bathymetric slope flattens, as in the case of a tidal or mud flat. The Gently sloping Beach test problem demonstrates that the algorithm allows wetting and drying fronts to propagate in non-symmetric ways, even for symmetric applications such as this one. Additionally, during the drying phase, small pockets of elements can remain wet even when negative pressure gradients exist. The mesh for the gently sloping beach is designed to highly resolve the wetting and drying region and to smoothly transition to decreasing element sizes with decreasing water depth, see figure 2.12a. The spatial scales of the problem are proportional to those of a realistic beach under tidal forcing. The modeled domain is a square box of dimension 4,960 meters with a bathymetry profile that gently slopes upward to a plateau beach. The water depth ranges from 9.32*m* at the open ocean boundary to -0.1*m* above sea level at the plateau beach. The bathymetry profile in the cross-shore (along the *y*-axis) is as follows,

$$z(y)=\begin{cases}2.0-0.006(y-1200),\text{if } y\le 1200m;\\ c_o+c_1y+c_2y^2+c_3y^3,\text{if } y\le 2500m;\\ -0.1,\text{if } y>2500m\end{cases}$$

where the cubic polynomial coefficients c_i are determined by solving a 4 x 4 system of linear equations satisfying $z(1220m)=2.0m$, $z(1780m)=-0.1m$ and the slopes ($z'=\frac{dz}{dy}$) satisfying, $z'(1220m)=-0.006$ and $z'(1780m)=0m$. The mesh consists of 92,176 computational nodes and 183,836 triangular elements. The mesh spacing is graded from the open ocean boundary where nodal spacing is 80*m* to the water/land transition zone (bathymetry +/-) where nodal spacing is only 5*m*, see figure 2.12a.

The model simulation is for 14.4 hours with a 6 hour ramp period applied to the forcing. A 0.1 second time step is required by the CFL condition. The simulation is forced for 9 hours with an elevation specified as a sinusoidal wave with amplitude of 0.135 meters and a period of one hour. After 9 hours the tidal forcing function is shut off entirely and no other forcing is applied. The period without forcing allows for investigation of the drying phase of the WAD algorithm. A value of $H_o=0.01$ meters for the minimum water depth and a value of $v_{\min}=0.01m/s$ for the minimum wetting velocity are selected.

During the tidally forced portion of the run, the wetting and drying front moves in a predictable fashion. Water moves up the slope and onto the beach plateau during inundation. This is subsequently followed by a retreat of the wetting front off the beach and down the slope. An unexpected result is the non-symmetric propagation of the wetting front, see figure 2.12b. This same asymmetry is observed during the drying phase. A matter of more concern is the lack of drainage during quiescent (non-forced) periods, see figures 2.12c and 2.12d. The pockets of wet elements left on the beach remain active in the simulation and can contribute to instabilities. In a wind-driven application, typical for inundation concerns, such instabilities can easily manifest when pockets of water move around in response to rising elevations caused by the wind forcing. In fact, since the WAD algorithm is not mass conserving, it would be possible to cause pockets of water to either increase in area, stay at a constant depth or even increase in depth, even though these pockets are cut off from the main body of water.

As we mentioned earlier, one of the past upgrades to the WAD algorithm was an empirical check that prevented downhill flow from originating from barely wet nodes, except in the case of overtopping a weir (or barrier node). The concept was conceived for situations when water levels crept up a hill and barely wet the crest of the hill which would in turn cause downward flow behind the hill. However, the same scenario is occurring for this gently sloping plateau beach case when we are trying to drain water back off the plateau. In this case, the empirical check is turning off elements (drying them), before all the water is drained and leaving pockets of wet elements, see for example figure 2.12c between $y=1670m$ and $y=1725m$.

e. Summary

A detailed sensitivity analysis of the surge and current response to the user controlled parameters of the wetting and drying algorithm, H_o and $\nu_{\min}$, used in the continuous Galerkin formulation of ADCIRC has been presented Three case studies support the analyses and bring to light some computational issues observed with the WAD scheme. Issues include a) noisy velocity solutions caused by the sudden wetting or drying of large numbers of elements simultaneously, b) difficulty in drying elements over very small bathymetric gradients, a problem for tidal flats, and c) instabilities that result from incomplete drainage leaving isolated pockets of wet elements. This last issue is very problematic during wind-forced simulations in that the wind acts on these isolated elements of water. The parameter H_o is most influential, affecting the global mass balance due to the non-conservative nature of the WAD algorithm. The parameter $\nu_{\min}$ has substantially less effect on the WAD's performance. Depending on the purpose of the simulation, a small value of H_o does not always produce the best solution. However, larger H_o values can produce shock-like characteristics in the velocity solutions. Overall, for most cases tested the WAD algorithm produces reasonable results but care should be taken in setting the value of H_o. One side note, using external boundary types, IBTYPE = 30, 40, and 41 with boundary nodes that are allowed to wet and dry, can quickly result in an unstable velocity solution under cyclic forcing conditions. This is due in part to the fact that no constraints are being placed on the velocity solution for these boundary types and, as such, the velocities can become unrealistically large during the ebb stage of the cycle.

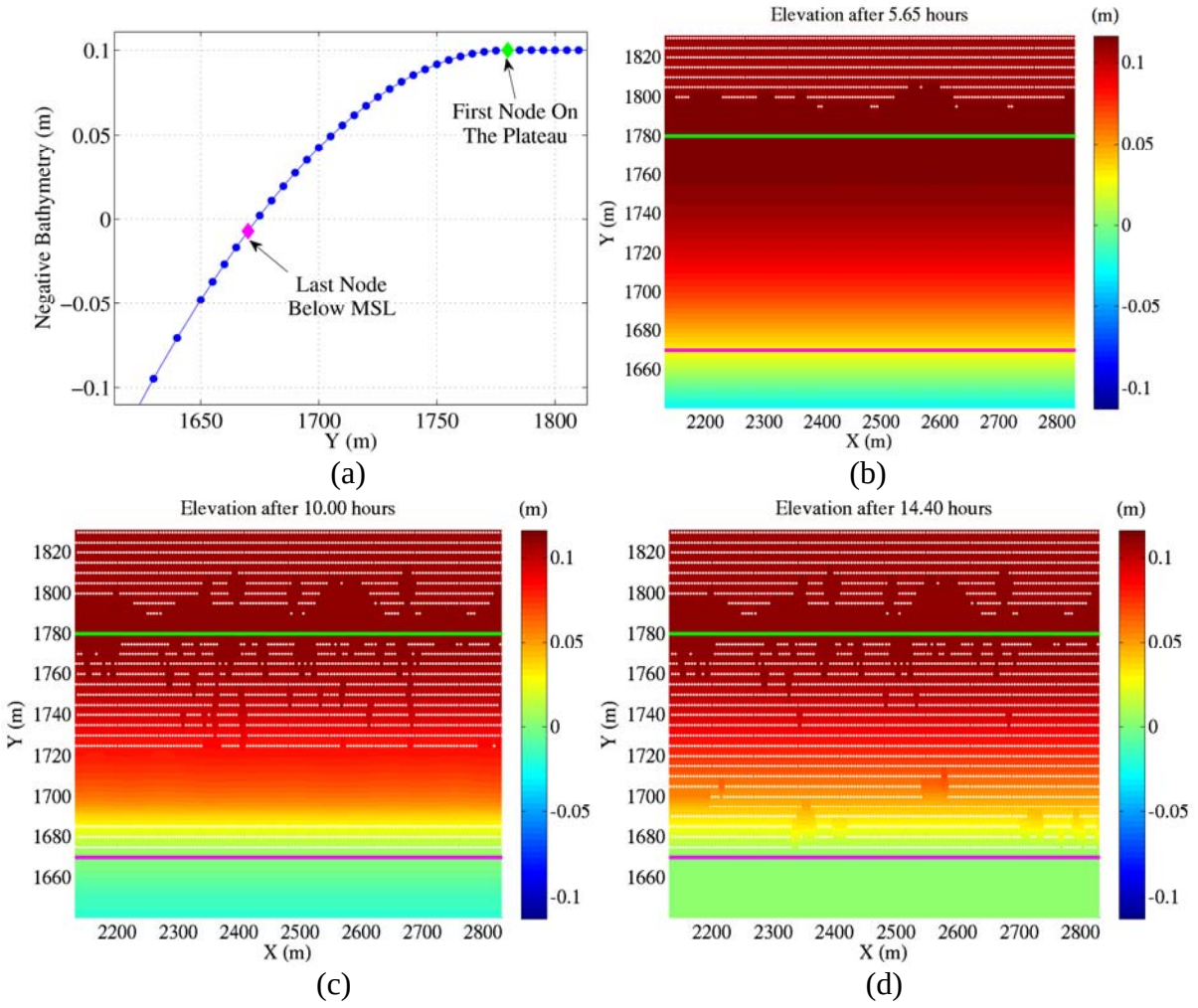

Figure 2.12. For the gently sloping beach, (a) shows a close up of the mesh topography/bathymetry with nodes indicated by blue circles, the magenta diamond indicates the last node below MSL and the green diamond indicates the first node on the plateau beach, -0.1*m* above sea level. In (b)-(c) a series of snap shots of elevation (dry nodes indicated with white '.') for (b) a wetting phase, (c) a drying phase and (d) the final elevation.

4. Validation Test Results – Hurricane Katrina Storm Surge

Throughout modern history, amphibious assaults and landings have been a mainstay of U.S. Navy operations. The vulnerability of these landing craft to capsizing, swamping, stranding, and filling with sand and water was clearly realized following a post-World War II review of amphibious operations. Many amphibious landing problems and casualties during World War II could be attributed to the waves, currents and water levels of the local environment. Following the major invasion of Incheon Harbor in the Republic of Korea, a U. S. Navy Tank Landing Ship was stranded during low tide near the Tidal Basin on Incheon's waterfront, 20 September 1950.

More than fifty years later, the Navy still finds inundated environments challenging for operations. Since the declaration of the Global War on Terrorism following the events of September 11, 2001, military operations are increasingly focused on special operations that take place in coastal environments such as estuaries, shallow waterways, and inland rivers. The occurrence of inundation in these operational theatres is typically caused by extreme tidal ranges, rainfall-induced flooding events, and/or wind-generated setup that directly affect the insertion and movement of Naval Special Warfare (NSW) forces. NSW forces routinely insert themselves into river and estuarine environments where the only known information may be an outdated, perhaps 30-year old, topographic map. Areas that are subject to inundation processes are often located at the cusp of the land-sea interface where algorithms for processing satellite imagery break down or are sub-optimal.

Inundation from storm surge is also a concern for stateside Navy installations. The two major homeports for the U. S. Navy's east coast fleet are at Norfolk, Virginia and Mayport, Florida, both vulnerable to landfalling Atlantic hurricanes. A decision to relocate the Norfolk harbor fleet, for example, could cost $5 million and would need to take place three days in advance of a predicted landfall in order to recall personnel and ready ships in maintenance or overhaul for evacuation. Most recently, the Navy base at Pascagoula, Mississippi located on the Gulf of Mexico was directly impacted by the landfall of Hurricane Katrina, 29 August 2005.

As we now know, the Naval Station Pascagoula was not alone in registering effects from Hurricane Katrina. The devastation to Gulf Coast communities on 29 August, 2005 from Hurricane Katrina far exceeded all previously recorded storm events. From the extent of storm damage to the coastal states of Louisiana, Mississippi and Alabama, Katrina has been categorized as the most destructive and costliest natural disaster in the history of the United States. According to the National Oceanic and Atmospheric Administration (NOAA), the storm surge along the Mississippi coast was the highest storm surge ever recorded in the United States.

The storm surge and inundation from Hurricane Katrina that devastated Mississippi Gulf Coast communities on 29 August, 2005 presents a unique opportunity to evaluate the capabilities at NRL and within the Navy to predict storm surge and inland inundation. Reconstruction of the storm surge and inundation events precipitated by Hurricane Katrina provide an invaluable opportunity to evaluate the Navy's capability to predict coastal surge and inundation and to direct future developments that enhance such a capability. A highly realistic simulation of Katrina's storm surge and inland inundation is developed using the 2DDI version of the ADvanced CIRCulation (ADCIRC) model. Unprecedented observations of the currents as well as high water marks, extent of inland inundation and water levels are available to assess model's performance.

a. Model Configuration

The initial requirement for reconstruction of hurricane Katrina's storm surge along the Mississippi Gulf Coast was a computational mesh that extended from the shoreline to inland locations. The importance of a quality mesh cannot be understated in the modeling of inundation events. To accurately represent the surge and inundation the mesh must resolve fine-scale changes in bottom slope and topography, details of the coastline, and other geographic features such as islands, inlets and channels, while simultaneously preserving properties of the triangular elements that promote model stability and retaining a

computationally viable problem (i.e. a timely solution). The transitioned software, MeshGUI, developed for semi-automated mesh generation is applied to construct an unstructured finite element mesh using refinement criteria based on the specified bathymetric/topographic values and constrained by the coastal boundary points that extend over the land to allow inundation processes. The bathymetric and topographic data source used in shallow coastal areas was taken from Northern Gulf Littoral Initiative bathymetric data at 3 arc second resolution. To eliminate the discontinuities between data blocks within the NGLI data set, particularly in the Pearl River Basin, bilinear interpolation was applied across such boundaries to smooth the bathymetry and topography values. Smoothly varying bathymetry and topography from element to element is very important for the stability of ADCIRC's wetting and drying algorithm. The final unstructured finite element mesh designed to best capture Katrina's storm surge and inland inundation consists of 489,071 nodes and 956,869 triangular elements (figure 4.1). Resolution ranges from 63*m* to nearly 6*km* (figure 4.2) with 225*m* to 500*m* resolution in most shallow coastal and inland areas.

The mesh centers on the northern Gulf Coast region encompassing inland areas, but also includes the entire Gulf of Mexico and extends out into the western North Atlantic Ocean. Such an expansive domain allows the surge to naturally build up within the modeled region as the hurricane moves from the deep ocean into coastal waters (Blain et al., 1994). Furthermore, ocean boundaries in deep water are subject to minimal surge and inverted barometer effects and can appropriately accept tidal forcing from a global tide model. These boundaries also are removed from the coastal area of interest.

The landward boundary includes inland areas concentrated on the Mississippi coast extending eastward just past Mobile Bay, AL and westward including the entire Pearl River basin and areas inland to Interstate 10 on the north shore of Lake Ponchartrain, LA. As important conduits of storm surge, the inclusion of river basins from the coast to inland, upstream locations is important. The inundating surge did not actually penetrate to the land boundaries rendering the no flow condition (IBTYPE = 0) a good choice. If surge had propagated to the inland boundary, a radiative boundary condition would be more appropriate (IBTYPE = 30) to prevent the surge from reflecting back into the model domain. The targeted spatial resolution of the mesh near the coast and inland is 225*m* and represents a balance between the desire for fine-scale resolution, the need for stability of the inundation algorithm, and accounts for computational constraints imposed by the necessarily small time step integration.

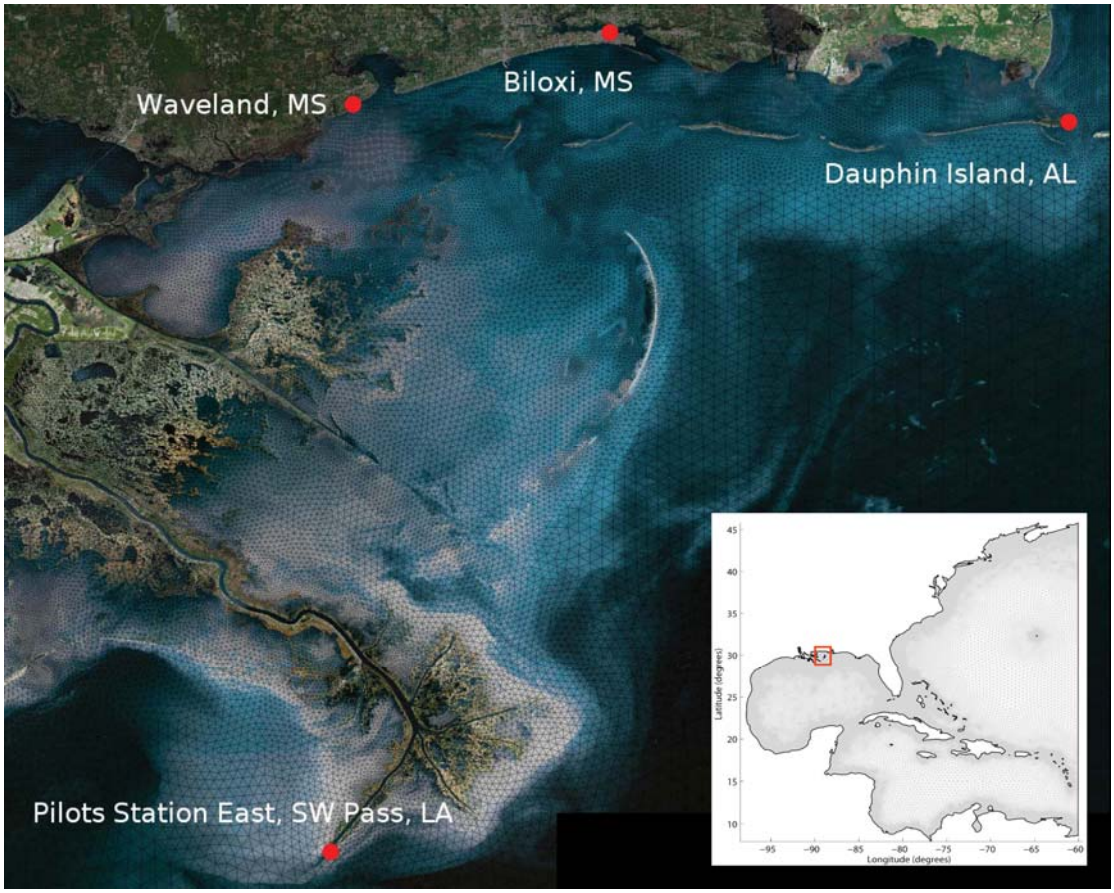

Figure 4.1. The density of the triangular elements in the northeast Gulf of Mexico contained in the computational mesh for the entire model domain (inset) overlays a true color satellite image that distinguishes land from water.

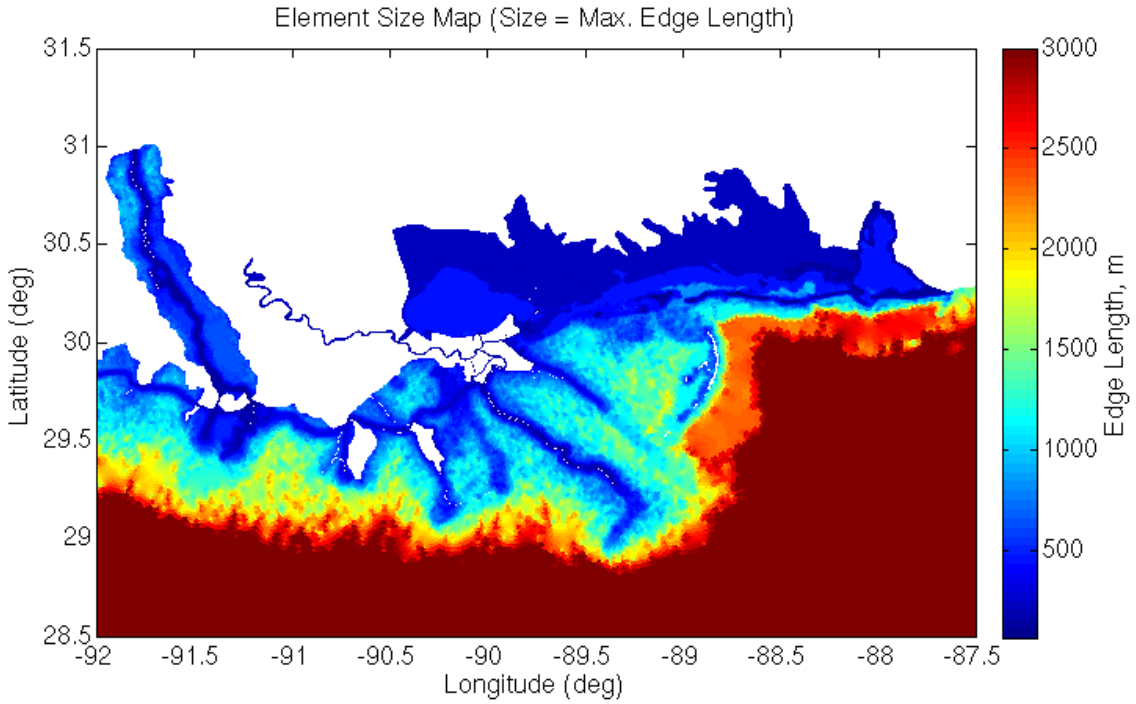

Figure 4.2 The resolution in meters of the computational mesh created for the northeast Gulf of Mexico storm surge and inundation computations.

To drive the surge model, the best available wind forcing was produced by NOAA's Hurricane Research Division (HRD) at the Atlantic Oceanographic and Meteorological Laboratory (AOML) through the HRD Real-time Hurricane Wind Analysis System (H*Wind) project. The H*Wind product is an integrated tropical cyclone observing system within which wind measurements from a variety of observation platforms are used to develop an objective analysis of the distribution of wind speeds in a hurricane (Powell et al., 1998). The wind fields are typically constructed from a real-time analysis of flight-level reconnaissance data, satellite observations, pressure-wind relationships and available surface data. We interpolate the 3-hourly H*Winds using an approach that follows the storm center in time to preserve the integrity of the storm as it moves in time and we further downscale the winds fields to fifteen-minute intervals. The time interpolated wind fields are spatially interpolated to the computational mesh and then converted to wind stress. The wind drag at the sea surface is simply specified as a constant and with no distinction between winds over land or water or the directional history of the wind. More recent versions of the ADCIRC model now accommodate spatially varying surface roughness values that can be computed to reflect land use, canopy, and vegetative cover leading to more realistic representations of the wind drag (Westerink et al., 2008).

In addition to surface winds, tidal forces are applied including those that act on the modeled body of water (tidal potential) and those caused by tides entering the domain at the open ocean boundary. At the deep ocean boundary, tidal forcing is applied at frequencies of the daily (K_1, O_1) and twice daily (M_2, S_2, and N_2) tides obtained from the Grenoble global tidal model (FES99, Lefevre et al, 2002). The tidal potential is applied on the interior of the domain for the same constituents.

The ADCIRC model fort.15 input file parameter specifications for the 2D wetting and drying application with tide and wind forcing are configured using the Makef15 GUI. The default settings in the Makef15 GUI were changed in the following manner:

- Activate the non-fatal error override, NFOVER = 1
- A hybrid nonlinear bottom friction formulation is selected, NOLIBF = 2
- Activate tidal potential forcing, NTIP = 1
- Wind velocity and surface pressure forcing are selected, NWS = 4
- Time step is reduced to 1 sec, DTDP = 1.0
- The reference time is set to the time after ramping, REFTIM = 14.0
- The meteorological forcing time increment is 15 minutes (900 sec), WTIMINC = 900
- The length of simulation is set to 18.41666667 days, RNDAY = 18.41666667
- The ramp period is set to a duration of 15 days, DRAMP = 15.0
- The minimum depth, H0, is set to 0.01 and the minimum velocity for wetting is 0.01 (NODEDRYMIN and NODEWETMIN are not used), H0 = 0.01, VELMIN = 0.01.
- The central projection points are specified for the model domain, SLAM0,SFEA0 = -88.5, 29.0, respectively.
- Parameters for the hybrid nonlinear bottom friction coefficient are specified, CF = 0.003 (minimum friction coefficient), HBREAK = 2.0 (break depth), FTHETA = 10.0, and FGAMMA = 1.333 (see equation (6), Section 1b)
- Assign 5 tidal potential constituent, NTIF = 5
- Tidal potential constituents, TIPOTAG = K1, O1, M2, S2, N2
- Input the date at the start of the simulation to compute the nodal factors (August 26, 2005)
- Assign 6 periodic boundary forcing frequencies, NBFR = 6
- Tidal potential constituents, BOUNTAG = STEADY, K1, O1, M2, S2, N2
- Input the date at the start of the simulation to compute the nodal factors (August 26, 2005)
- Select global elevation output, NOUTGE = -1 for just under 3 days (TOUTSGE = 15.97916667, TOUFGE = 18.416667.0 model days) every half-hour (NSPOOLE = 1800)
- Select global velocity output, NOUTGV = -1 for just under 3 days (TOUTSGV = 15.97916667, TOUFGV = 18.416667.0 model days) every half-hour (NSPOOLV = 1800)
- Output a hotstart every 6 hours (21600 time steps), NHSTAR = 1, NHSINC = 21600 time steps

The hindcast simulation of Hurricane Katrina storm surge began 27 August 2005 (0000 UTC) following a ramp-up period of 15 days during which all forcings were gradually applied until full strength was reached at the end of the ramp-up phase. By this time in the simulation, Hurricane Katrina had crossed the state of Florida and had entered the warm waters of the Gulf of Mexico (figure 4.3). Katrina was past its peak intensity by the first landfall near Buras, Louisiana at 6:10 am CDT (1110 UTC) 29 August 2005 and a second landfall near the Louisiana/Mississippi border occurred about 9:45am CDT (1445 UTC) 29 August 2005. The model hindcast of surge and inundation ended at 5:00am CDT (1000

UTC) on 30 August 2005 which coincided with the last available H*wind product contained within the mesh. At every 1-sec time integration of the model, the water levels and depth-integrated currents are computed by the ADCIRC model at all points in the model domain.

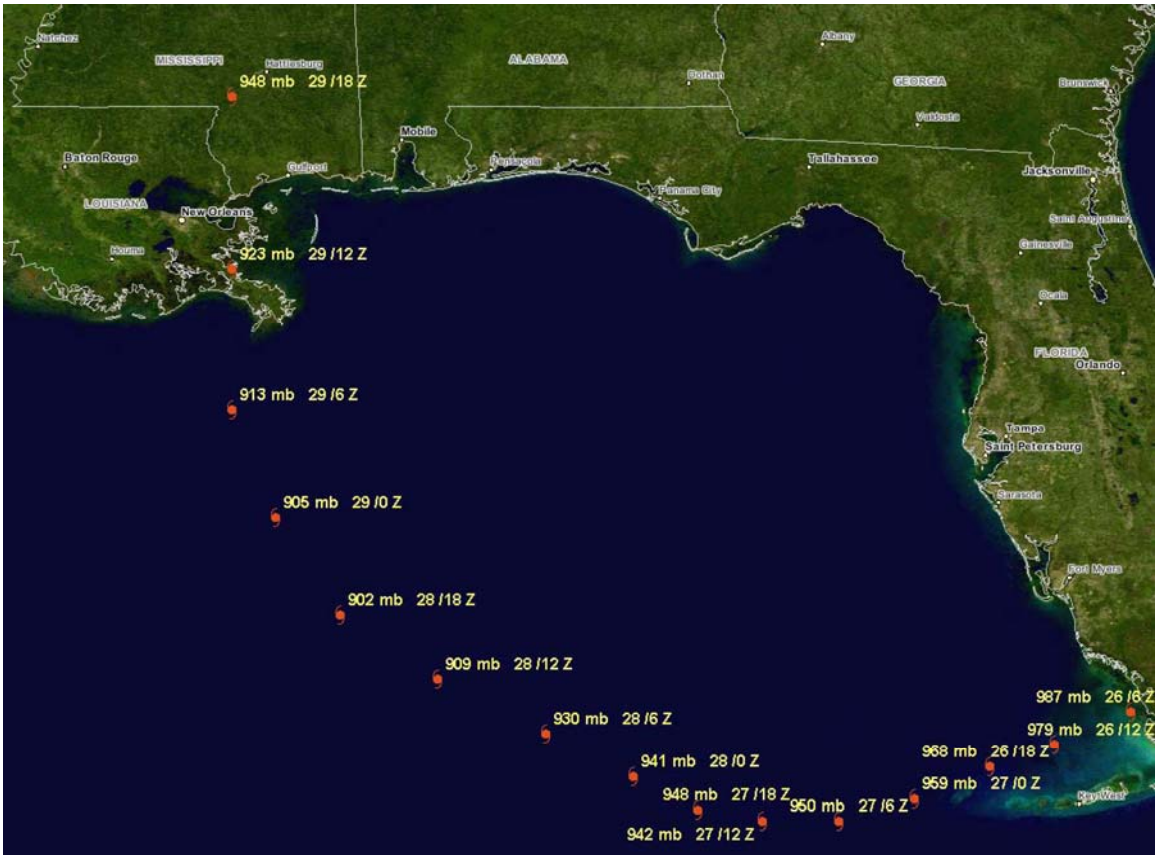

Figure 4.3: The track of Hurricane Katrina at 6 hour intervals once the storm enters the Gulf of Mexico off the west Florida coast at 6Z 26 August 2005 with central pressure of 987 mb. The final location of the storm at hurricane strength occurred in southern Mississippi at 18Z 29 August 2005 with a central pressure of 948 mb.

b. Water Levels

The surface winds from Hurricane Katrina at 10:00am CDT (1500 UTC) on 29 August 2005 (figure 4.4) and the resulting storm surge computed by the ADCIRC model (figure 4.5) for the same time and date are presented. Surge heights well over 20 feet at the coastline on the right side of storm reflect not only the strength of the storm winds at the time of landfall but also the build-up of surge that occurred prior to landfall. Even higher water levels are shown inland (near Waveland Mississippi and west of Biloxi, Mississippi) as the large radius of hurricane winds easily pushed water over the gently sloping coastal lands. Timing of the inundation indicates that areas to the west of Waveland, Mississippi including the northern coast of Louisiana (Slidell) inundated first as hurricane winds pushed water into the bays and up the rivers. Not until landfall did the Mississippi Gulf coast west of Biloxi experience its peak flooding. Note that even after landfall (figure 4.5), sea levels remain

elevated throughout the coastal waters. For some areas far inland particularly at the wetting front, excessive inland flooding (over 30 feet) is computed. Analysis of these hindcast results have revealed limitations in the inundation mechanism within the ADCIRC model that prevent rapid advancement of a wetting front and incomplete drainage of the flood water following peak storm winds (evidence of this is northwest of Stennis Space Center, Mississippi).

Timing of the wetting front is difficult to validate since observations are often limited. However, the modeled water heights are compared to recorded elevations at three observing stations that survived the storm, Pilot's Station, SW Pass, Louisiana, Waveland, Mississippi and Dauphin Island, Alabama (figure 4.6). In each case the agreement between the modeled and observed water levels is quite reasonable with correlation coefficients of 0.75 or higher. The phasing of the tides and peak surge computed by the model are leading the observed values by no more than a couple of hours and the model underprediction as the storm nears its landfall position is likely due to the neglect of surface wave effects.

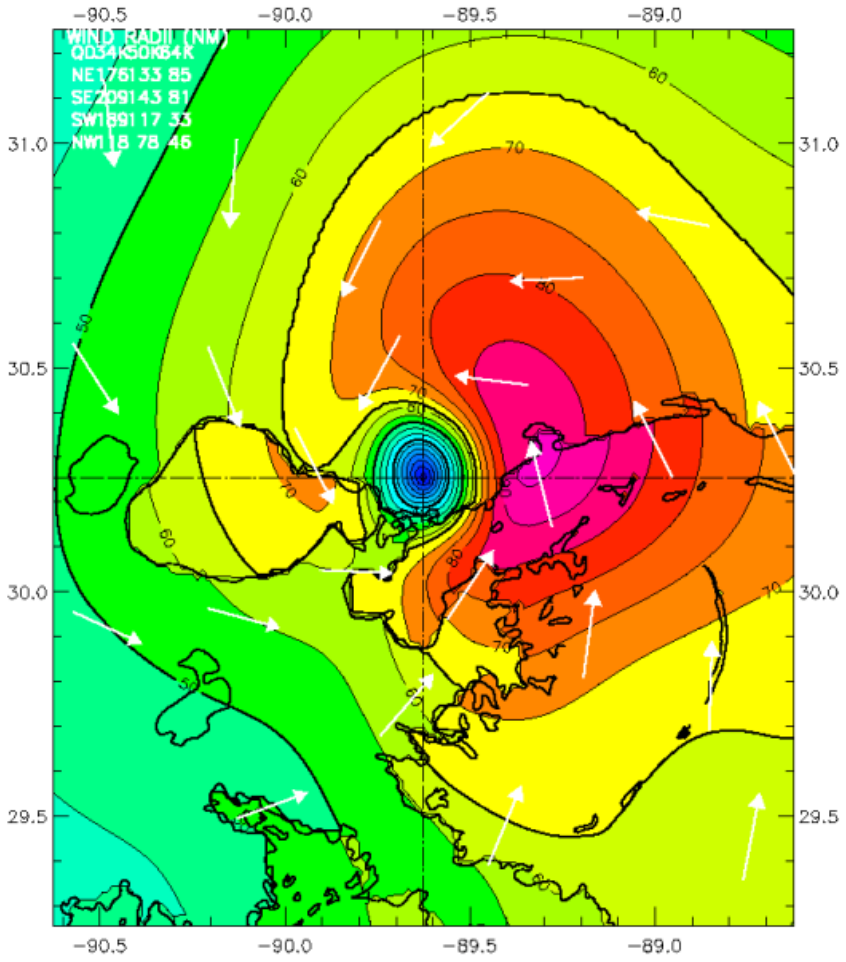

Figure 4.4: The magnitude (color) and direction (arrows) of the maximum 1-minute sustained surface winds in knots for Hurricane Katrina at 10:00am CDT (1500 UTC) on 29 August 2005. [Courtesy of the NOAA Hurricane Research Division]

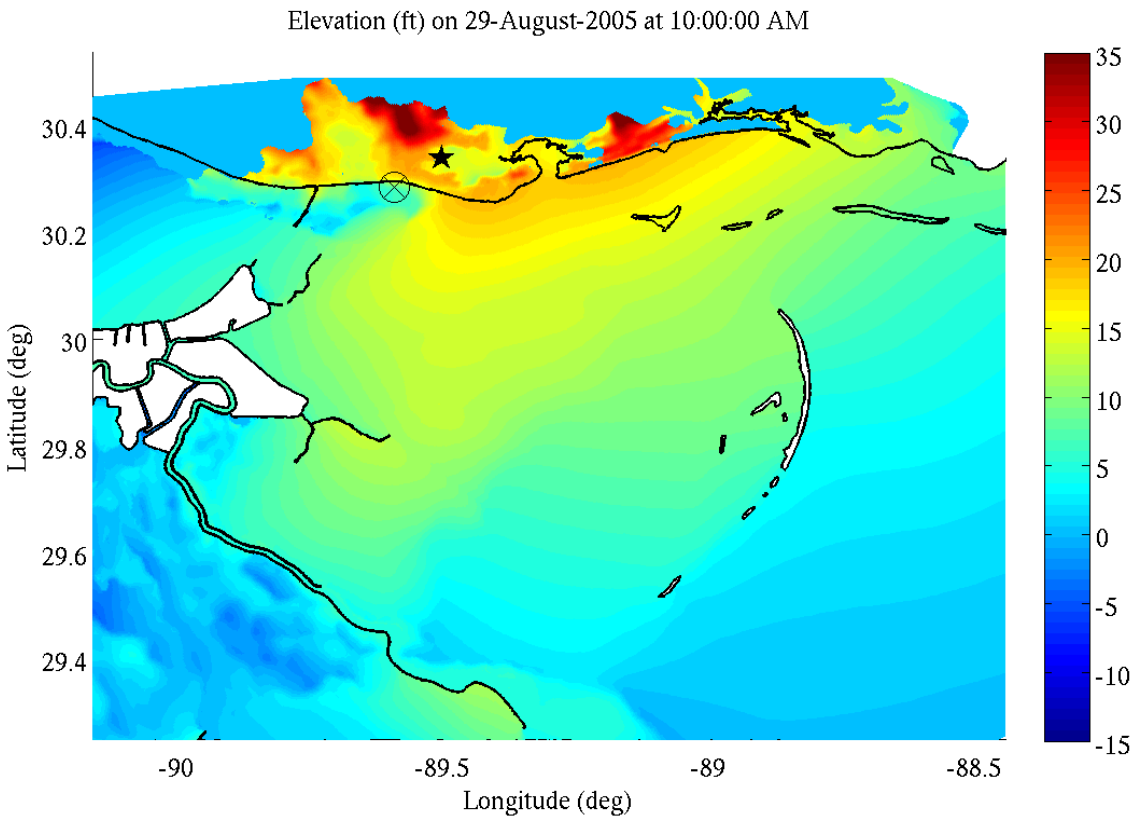

Figure 4.5: The ADCIRC model computed storm surge and inland inundation elevation in feet for Hurricane Katrina at 10:00am CDT (1500 UTC) on 29 August 2005. The coastal outline is shown in black. The storm center is shown by a circled X and the location of Stennis Space Center, Mississippi is given by a star.

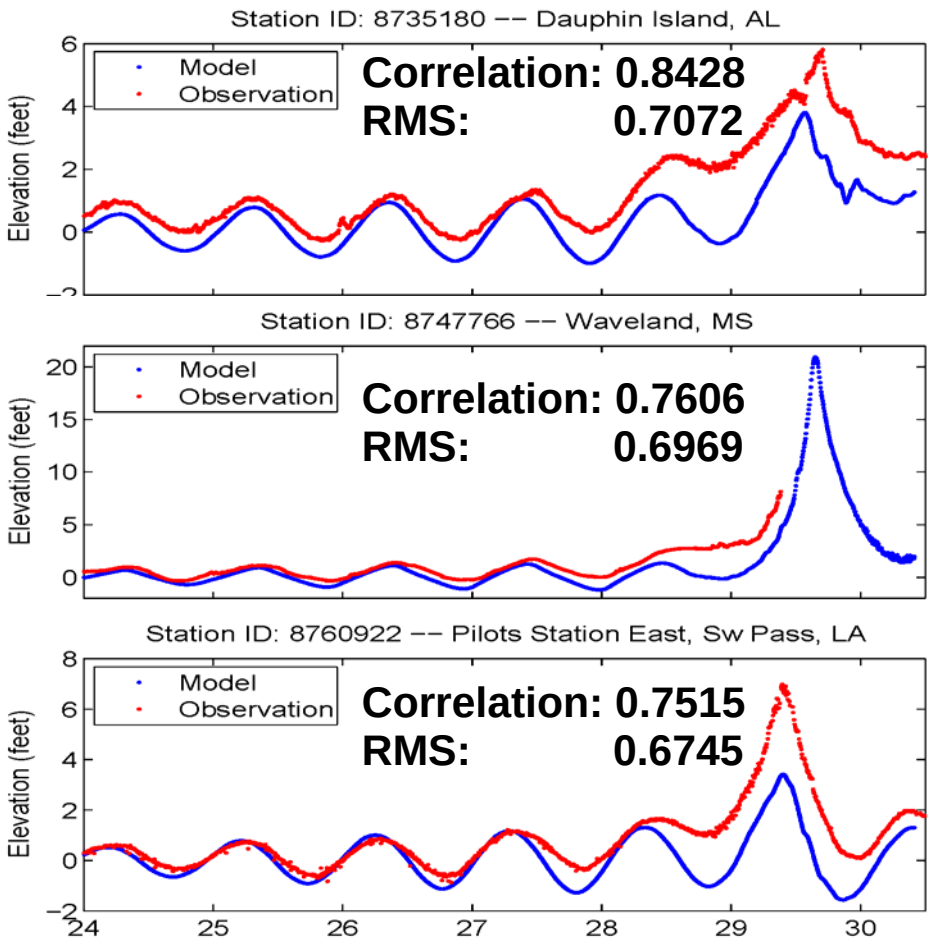

Figure 4.6: Time series of model computed (blue) and observed (red) water elevations in feet at three NOAA coastal stations, Pilots Station East, Sw Pass, Louisiana, Waveland Mississippi, and Dauphin Island, Alabama.

c. Inundation

A qualitative assessment of the model-computed inundation is provided by comparing a map of modeled high water levels with Federal Emergency Management Agency (FEMA) inundation maps (FEMA, 2005 and FEMA, 2006) as shown in figure 4.7. On the FEMA maps for Louisisana (figure 4.7b) and Mississippi (figure 4.7c), zones of inundation are highlighted in yellow with the storm track visible as a red line on the Louisiana map. The FEMA and ADCIRC inundation maps are alligned vertically within figure 4.7 to facilitate a qualitative intercomparison between the two. The ADCIRC inundation map (figure 4.7a) is created by recording the highest water elevation at each model grid point over the entire simulation period of the storm. These high water mark maps provide no information on timing of the inundation front and the comparison to FEMA inundation maps does not provide an assessment of the magnitude of the water level, but rather this comparison measures the model capability with repsect to the spatial extent of inland inundation.

Moving from west to east in figure 4.7, the model represents well the significant pathway for inland inundation in Lousiana along the Pearl River basin. The lengthly inland extent of inundation associated with the Pearl River basin indicated in the FEMA map is also well captured by the model with notably less inundation to the west of the Pearl River basin. However, the model records anomalous inundation just to the east of the hurricane Katrina landfall path in Mississippi. The FEMA inundation map for Mississippi (figure 4.7c) shows large areas of inundation west of Bay St. Louis which is consistent with locations immediately to the right side of a landfalling hurricane. Moving eastward the primary inundation pathways are the tributaries entering Bay St. Louis and Biloxi Bay. Very little inundation occurs along the coastline between Bay St. Louis and Biloxi Bay which is indicative of locally high ground. The modeled inundation also reflects this pattern of inundation (following river tributaries out of bays and limited inland inundation along the coast near Pass Christian, MS). The exception in the modeled inundation is the more extensive inundation casued by the merging of water from the eastern tributaries of Bay St. Louis with water coming from the western tributaries of Biloxi Bay. The remaining area of significant inundation both recorded by the FEMA map and computed by the model is in and around Pascagoula Bay and inland up the Pascagoula River. Overall the modeled patterns of inundation reflect those shown in the FEMA Inundation Maps. In the model, it is likely that the wetting front moved inland too quickly covering more area in the regions of highest water levels and then steeper topography prevented additional wetting and caused water to pile up artifically in several locations as inidated by the red in the figure 4.7a.

An evaluation of the modeled high water magnitudes of the surge and inundation is accomplished by comparing computed high water mark values to high water marks measured by the United Stated Geological Survey shortly after the storm. At each location in the mesh, the highest water level from the model (evaluated on 10-minute intervals) is recorded and shown in Figure 4.8a. Of 458 high water mark stations, 315 were wetted in the model. Red dots on the map in figure 4.8a indicate 143 locations that did not experience inundation during the hindcast simulation of Hurricane Katrina. It is likely that a number of factors contribute to this type of error, i.e., erroneous values for local water depth and land height, not accounting for the decreased wind drag over water, or limitations in the inunndation mechanism of the model as previously documented in Section 3. Despite the non-wetting of certain locations, the model computed water elevations at the remaining 315 high water mark locations had an average error of only 1.2 feet (figure 4.8b). Stations with the largest errors underpredict water levels and are found near those same locations that remained erroneously dry. Note that dry area locations coincide with the limited inland inundation shown in the FEMA map of figure 4.7c. A spatial resolution in the model of 225m may have been too coarse to accuractly capture the wetting front in this region. Overall, the exhibited model skill is extraordinary, given that the hindcast only used readily available information on water depth, land height, and wind strength. The level of detail reflects typical conditions for Navy operations in non-US waters.

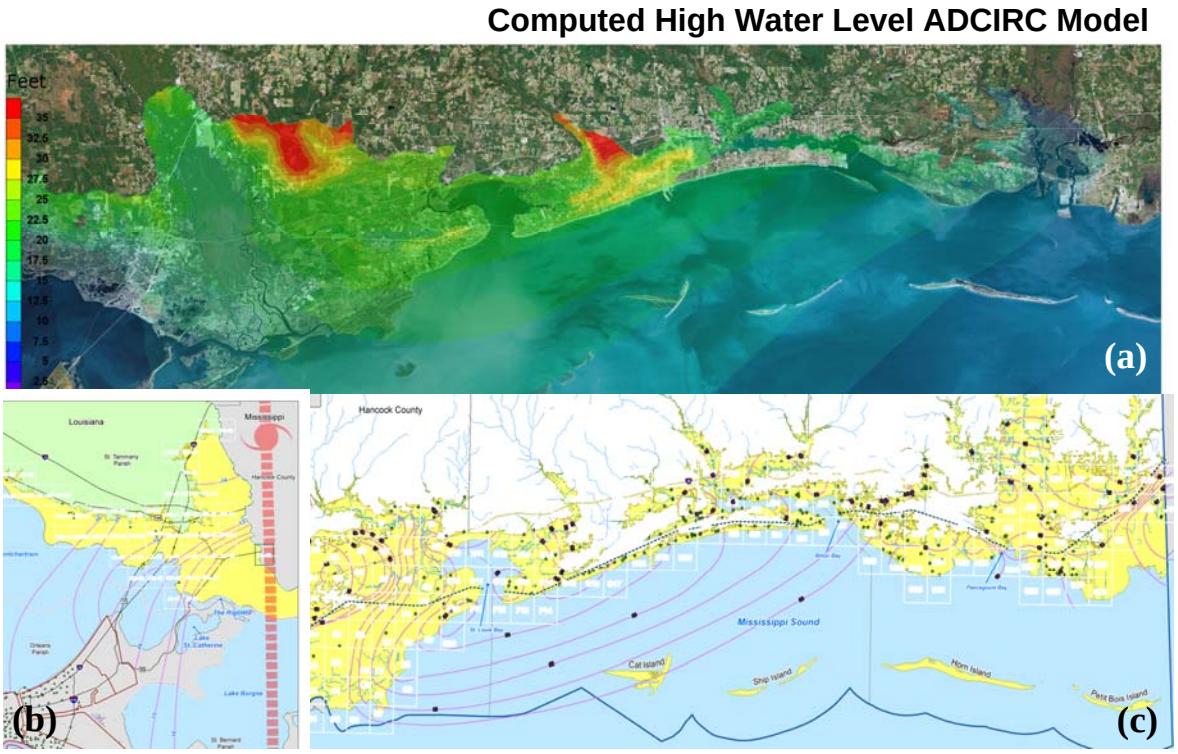

Figure 4.7: (a) A map of ADCIRC model-computed high water marks for Hurricane Katrina; (b) the FEMA Louisiana Hurricane Katrina Surge Inundation Map and c) the FEMA Mississippi Hurricane Katrina Surge Inundation Map.

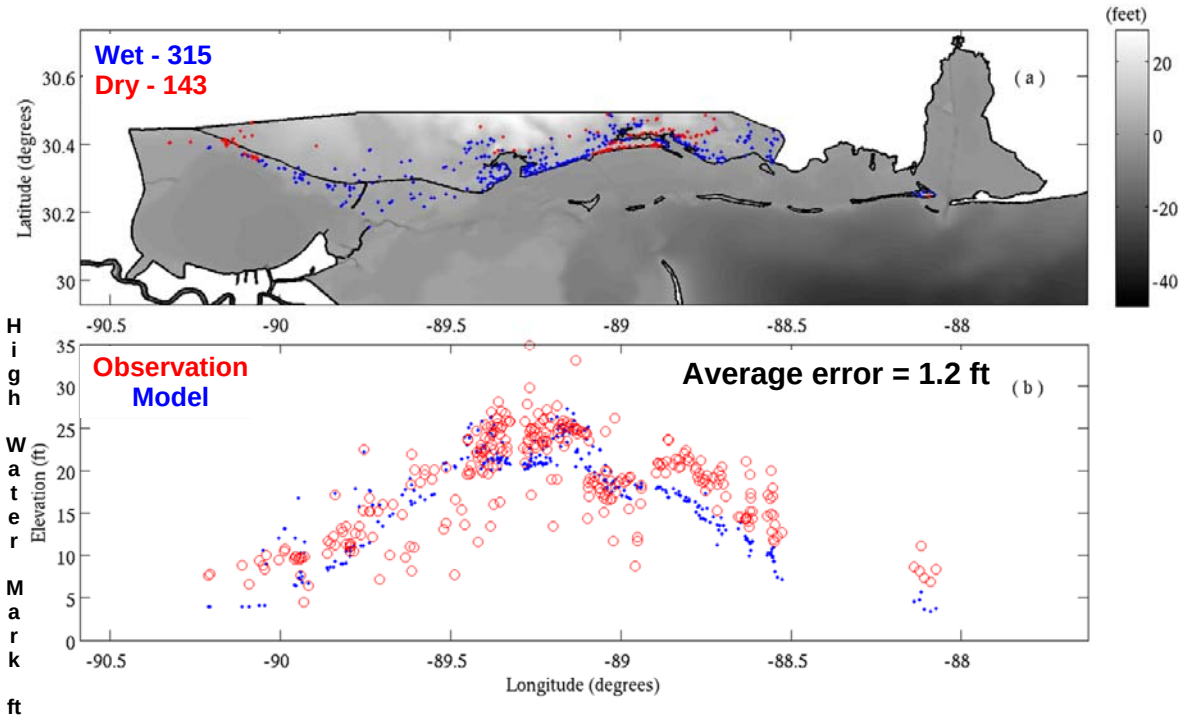

Figure 4.8: (a) A map of inundated (blue) or dry (red) U.S.G.S high water mark locations as computed by the model; (b) Comparisons of the modeled (blue) and measured (red) high water elevations in feet at 315 USGS stations.

d. Currents

The University of Southern Mississippi had deployed Buoy USM3m001 as an initial observing element of the Central Gulf of Mexico Ocean Observing System on December 13, 2004 at the location 30^{o} 02' 32.710''N and 88^{o} 38' 50.235''W (figure 4.9a). Data were telemetered every 3 hrs via Globalstar until it was recovered after hurricane Katrina in September of 2005. The eye of hurricane Katrina passed 49*nm* to the west of the 3*m* discus buoy, in 20 water depth, operated by the Central Gulf of Mexico Ocean Observing System. The buoy moved 2*km* to the northwest during the storm surge and then 13*km* to the southwest as the surge retreated (figure 4.9b). The buoy begins to drag its mooring when the significant wave height (SWH) exceeds 6*m* (A in figure 4.10). Buoy latitude reaches a maximum when the eye of Katrina shares the same latitude as the nominal buoy position (B in figure 4.10). Southward movement of the buoy stops when the significant wave height falls below 4*m* (C in figure 4.10). Waves built to nearly half the mean water depth and wave height rapidly decayed 5-6 hours after the hurricane moved over land.

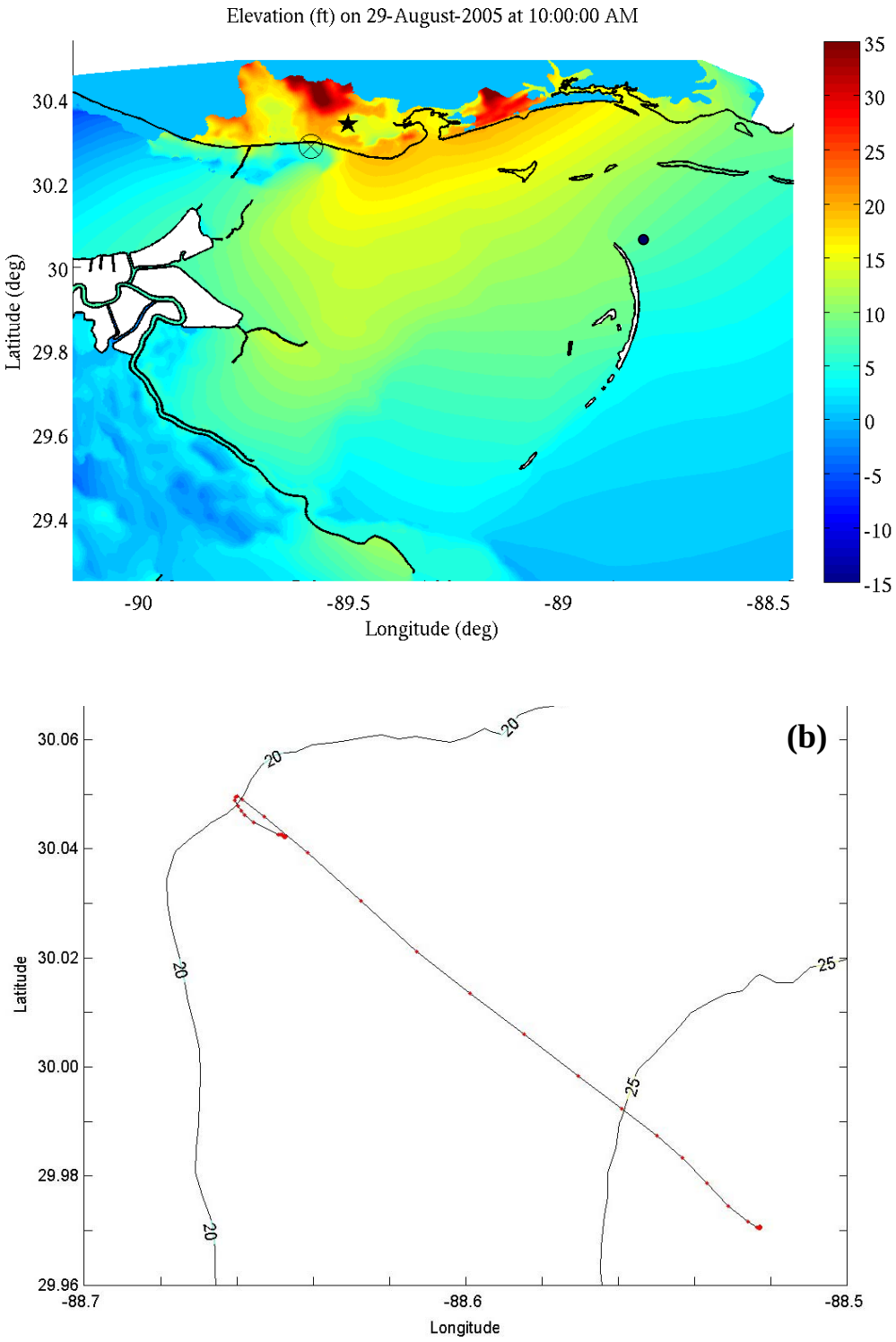

Figure 4.9: (a) The location of Buoy USM3m001 shown as a blue dot and (b) the northwestward movement of the buoy during hurricane Katrina, August 2005.

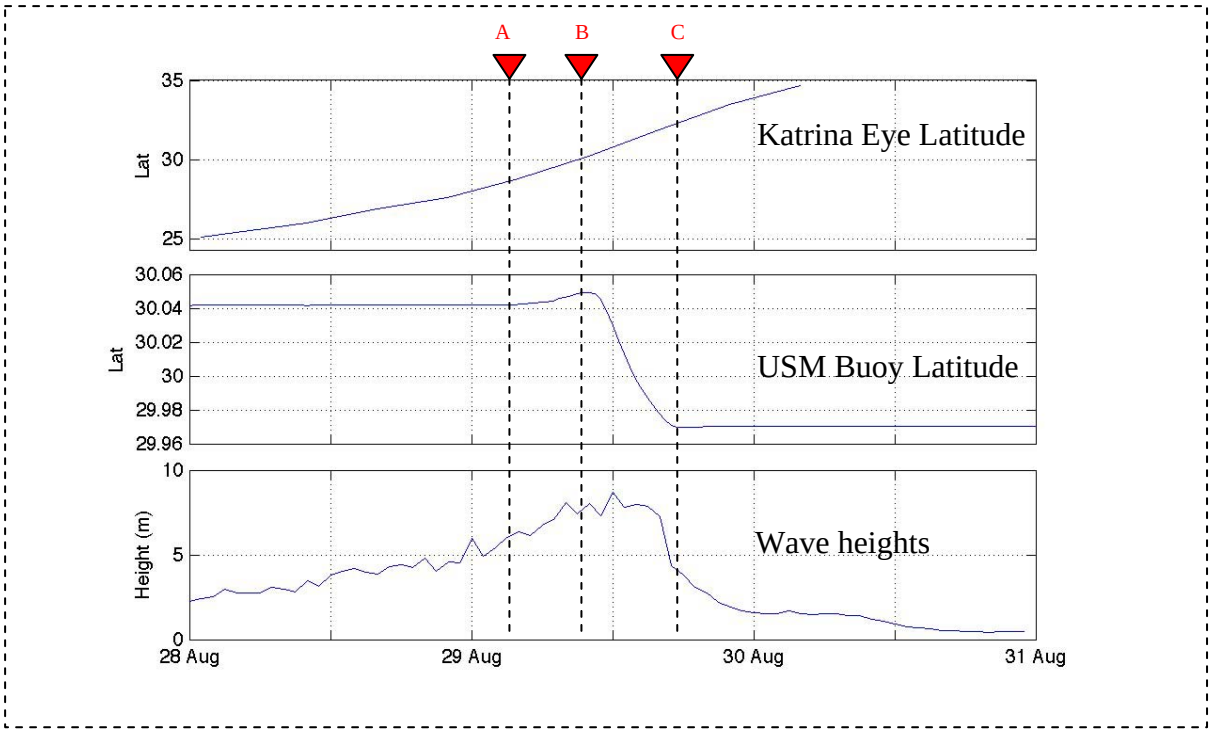

Figure 4.10: Time series of the latitude of Katrina's eye, the latitude of Buoy USM3m001 and the buoy measured significant wave heights. At A the buoy begins to drag the mooring when SWH > 6 m; at B, buoy latitude reaches a maximum when Katrina's eye is at the same latitude as nominal buoy position; at C, the buoy stops moving southward when SWH < 4 m.

Figure 4.11 compares the measured buoy wind stress to the computed stress as applied to the model at the location of the buoy. The wind stress applied to the model over-predicts the east-west component of the wind with the most significant over-prediction occurring just prior to landfall (figure 4.11a). The northward component of the wind stress applied to the model is slightly under-predicted at the peak but remains artificially elevated after the peak winds have passed (figure 4.11b).

Currents show an asymmetrical storm surge event with stronger currents during the fall of the surge (figure 4.11). Comparison of the buoy movement versus the ADCIRC currents (figure 4.12a), shows good agreement between the model and the observations once the buoy is moving along its southeast track. When considering the total currents (movement of the buoy plus the ADCP measured currents), the northwest currents leading up to the peak surge is well represented by the model. Immediately after landfall, the northward currents from the model track the observations but the eastward component never reaches the maximum observed currents and then begins to diminish while the observed currents continue to increase. Two potential causes can be attributed to this discrepancy. First, the model is forced with the NOAA reanalysis of the core circulation of the storm which does not include the far field winds that continue offshore beyond the time of storm landfall. Hence the model agrees reasonable well with the observations during the landfalling period of the storm but currents fall off rapidly after that point in time. Secondly, the model retained very high waters inland (recall figure 4.7a) due to shortcomings in the wetting and drying algorithm as exposed in section 3. Thus the model does not capture retreating waters as

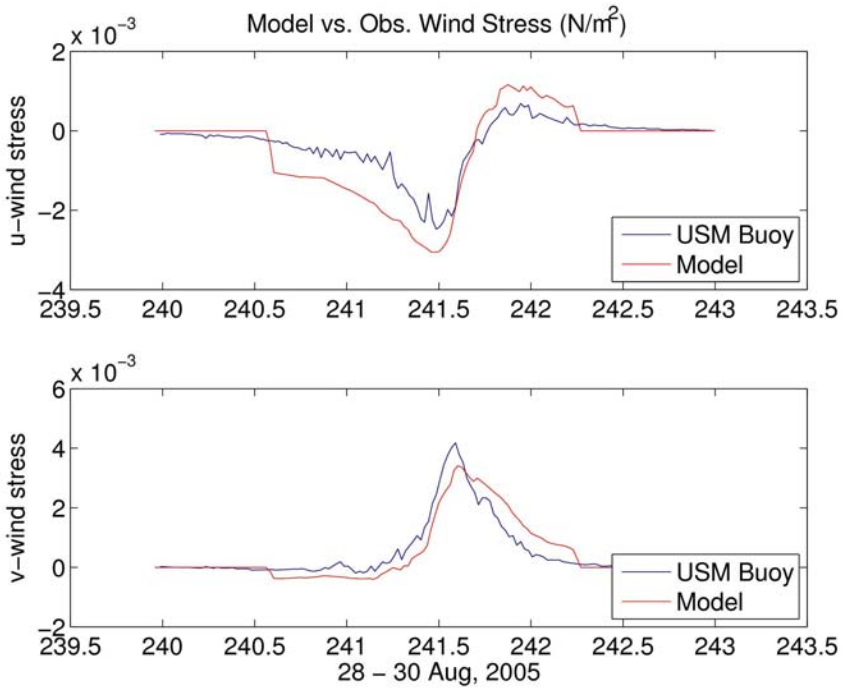

Figure 4.11: (a) Eastward wind stress observed (blue) and applied to the model (red); (b) Northward wind stress observed (blue) and applied to the model (red).

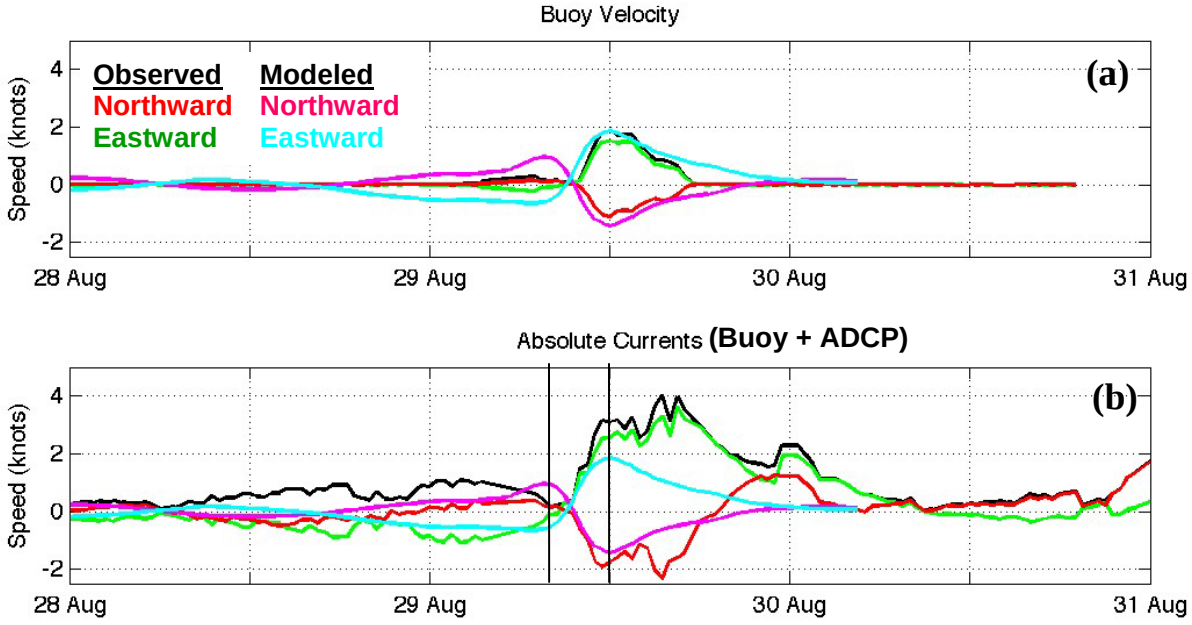

Figure 4.12: Northward (red) and eastward (green) movement of Buoy USM3m001 and the model computed northward and eastward components of the currents (magenta and cyan, respectively); (b) the total measured (buoy movement plus ADCP measured currents) and the modeled currents for the northward and eastward components (same color scheme).

evident by the buoy recorded currents. Figure 4.13 provides maps of the modeled current magnitudes and directions at two times during the observed storm event (indicted by black vertical lines on figure 4.12b.

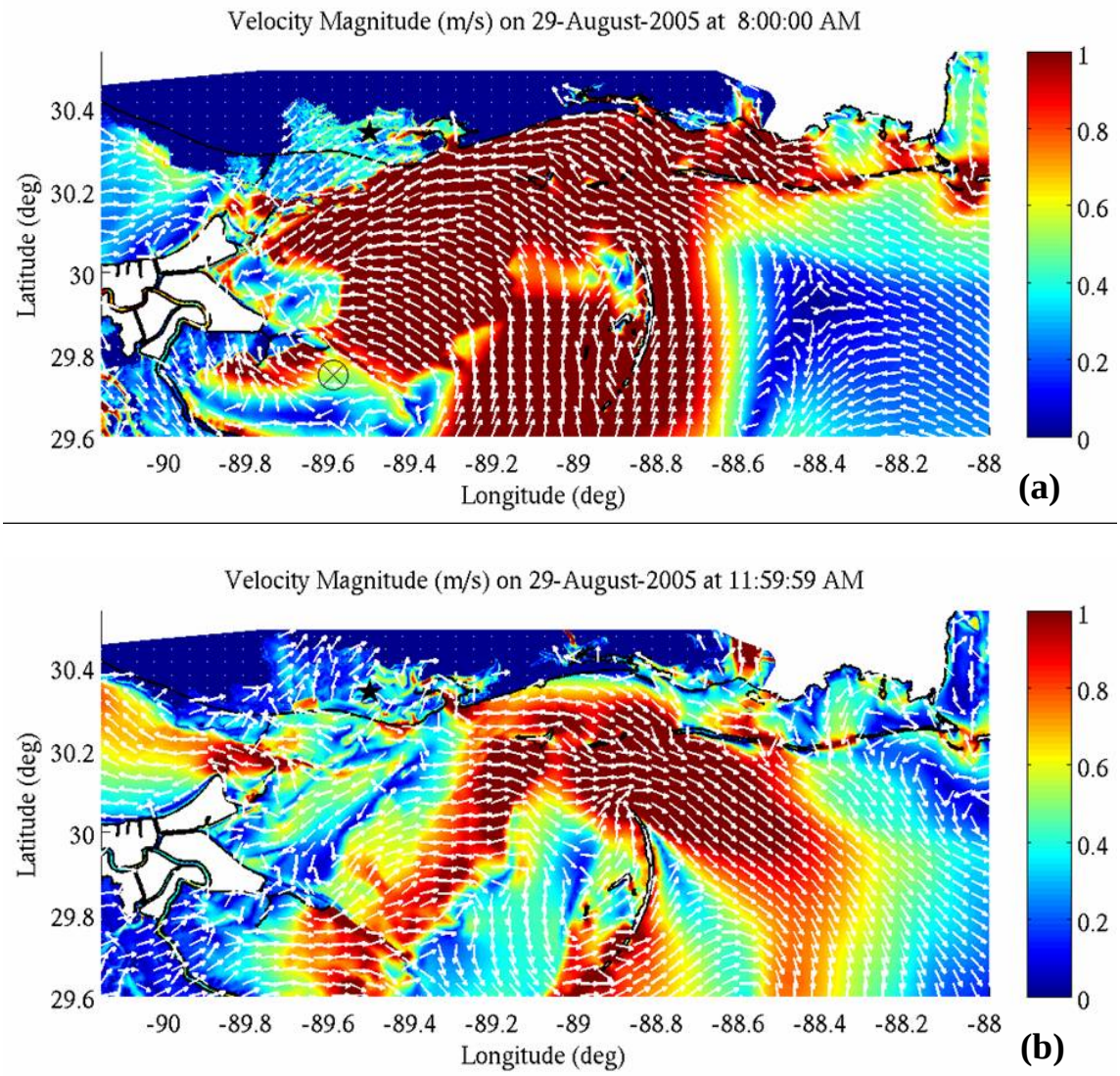

Figure 4.13: Modeled current magnitude (color) in *m/s* and direction (white arrows) at (a) 8:00 CDT 29 August 2005 and (b) 12:00 CDT 29 August 2005. These times are indicated by black lines in figure 4.13b.

e. Summary

The ability to rapidly apply the ADCIRC surge model to any location globally is the operational goal of the surge forecast prediction system. The mesh generation tool, MeshGUI, renders that goal of re-locateability possible. Experiences gained during the hindcast of Katrina have lead to upgrades in the MeshGUI tool. For example, a series of mesh quality adjustments are now automatically applied to a created mesh to eliminate

poorly constructed triangular elements that may cause model instabilities. Furthermore an estimate of model computational time is provided based on the size of a created mesh. The user can decide if iterations on the mesh design are needed knowing current operational constraints. Additionally, experience in creating the "Katrina" mesh indicates that a multi-stage mesh generation approach may be advantageous to balance resolution requirements and computational limitations in different regions of the mesh. For this approach the ability to "stitch" together different meshed regions was developed. Our own as well as others' experience modeling the inundation from Katrina indicates that fine scale information on overland elevation, vegetation type, and frictional characteristics are all very important for accurate represention of a wetting front. Methods are now being developed to automatically extract such information from remotely sensed imagery and utilize it in the mesh generation process.

Apart from the mesh generation process, our analyses of Hurricane Katrina surge and inundation hindcasts highlight improvements to the inundation methodology that could result in even more accurate, robust forecasts. For example, the movement of water inland would be better represented as a response to not only water elevation and frictional effects but also wind forcing. The conservation of water in overland regions that are wet, dried and rewet is another important aspect. In addition tracking and resolving the wet-dry interface could further enhance fidelity of the inundation forecast. Resolution of the mesh and representation of the bathymetry and topography as well as aresonable representation of the wind event are the most essential elements for accurate storm surge and inundation prediction.

5. Validation Test Results – Delaware Bay Tides and Currents

NOAA's National Ocean Service (NOS) is in the processes of evaluating oceanographic nowcast and forecast modeling systems to support navigational and environmental applications in U.S. coastal waters. In that context NOAA NOS has established the Delaware Bay benchmark for evaluating various model's performance using in-house developed skill assessment software. We adopt the same Delaware Bay benchmark for validation of the 3D barotropic ADCIRC model in the spirit of using community established benchmarks and to take advantage of the rich data set associated with this benchmark. The objectives of the Delaware Bay benchmark as applied here are 1) to validate and verify ADCIRC elevation and 2D and 3D current predictions against observational data and 2) to evaluate the model's response and associated uncertainty in an estuary setting under various forcing scenarios.

Delaware Bay is a major estuary of the U.S. east coast, surrounded by the states of Delaware, Pennsylvania and New Jersey. The length of the bay is about 75 km, has a maximum width of about 45 km with a mean depth of 10 m (figure 5.1a). The study area spans the distance from the Atlantic Ocean to Trenton, New Jersey. Water motions in the bay are dominated by tidal currents with M_2 the dominant tidal constituent. Delaware Bay adds a tidally-driven, shallow estuary with river contribution to the suite of validation benchmarks.

a. Model Configuration

The unstructured finite element grid shown in figure 5.1b consists of 15726 nodes and 28831 elements with resolution ranging from 50 meters at the upstream tributary area to 1000

meters at the offshore open boundary region. The domain includes the Delaware River, the Chesapeake and Delaware (C&D) Canal and extends out from the estuary into the Atlantic Ocean to depths of 100*m*. Forcing is applied in the form of 13 tidal harmonics (M_2, S_2, N_2, K_1, O_1, K_2, Q_1, M_4, M_6, MN_4, P_1, and $2SM_2$) along the model's open water boundary and at the C&D Canal. Values for the harmonic constants are taken from the 2001 ADCIRC East Coast database (EC2001) (Feyen and Yang, 2007). River discharge specified through ADCIRC's fort.20 file forced the head of the Delaware River. For most of the validation testing presented, the affects of meteorological forcing are ignored. Two short term simulations demonstrate the influence winds for the two dominant wind patterns, from the northwest and from the southeast.

The ADCIRC model was run for 190 day period in 1984, a time period during which 17 NOS water level gauges (figure 5.2a) and 44 current stations (figure 5.2b) recorded observations. A range of experiments were configured to examine different aspects of the model forcing (river discharge and wind) and bottom friction coefficient specification. For this later set of experiments used a spatially varying bottom friction coefficient as suggested by Walters (1997) such that a value of 0.0025 was specified in the bay and the friction increased to 0.04 upstream in the Delaware River. Table 1 presents a complete list of the numerical experiments. Experiments 1 to 6 focused on two-dimensional depth-integrated solutions from ADCIRC while experiments 7 to 12 were analyzing three-dimensional calculations. Standard statistical measurements were computed to evaluate model skill. The metrics include Mean Bias Error (MBE), Standard Deviation (SD), Root Mean Square Error (RSME) and Index of Agreement (AI) as defined by Blain (1997).

Table 5.1 Description of the 2D and 3D validation experiments for Delaware Bay.

Experiment No.	**Dimensionality**	**Description**	**Label**
1	2D	Baseline (constant river inflow)	2DCR
2	2D	No river inflow	2DNR
3	2D	Time-varying real river inflow	2DRR
4	2D	Spatially varying bottom friction	2DBF
5	2D	Dominant NW wind event at 12*m/s*	2DNW
6	2D	Dominant SE wind event at 12*m/s*	2DSE
7	3D	Baseline (constant river inflow)	3DCR
8	3D	No river inflow	3DNR
9	3D	Time-varying real river inflow	3DRR
10	3D	Spatially varying bottom friction	3DBF
11	3D	Dominant NW wind event at 12 *m/s*	3DNW
12	3D	Dominant SE wind event at 12 *m/s*	3DSE

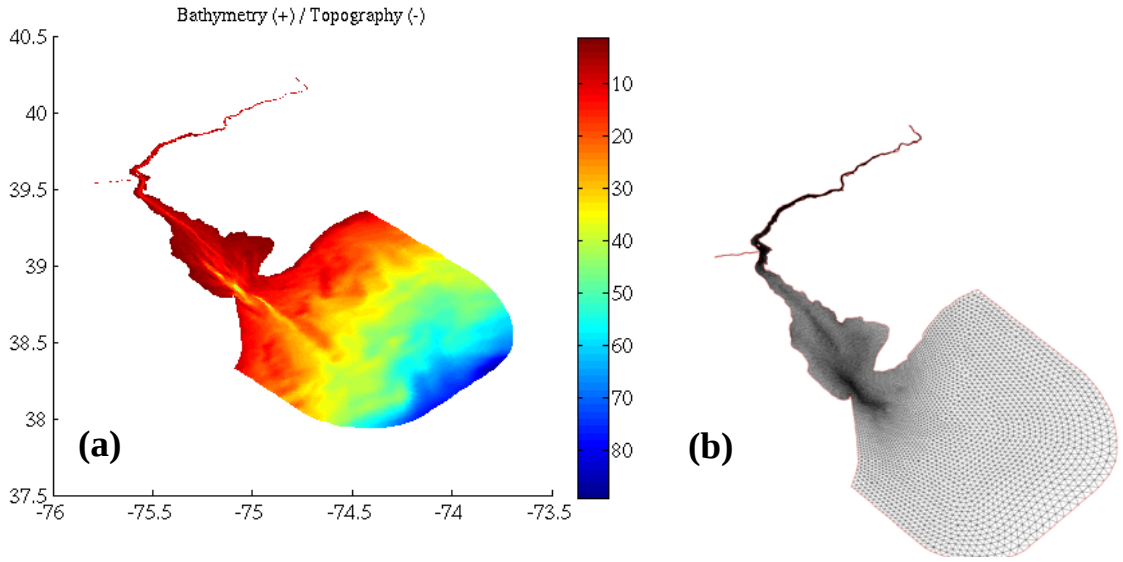

Figure 5.1: (a) Bathymetry contours in *m* for Delaware Bay and (b) the unstructured finite element mesh created for the same region as part of the NOAA's NOS Delaware Bay benchmark test case.

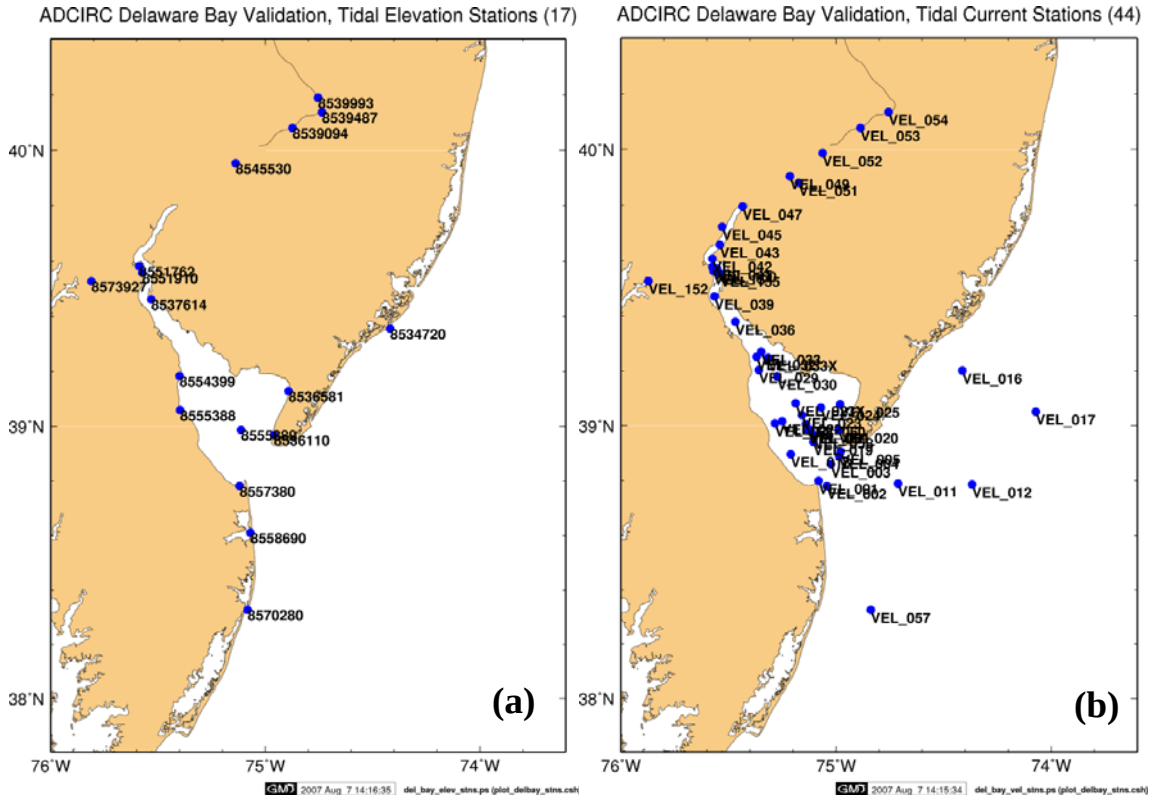

Figure 5.2: Locations of (a) 17 tide gauges and (b) 44 current meters associated with the NOAA Delaware Bay benchmark test case.

b. 2D Harmonic Tidal Elevations

Model-data comparisons for the baseline NOAA case (2D, constant river inflow, 2DCR) resulted in a small 0.018*m* error for the mean bias error (MBE) and a very high agreement index (AI) equal to 0.94. The influences of river discharge and bottom friction on predictive skill are then investigated for three different river inflow conditions (No River, Constant River, and Time-varying Real River) and variable bottom friction coefficients. Figure 5.3 and figure 5.4 compare four error measures, mean bias error (MBE), standard deviation (SD), mean absolute error (MAE), and root mean square error (RMSE), for each of eight elevation harmonic constituents in amplitude and phase, respectively. Overall, the dominate tidal constituent, M_2, has errors of about 6*cm*, an increase over the constant river inflow condition Errors of about 2*cm* are computed for the S_2, N_2, K_1 and M_4 constituents and approximately 1*cm* error for O_1, M_6 and MN_4 constituents relative to the 2DCR and 2DNR cases. Changing the bottom friction coefficient from 0.0025 to a spatially varying bottom stress produces the largest errors. For the M_2 constituent, MBE =- 0.20*m*, SD = 0.23 *m*, MAE = 0.22 *m*, RMSE = 0.30 *m* and AI= 0.35. All four cases (2DCR, 2DNR, 2DRR, 2DBF) have similar magnitudes for the phase error as seen in figure 5.4. There is a 10 degree variation for M_2, S_2, N_2, and O_1 and much more substantial phase errors in the range of 40 degrees for M_4, M_6, and MN_4, the shallow water quarter diurnal constituents.

The amplitude Agreement Index ranges from 0.8 to 0.95 for all constituents in each of the test cases having variants of the river forcing with the exception of the K_1 constituent. Varying the bottom stress resulted in notably lower AI scores. For phase, all cases tested have excellent phase agreement with observations according to the AI value which ranges from 0.95 to 0.99 for dominant as well as secondary constituents (figure 5.5).

Overall, whether no river discharge or a constant river discharge are specified all harmonic tidal elevation errors are quite similar. Adding a time-varying daily discharge which is more representative of reality did lead to slight improvements in the model-data comparisons. Spatially varying the bottom friction, as suggested by Walters (1997) to improve diurnal constituent representation, leads to large error with a negative bias indicating the model computations are very sensitive to the bottom friction coefficient. Increasing bottom friction heavily damped the elevation signal and degraded the comparison to observed water levels.

To investigate any spatial trends in the water level error, individual station errors are computed considering only the dominant tidal constituent, M_2. Table 5.2 summarizes the individual station errors for each experiment. These same errors are graphically depicted in figure 5.6.The 17 stations are grouped into three categories depending on their location to see if any trend or bias can be found. Four stations are in the estuarine category (8539993, 8539487, 8539094, 8545530) indicating primary influence of the Delaware River, eight stations are in the bay category (8551762, 8551910, 8573927, 8537614, 8554399, 8555388, 8536581, 85555889), and five stations (8534720, 8536110, 8557380, 8558690, 8570280) are identified as offshore near the open ocean boundary. For the constant river flow case, the model under-predicts water level at estuarine and bay stations while over-estimating water height at open ocean stations. But for the 2DNR and 2DRR experiments, the model over-predicts at estuarine and open ocean stations and still slightly under-predicts water level at the bay stations. For the 2DBF case, the model under-estimated water levels at all but two stations.

Among all 17 stations, the largest magnitude errors are located at Trenton (8539993),

Artificial Island (8537614) and Indian River Inlet (8558690). Errors at these three stations are at least one order of magnitude larger than errors at the remaining stations. The probable cause for the large error at Indian River Inlet (found outside the Bay along the western shoreline) is the complex inlet geometry not currently included in the model grid. Additionally, discharge from the Indian River is not incorporated as forcing. At the Trenton station (located at the northeastern most point of the Delaware River) error is due to the variability in the Delaware river flux. When a time-varying river flux is applied as forcing, the error reduces from 10*cm* down to 1*cm*. Similar errors are computed for the constant and no river flux forcing cases. Errors at Artificial Island located just south of the Chesapeake & Delaware Canal are due to combined errors in the forcing specified for both the Delaware River and the C&D canal. A spatially varying bottom friction still creates the largest errors at nearly every station, especially in the estuarine and bay regions where bottom friction coefficients are higher.

Table 5.2 2D tidal elevation errors for the M_2 tide at 17 water level stations for all experiments.

Location	**StationID**	**2DCR**	**2DNR**	**2DRR**	**2DBF**
Trenton*	8539993	-0.1065	0.0687	0.0150	-0.8595
Fieldsboro	8539487	-0.0066	0.1484	0.1092	-0.7280
Burlington	8539094	-0.0532	0.0694	0.0563	-0.6832
Philadelphia	8545530	-0.0483	0.0407	0.0441	-0.2364
Delaware City	8551762	-0.0629	-0.0372	-0.038	-0.1796
Reedy Pt.	8551910	-0.0784	-0.0599	-0.0623	-0.1880
Chesapeake City	8573927	-0.0090	-0.0132	-0.0142	-0.0039
Artificial Island	8537614	-0.1654	-0.1354	-0.1377	-0.2805
Mahon Riv	8554399	0.0007	0.0360	0.0384	-0.1500
Murderkill Riv	8555388	0.0359	0.0702	0.0695	-0.1235
Bidwell Creek	8536581	-0.0013	0.0349	0.0346	-0.1671
Brandywine	8555889	-0.0003	0.0276	0.0274	-0.1326
Atlantic City	8534720	0.0036	0.0036	0.0036	0.0036
Cape May Canal	8536110	0.0069	0.0332	0.0331	-0.1120
Lewes	8557380	0.0153	0.0328	0.0327	-0.066
Indian Riv Inlet	8558690	0.1825	0.1852	0.1852	0.1674
Ocean City	8570280	0.0105	0.0106	0.0106	0.0105

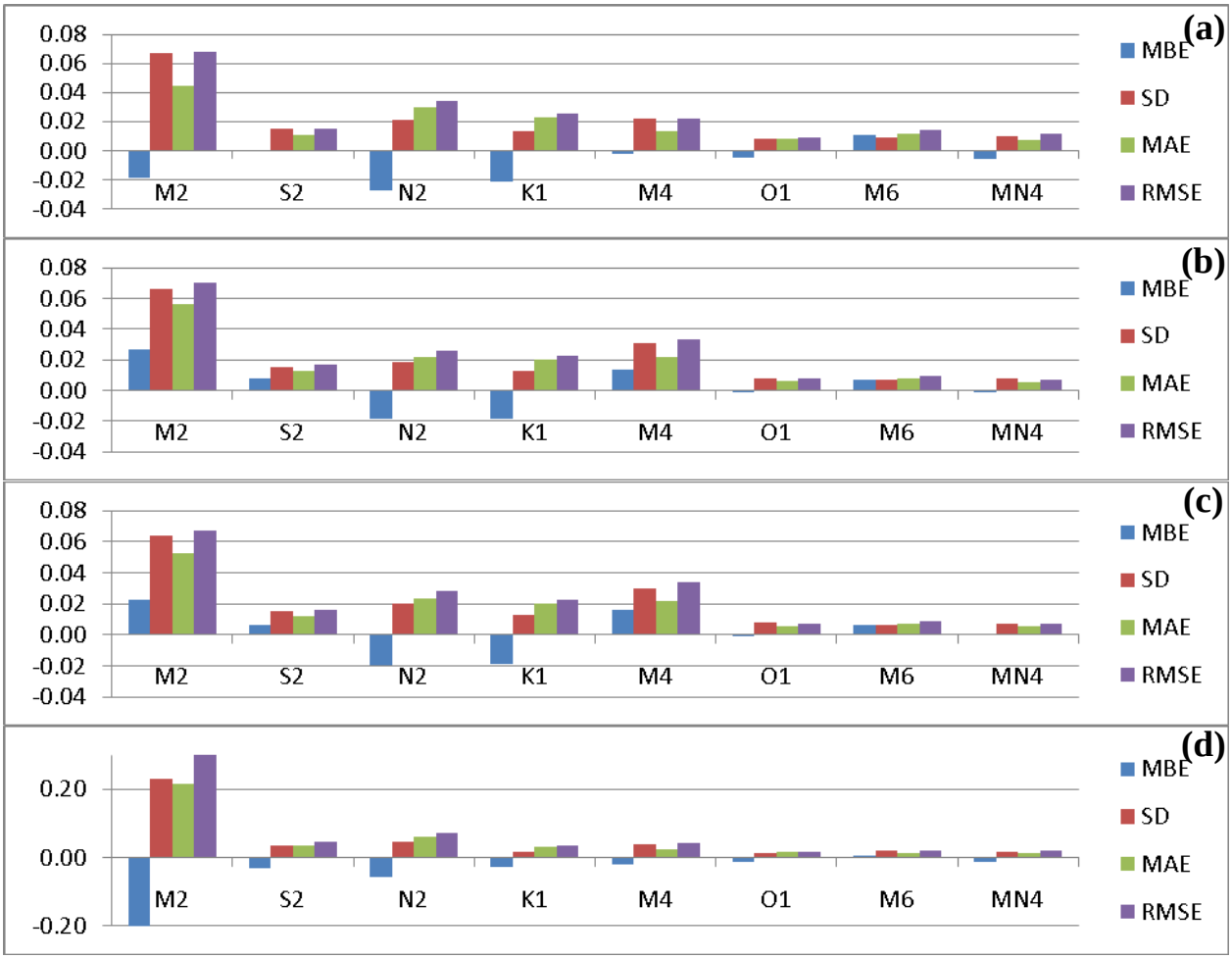

Figure 5.3: Four 2D amplitude error measures, mean bias error (MBE), standard deviation (SD), mean algebraic error (MAE), and root mean square error (RMSE), for each of 8 water level harmonic tidal constituents for the (a) 2DCR, (b) 2DNR, (c) 2DRR, and (d) 2DBF experiments.

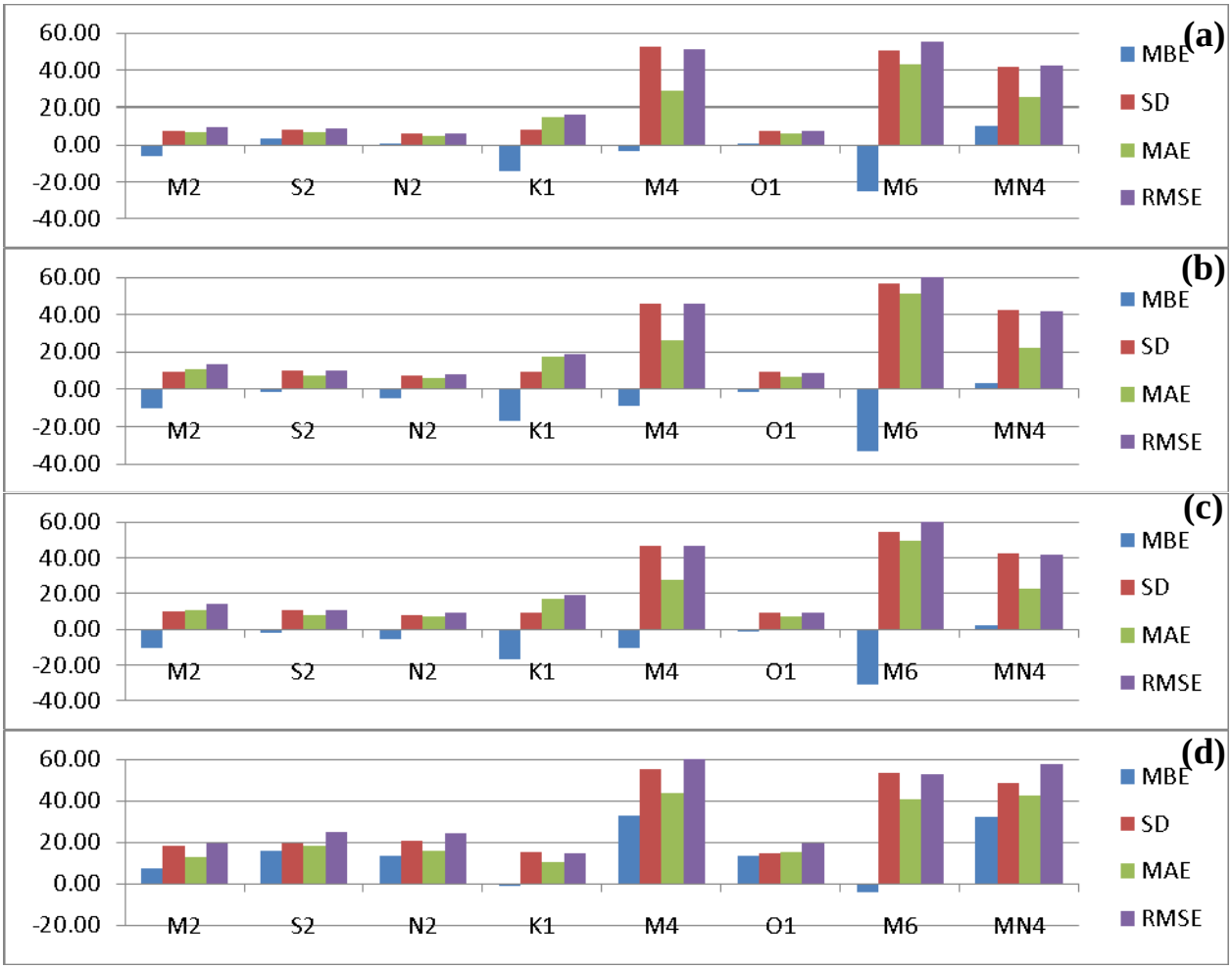

Figure 5.4: Four 2D phase error measures, mean bias error (MBE), standard deviation (SD), mean algebraic error (MAE), and root mean square error (RMSE), for each of 8 water level harmonic tidal constituents for the (a) 2DCR, (b) 2DNR, (c) 2DRR, and (d) 2DBF experiments.

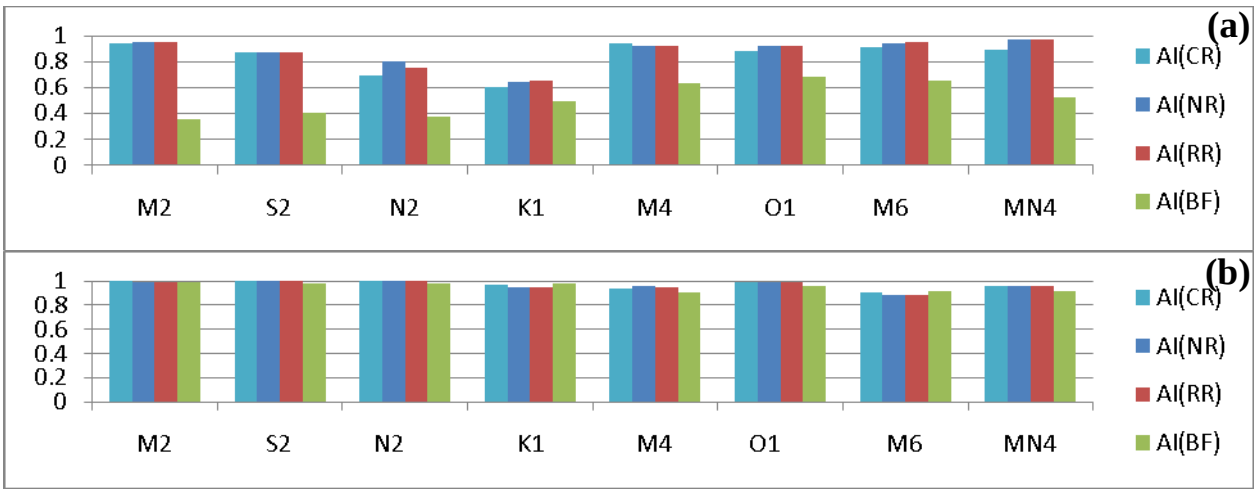

Figure 5.5: The 2D Index of Agreement (AI) elevation (a) amplitude and (b) phase for each of 8 water level harmonic tidal constituents for the 2DCR, 2DNR, 2DRR, and 2DBF experiments.

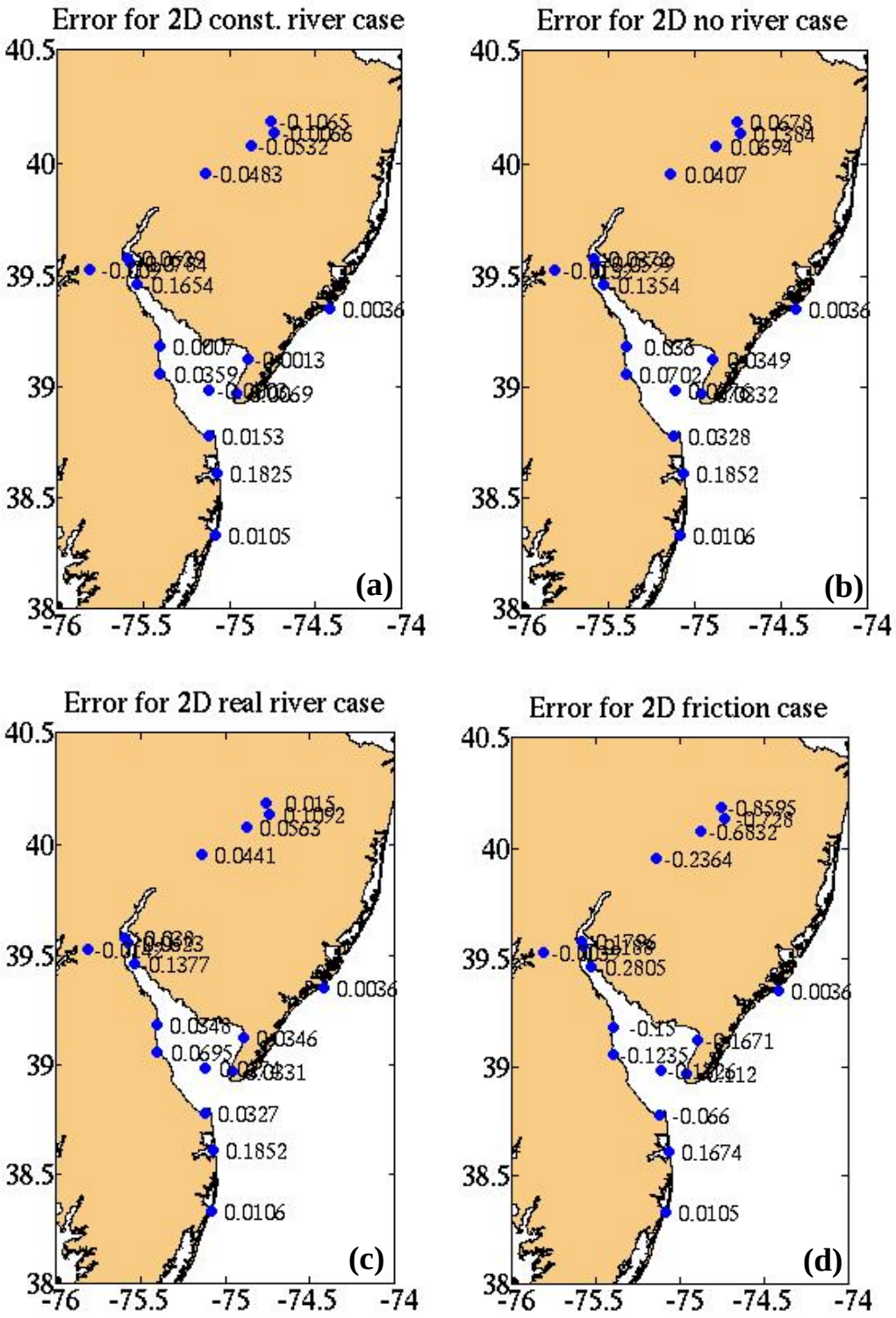

Figure 5.6: The M_2 elevation MBE for amplitude from each of the 2D experiments (a) 2DCR, (b) 2DNR, (c) 2DRR, and (d) 2DBF.

c. 3D Harmonic Tidal Elevations

A similar analysis as outlined in section 5b was conducted using results from the 3D ADCIRC computations. Amplitude and phase errors for 8 constituents over 4 3D model experiments are shown in figures 5.7 and 5.8. For the 3D experiments, errors increase for the M_2 (10*cm*) and M_4 (5*cm*) constituents when compared with the 2D results. The baseline (2DCR) experiment, had errors for the M_2 tidal constituent as follows: a MBE of -0.0028*m*, SD of 0.104*m*, MBE of 0.0812*m*, an RMSE of 0.102*m* and an AI value of 0.849. The lowest error values are recorded for the 3DRR experiment for the M_2 tidal constituent when compared to the other experiments and follows the same trend as the 2D error analysis. In contrast notably larger errors are associated with the S_2 amplitude for the 3DRR test case. Other constituents (N_2, K_1, M_4, O_1, M_6 and MN_4) exhibit similar statistical scores for all test cases though errors are increased for the higher harmonics (M_4, M_6 and MN_4). Phase errors in all experiments are under 10 degrees with the exception of the higher harmonics (M_4, M_6 and MN_4). No significant differences in the phase error are evident among the test cases. The Agreement Index for amplitude and phase for the 3D experiments are provided in figure 5.9. Values of the AI are quite similar to those computed from the 2D model data except for the quarter-diurnal constituents, M_4 and MN_4. All constituents in 3D runs also show excellent phase agreement with AI ranges from 0.9 to 0.99.

Station by station error values for 17 water level stations are listed in Table 5.3 for the M_2 tide for all experiments. For 3D experiments the largest errors occur at the estuarine stations (Trenton, Fieldsboro and Burlington) for the 3DCR, 3DNR, and 3DBF test cases. Error magnitudes for the 3DCR and 3DNR are similar at most stations. Significant improvement is evident at the 4 estuarine stations for the 3DRR but no improvement is seen at either the bay or open ocean stations. When comparing differences between the 2D and 3D constant river flow case, the 2DCR actually has smaller errors at the estuarine stations than the 3D case. From this set of experiments, the 3D model performs best for the river forcing that represents the more realistic time-varying river discharge.

Spatially, the 3DCR, 3DNR, and the 3DBF experiments show under-prediction at the estuarine stations and over-prediction at the open ocean stations. The exception is the 3DRR which has a positive bias for all estuarine stations.

Table 5.3 3D tidal elevation errors for the M_2 tide at 17 water level stations for all experiments.

Location	StationID	3DCR	3DNR	3DRR	3DBF
Trenton*	8539993	-0.2502	-0.2546	0.0180	-0.2502
Fieldsboro	8539487	-0.1695	-0.1746	0.0934	-0.1695
Burlington	8539094	-0.1931	-0.2124	0.0394	-0.1931
Philadelphia	8545530	-0.090	-0.1409	0.0621	-0.090
Delaware City	8551762	-0.0013	0.0075	0.0271	-0.0013
Reedy Pt.	8551910	-0.0158	-0.0082	-0.0066	-0.0158
Chesapeake City	8573927	-0.010	-0.011	-0.0090	-0.0102
Artificial Island	8537614	-0.1067	0.0986	-0.0916	-0.1067
Mahon Riv	8554399	0.0646	0.0673	0.0827	0.0646
Murderkill Riv	8555388	0.1109	0.1124	0.1278	0.1109
Bidwell Creek	8536581	0.0723	0.0731	0.0875	0.0723
Brandywine	8555889	0.0718	0.0724	0.0815	0.0718
Atlantic City	8534720	0.0036	0.0036	0.0036	0.0036
Cape May Canal	8536110	0.0666	0.0670	0.0812	0.0666
Lewes	8557380	0.0512	0.0513	0.0580	0.0512
Indian Riv Inlet	8558690	0.1795	0.1794	0.1802	0.1795
Ocean City	8570280	0.0104	0.0104	0.0104	0.0104

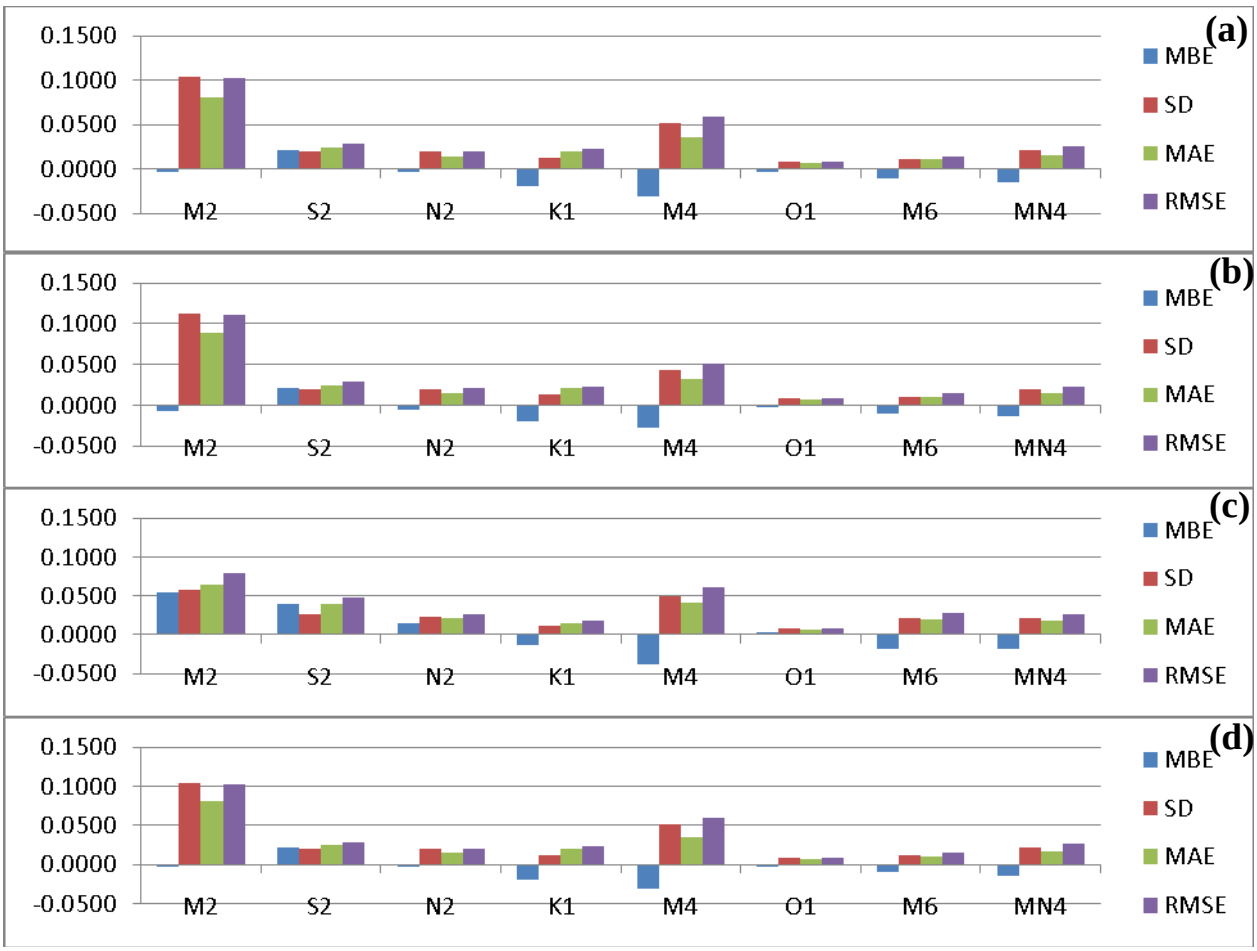

Figure 5.7: Four 3D amplitude error measures, mean bias error (MBE), standard deviation (SD), mean algebraic error (MAE), and root mean square error (RMSE), for each of 8 water level harmonic tidal constituents for the (a) 3DCR, (b) 3DNR, (c) 3DRR, and (d) 3DBF experiments.

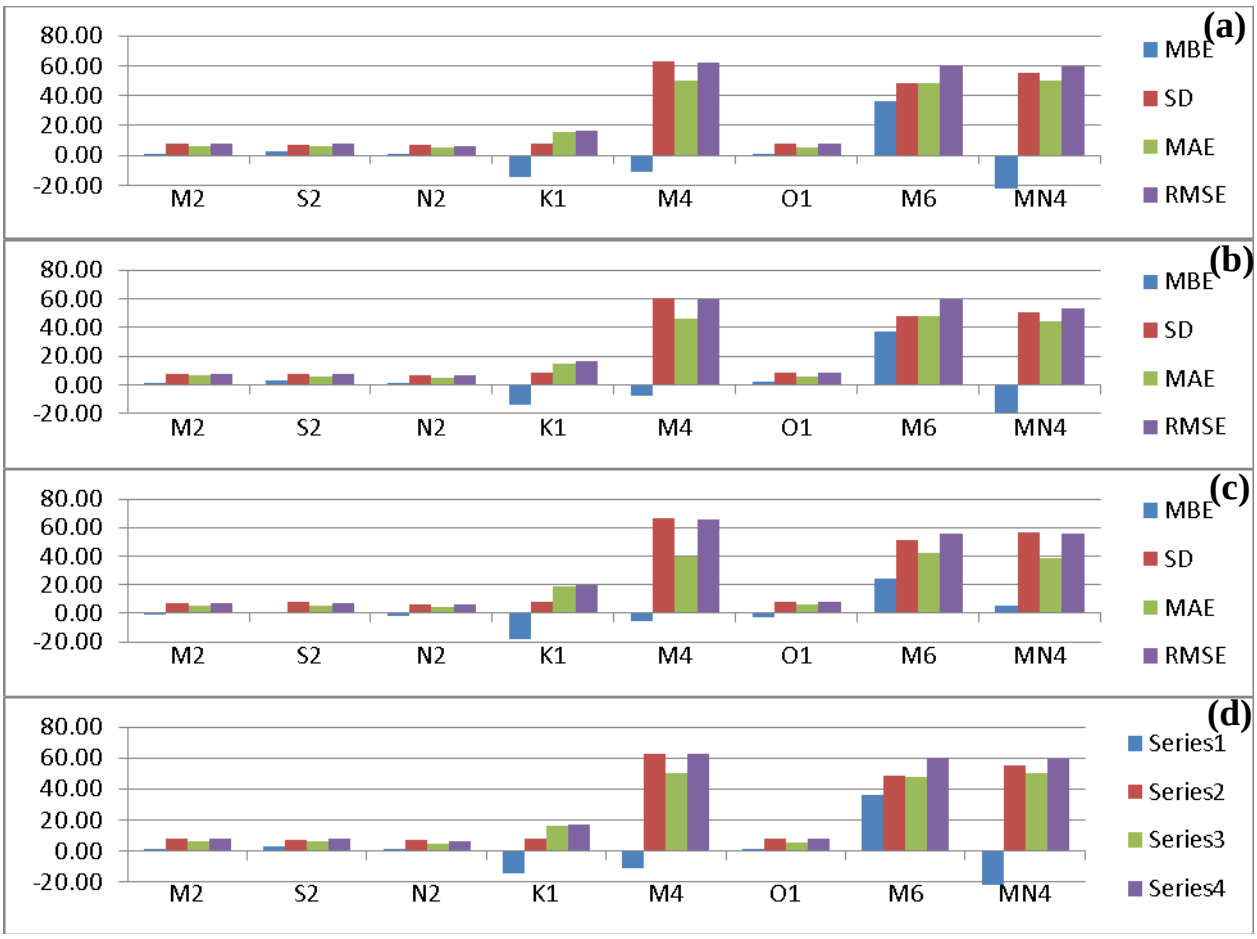

Figure 5.8: Four 3D phase error measures, mean bias error (MBE), standard deviation (SD), mean algebraic error (MAE), and root mean square error (RMSE), for each of 8 water level harmonic tidal constituents for the (a) 3DCR, (b) 3DNR, (c) 3DRR, and (d) 3DBF experiments.

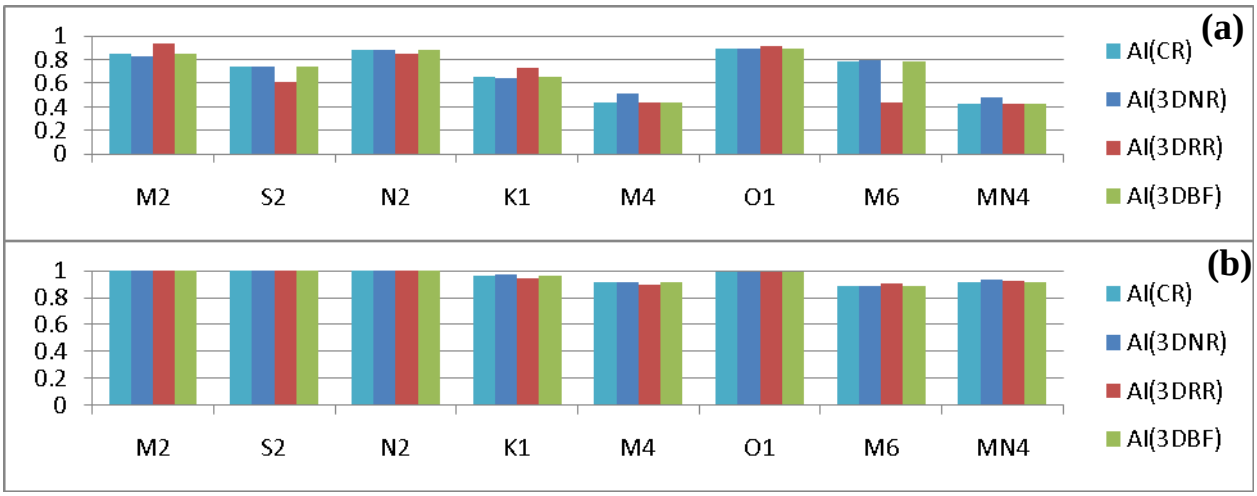

Figure 5.9: The 3D Index of Agreement (AI) for elevation (a) amplitude and (b) phase for each of 8 water level harmonic tidal constituents for the 3DCR, 3DNR, 3DRR, and 3DBF experiments.

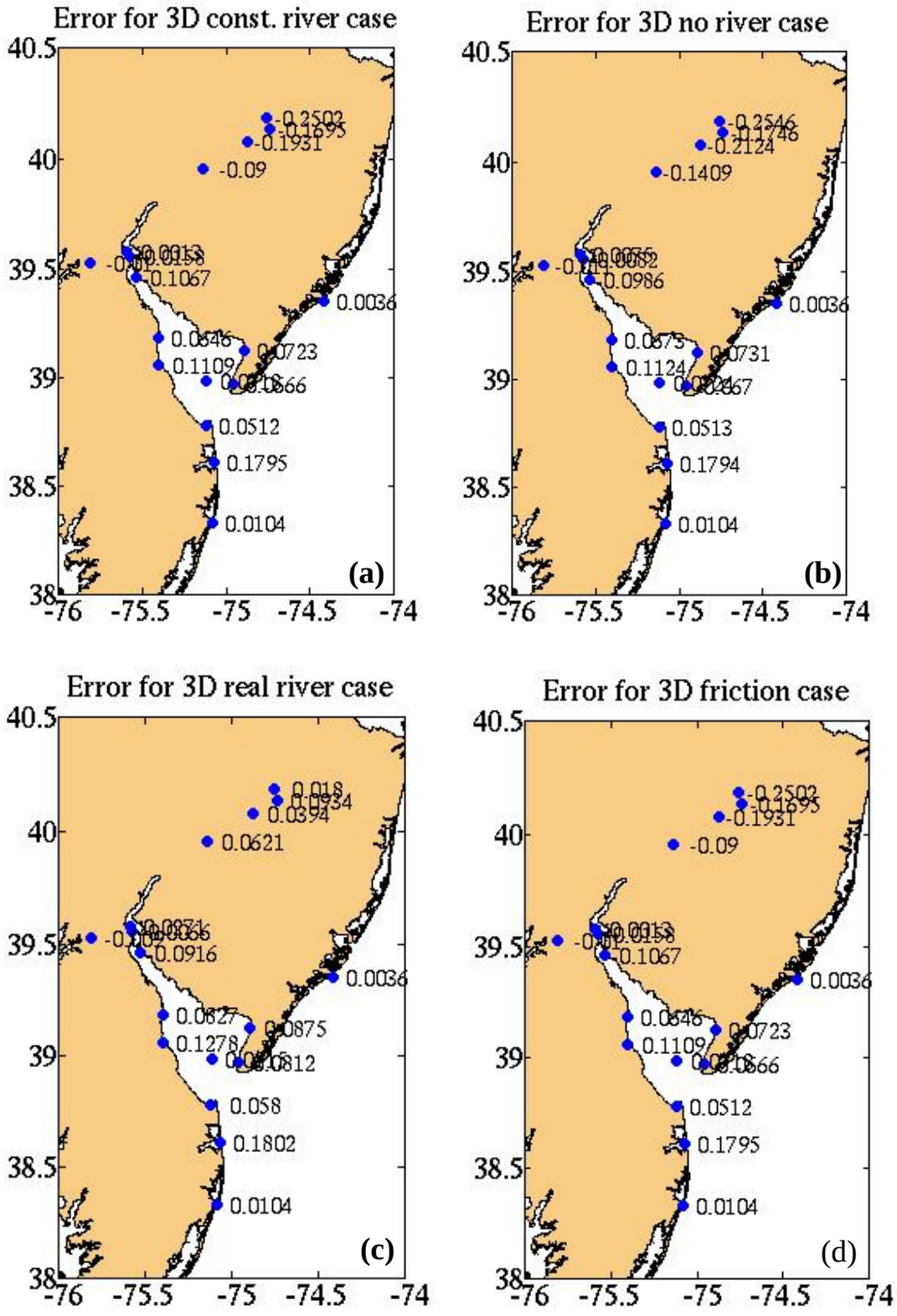

Figure 5.10: The M_2 elevation MBE for amplitude from each of the 3D experiments (a) 3DCR, (b) 3DNR, (c) 3DRR, and (d) 3DBF.

d. 2D Harmonic Tidal Currents

Statistical analyses of the harmonic constituent amplitudes and phases of 2D currents are presented for the four experiments, 2DCF, 2DNR, 2DRR, and 2DBF. The constant river flow case (2DCR) is used as a benchmark and is compared against the other three test cases. The average errors are 20*cm/s* for M_2 and 5*cm/s* for the remaining constituents. Specification of a spatially variable bottom friction once again yields larger MBE and RMSE values as it over-damps the velocity in the water column. All current tidal constituents for each of the four test cases had phase errors ranging from 70 to 120 degrees with no significant differences regardless of the river forcing or the spatially variable bottom friction specification. Some of the phase error may be attributed to inconsistencies in the axis orientation used for comparing observations and modeled results. (The dominant M_2 tide enters the estuary at 110 degree from true north, with a clockwise rotation. Observations are processed using the true north/east directions while the skill assessment software may decompose the currents to major/minor axis. A 110 degree phase shift in the modeled major/minor axis results in phases errors of 20-30 degree which is more in keeping with the known model skill.

The temporally varying real river simulation provided the best overall statistical skill. For 2DRR, the M_2 amplitude had the smallest MBE; it also had the smallest SD, MAE, RSME and highest AI among all four cases for most of the tidal constituents. 2DCR and 2DNR yielded comparable statistical numbers while the varying bottom case (2DBF) generated larger MBE, RSME and lowest AI for the M_2 amplitude. Figure 5.11 shows the AI score ranging from 0.6 to 0.8 for current amplitude and phase.

The spatial distribution of M_2 current errors are presented in figure 5.12. Unlike the water level errors discussed in the previous sections, large errors for the currents are concentrated in the upper bay where maximum velocities usually occur in conjunction with complex stratification and mixing processes. For 2DCR, open ocean stations have the smallest error, between 3*cm* and 5*cm*, estuarine stations have errors between 5 and 15*cm* while errors at bay stations are as high as 60*cm*. By incorporating the realistic time-varying river flow, velocity errors are reduced in both the estuarine and bay regions. No improvement is observed for the 2DBF case, despite the increased bottom friction in the estuarine and bay regions.

Figure 5.11: The 3D Index of Agreement (AI) for current (a) amplitude and (b) phase for each of 8 water level harmonic tidal constituents for the 3DCR, 3DNR, 3DRR, and 3DBF experiments.

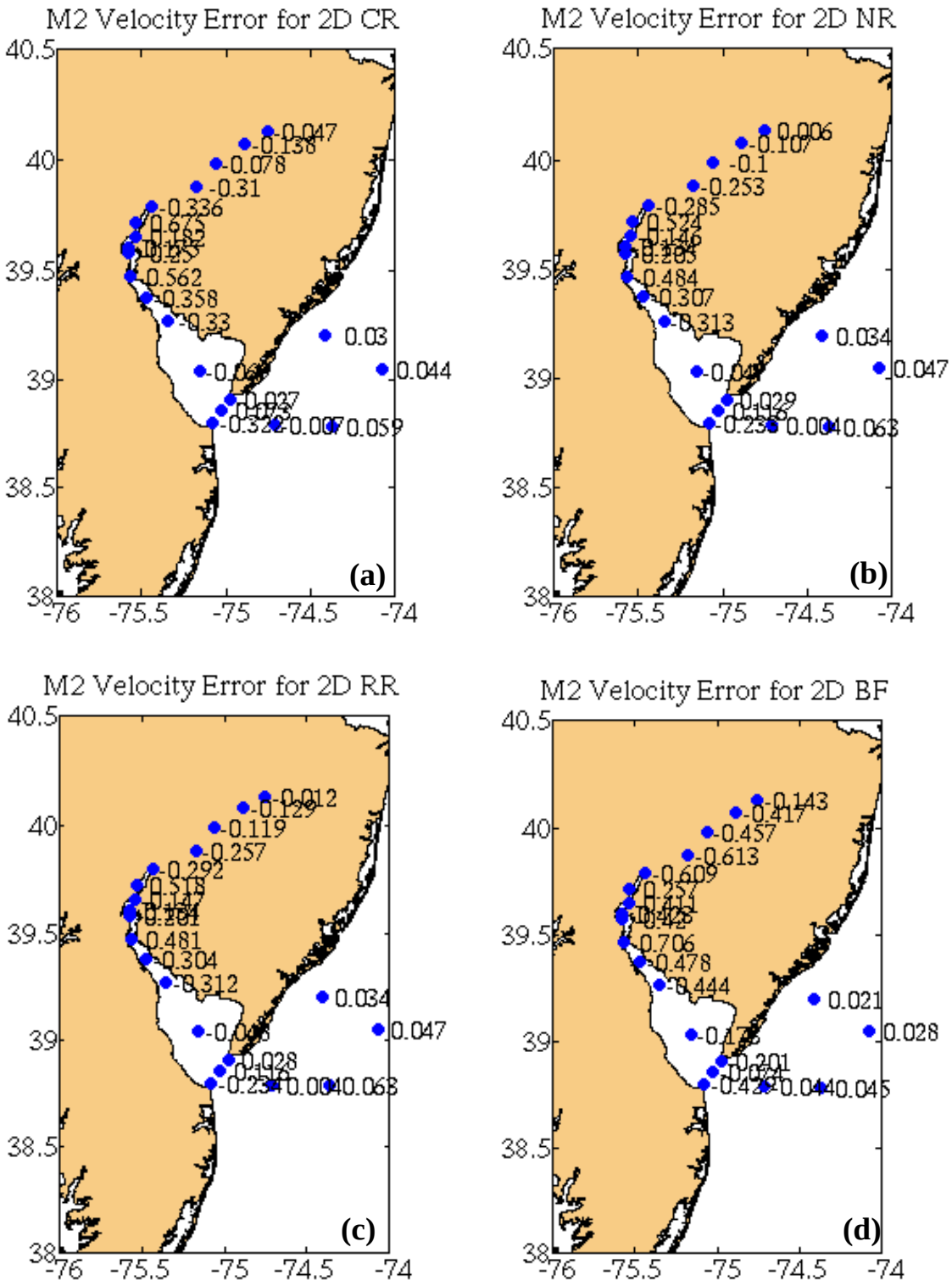

Figure 5.12: The M_2 velocity MBE for each of the 2D experiments (a) 2DCR, (b) 2DNR, (c) 2DRR, and (d) 2DBF.

e. 3D Harmonic Tidal Currents

Average errors for the model representation of 3D currents in the constant river case are 20*cm/s* for M_2 and 5*cm/s* for the rest of constituents, the same magnitude of error as for the 2D simulation. Variable bottom friction, 3DBF, results in larger MBE and RMSE values. All constituents in each of the four cases have phase errors ranging from 100 to 150 degrees with no significant differences observed between the various experiments. Once again, the realistic river inflow (3DRR) demonstrated the best model skill. The AI values for current amplitudes from the 3DRR experiment are higher than the remaining three test cases in 9 of 13 constituents, including the major M_2, S_2, N_2 and K_1 constituents (see figure 5.13). The AI for current phase for the 3DRR experiment is also higher for 8 of 13 constituents when compared with other three test cases. 3DRR also has the smallest SD, MAE, RSME and highest AI among all four cases for most of the tidal constituents. The 3DCR and 3DNR cases yield comparable statistical errors while the varying bottom case (3DBF) still results in larger MBE and RSME and the lowest AI values. AI values for current amplitudes range from 0.6 to 0.8 while AI for current phases have a wider range from 0.4 to 0.8 in figure 5.13. The error analyses have shown the importance of the inclusion of realistic river discharge in both the 2D and 3D model computations, even model computations neglecting density contributions.

Spatially the errors for the 3DCR test case showed a reduction in the model-data error in the upper bay region, but not in the estuarine section when compared with errors computed using the 2D solution for the same forcing (see figure 5.14). The 3DRR case had the smallest errors in both the estuarine and bay regions as compared with the 2DCR, 2DRR and the 3DCR experiments.

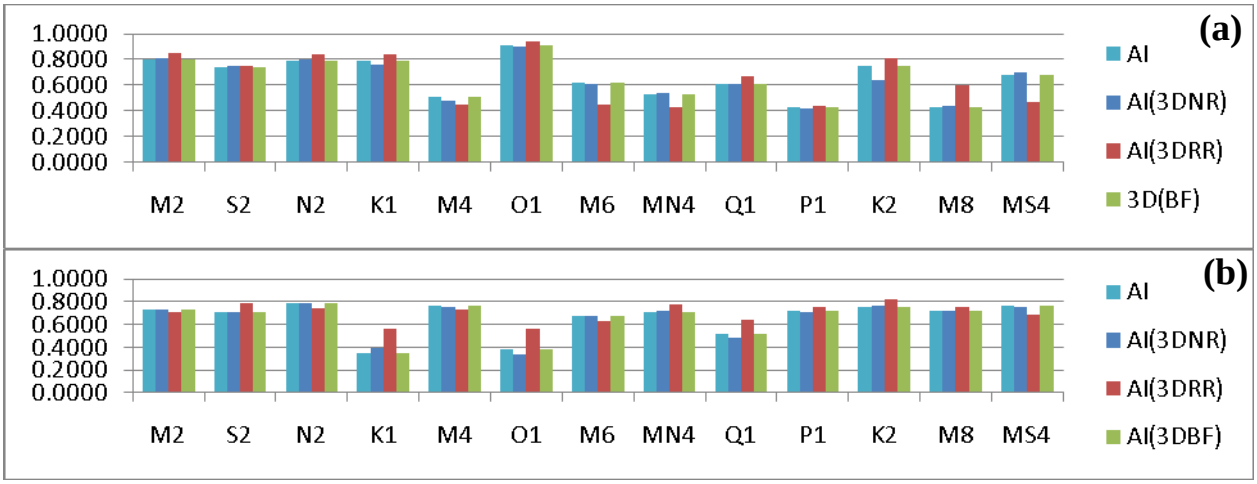

Figure 5.13: The 3D Index of Agreement (AI) for current (a) amplitude and (b) phase for each of 8 water level harmonic tidal constituents for the 3DCR, 3DNR, 3DRR, and 3DBF experiments.

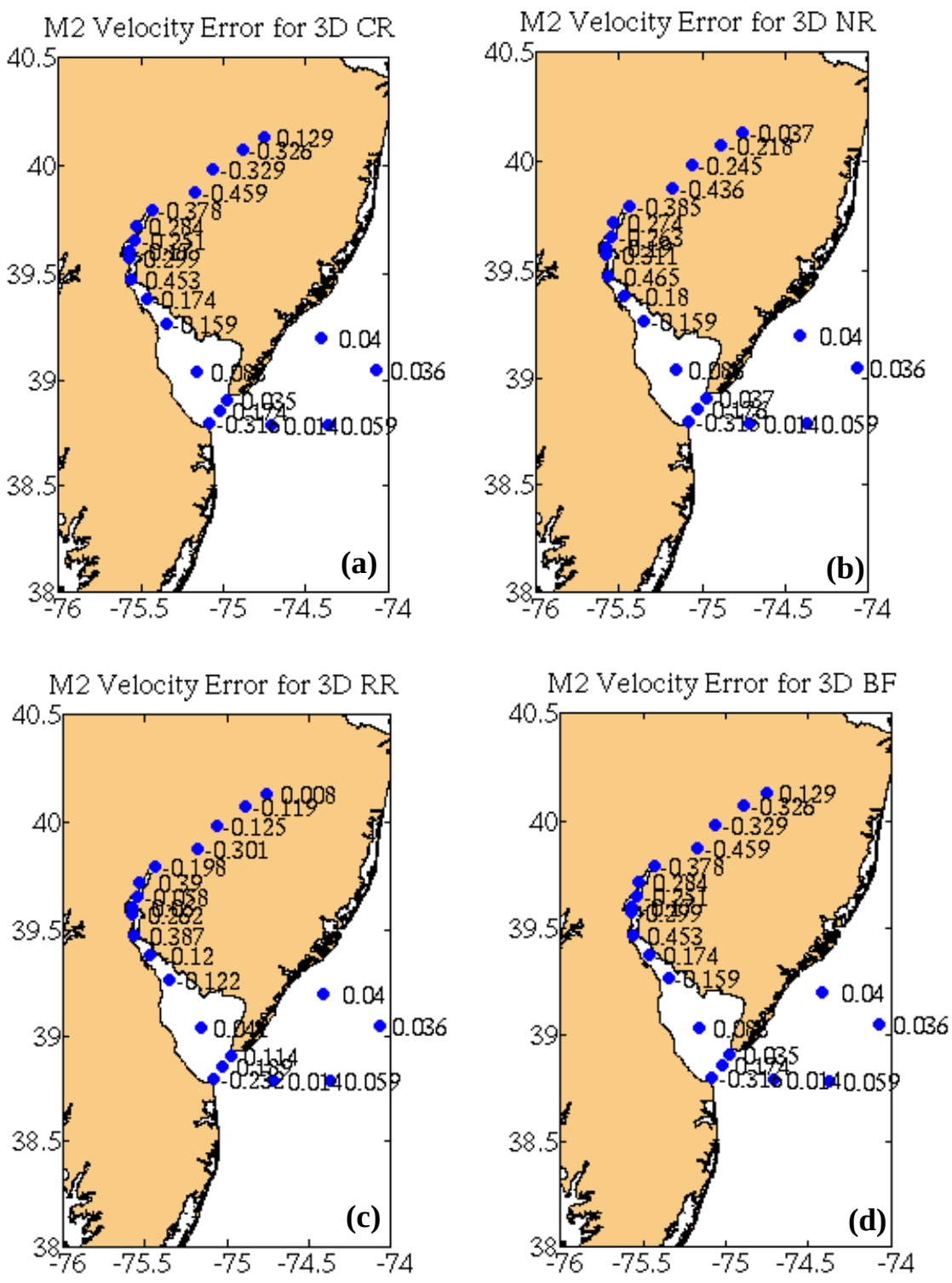

Figure 5.14: The M_2 velocity MBE for each of the 3D experiments (a) 3DCR, (b) 3DNR, (c) 3DRR, and (d) 3DBF.

f. Water Level Time Series Comparisons

Of all the 17 NOAA water level stations, only seven are primary stations with long-term continuous records. There are two located on the coast, two within Delaware Bay and three near the Delaware River. These seven NOAA stations with complete water level data records are used for model-data time series comparisons. Twenty five days of simulated water levels for each of the four test cases (2DCR, 2DNR, 2DRR, and 2DBF) are compared with the observation data. Mean model and observed water levels are computed and mean algebraic errors are reported in Table 5.4. In general, ADCIRC generated water levels are in good agreement with measured data, for both amplitude and phase. The largest errors occur at two river inlet locations. The form of the river forcing (2DCR, 2DNR, or 2DRR) does not make a significant difference in the water level time series, although minor fluctuations are evident nearest the river discharge location. The 2D and 3D modeled water levels simulations produced similar results. The most notable influence came from the applied meteorological forcing. Strong wind events (12*m/s*) showed a -25 to +25 cm variation when compared to model computations without surface wind. The magnitude of the deviation depends on the wind speed and direction.

Table 5.4. Mean algebraic error (MAE) for water level at 7 NOAA stations for all test cases.

Station	**2DCR (MAE)**	**2DRR (MAE)**	**2DNR (MAE)**	**2DBF (MAE)**
8534720	0.0835	0.0834	0.0834	0.0834
8558690	0.0379	0.0386	0.0385	0.0390
8536110	0.0245	0.0239	0.0237	0.0358
8557380	0.0273	0.0296	0.0294	0.0311
8551910	0.1074	0.1423	0.1369	0.1313
8545240	0.1607	0.2131	0.1854	0.2146
8539993	0.2346	0.1831	0.1129	0.9859

The model-data time series are plotted for the 2DCR baseline at all 7 NOAA stations in figure 5.15 for coastal and bay stations and figure 5.16 for river stations. At coastal station 8534720 (figure 5.15a), the model represents well the observed water levels after a ramping period of 5 days. In this location, model predictions and observational data are in good agreement with an MAE value of just above 8*cm*. No notable phase lag or lead is evident as the modeled water levels track the observed peaks and troughs. Errors appear larger at the other coastal station (8558690) shown in figure 5.15b thought he MAE has a smaller value of 0.0379*m*. The model overestimates water levels much of the time series with observed water levels having a smaller tidal range. Model computations at two bay stations (8536110 and 8557380), shown in figure 5.15c and 5.15d, have the lowest MAE just above 2*cm*. At these stations the model underestimates high tide during the first eight days, then overestimates the low tide elevation for the next few days. For the final 5 days the model continues to underestimate the low tide but grossly overestimates the high tide during the same period. Tides at the three river stations had stronger tidal signals when compared to water level time series at the other four stations; MAE values range from 10*cm* to 23*cm*. Station 8551910 showed reasonable agreement between model and measured data (figure 5.16a) and follows as error pattern similar to bay station 8536110 (figure 5.15c). In contrast, at stations 8539993 and 8545530, the model computed water levels overestimate high tide and underestimate low

tide (figures 5.16b and 5.16c).

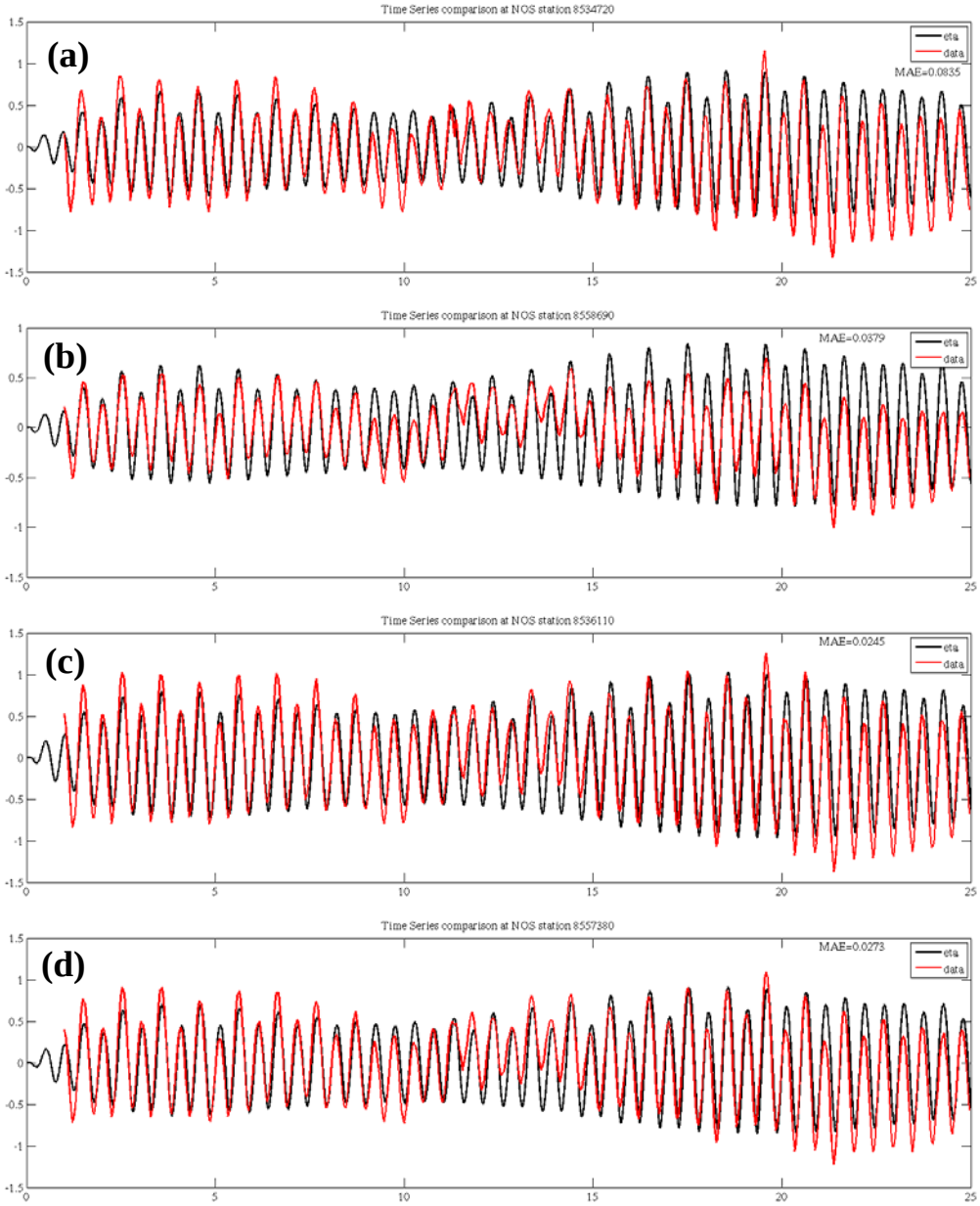

Figure 5.15: Water level times series of model (black) versus observations (red) for the 2DCR experiment at 4 NOAA stations, on the coast (a) 8534720, (b) 8558690, and in the bay (c) 8536110, and (d) 8557380.

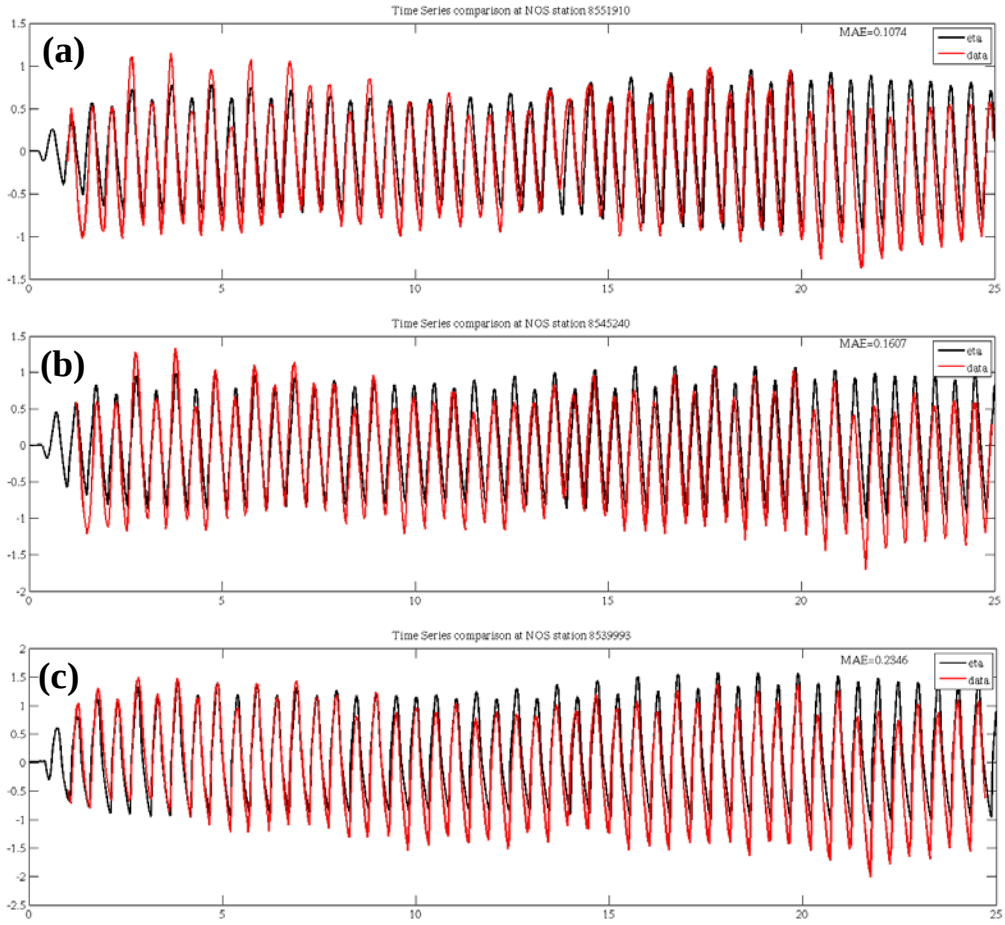

Figure 5.16: Water level times series of model (black) versus observations (red) for the 2DCR experiment at 3 NOAA stations near the river (a) 8551910, (b) 8545240, and (c) 8539993.

Comparisons between the 40-day time series for all four experiments (2DCR, 2DNR, 2DRR, and 2DBF) show negligible differences for the various river discharge options. The water levels are almost identical at open water stations where river flux is negligible. Even at a location near the Delaware River mouth, the difference between no river discharge and realistic river inflow is only few centimeters (figure 5.18e). As noted in prior discussions, modeled elevations are extremely sensitive to the bottom friction coefficient. The increased bottom friction coefficient in the estuarine region damps the tidal signal to a range of 0.5*m* (figure 5.17e), a significant reduction in the 2.5*m* range of water level fluctuation for the baseline, 2DCR test case.

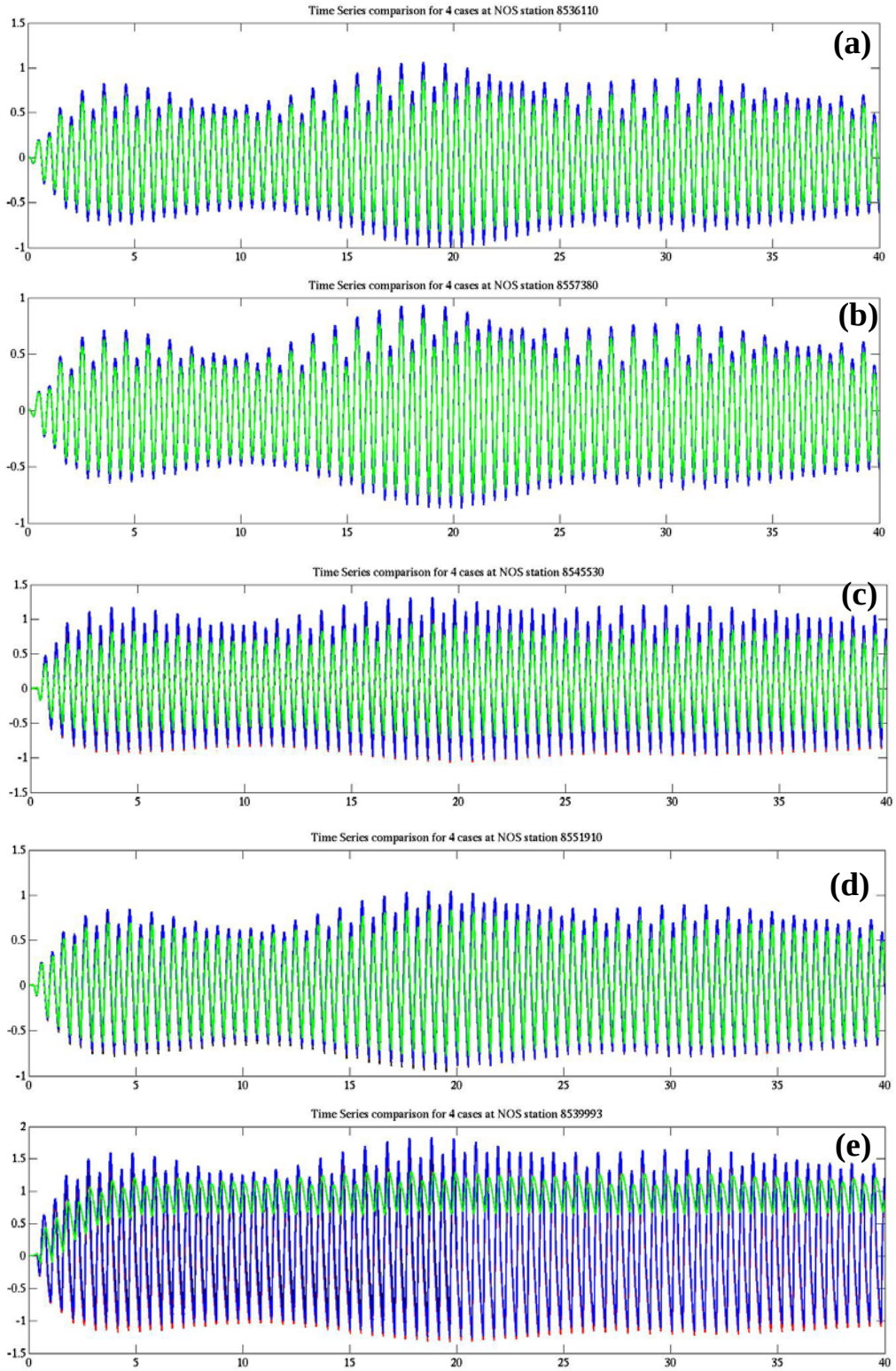

Figure 5.17 Modeled water level times series for the 2DCR (black), 2DNR (red), 2DRR (blue), and 2DBF (green) experiments at five NOAA stations near the river (a) 8536110, (b) 8557380, (c) 8545530, (d) 8551910, and (e) 8539993.

To determine the influence of meteorological forcing, strong wind events based on two predominant wind direction patterns are selected for simulation. Southeast and northwest winds at 12*m/s* are applied to a 30 day model simulation. The modeled elevations are not compared to field data since winds are idealized. Time series of the computed elevations are plotted against the no wind condition (case 2DCR) to demonstrate the effect of winds. As we might expect, the water levels generated without wind stress should fall in magnitude between water levels subject to winds in the opposite directions. Under the SW winds, a strong water elevation setup occurs at two river stations (8539993 and 8545530) while water levels at the coastal stations do not exhibit much response to the wind events. Time series for the SE wind, the NW wind and no wind are shown in figure 5.18. The applied winds lead to a 50*cm* range in the amplitude variation as compared to a scenario without wind. The magnitude of this deviation depends on the wind speed and direction.

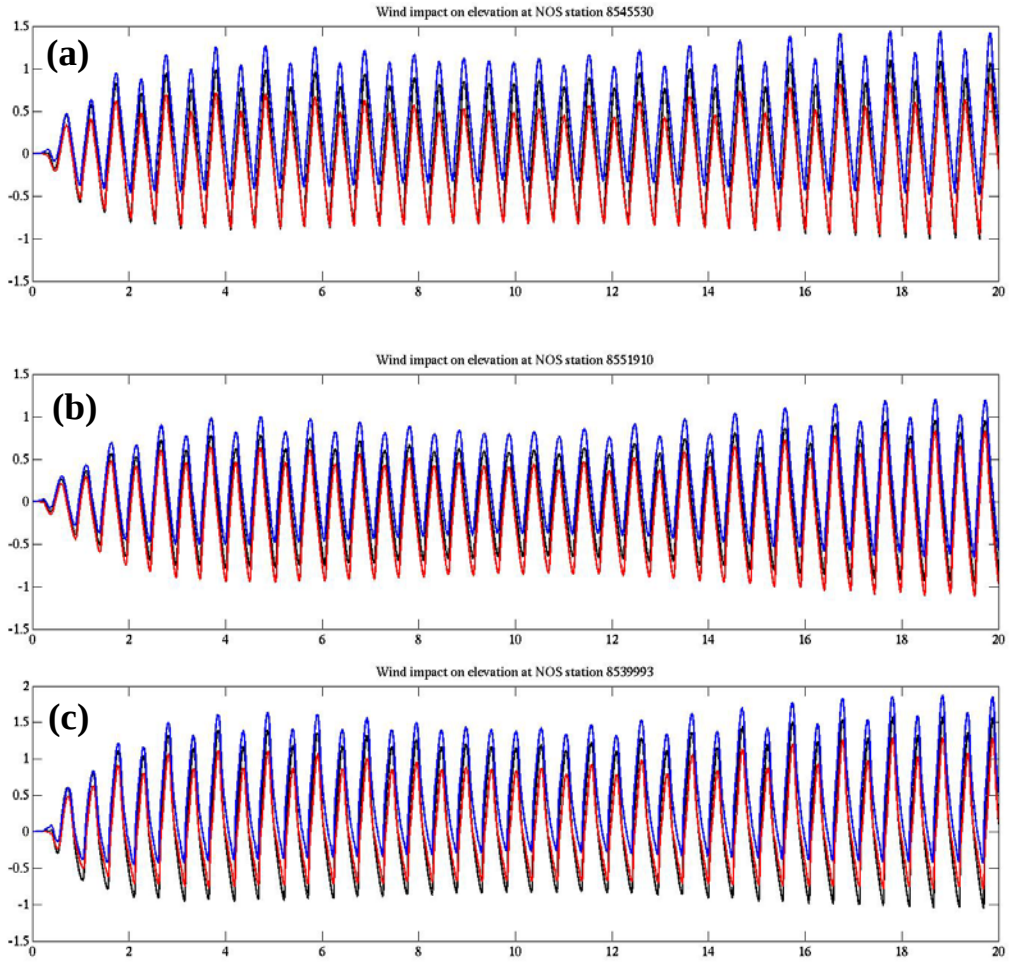

Figure 5.18 Modeled water levels at station (a) 8545530, (b) 8551910, and (c) 8539993 for an applied SW wind (blue), NW wind (red), or no wind (black) for the 2DCR test case.

g. Velocity Time Series Comparisons

The evaluation of modeled currents involves comparisons to current meter observations at 8 locations. Three stations are located at the bay entrance (001, 003 and 005), two are inside the bay (023 and 033) and three stations are in the Delaware River (052, 053 and 054). A twenty-day time series of velocity magnitudes are used to compute average velocity values at each location as well as a MAE. Tabulated results are recorded in table 5.5 for all four test cases, 2DCR, 2DNR, 2DRR, and 2DBF. Time series of the current magnitude compared during periods where current observations are available, e.g. for stations 001, 003, 005, 023, 033, Julian Days 95 to 115 are compared and for stations 052, 053 and 054, Julian Days 67 to 87 are considered.

The average velocity for all eight current meters ranges from 0.42 to 0.67 *m/s* except at station 054 in the upper Delaware river where currents are quite small at 0.15*m/s*. Even under the constant river discharge (2DCR), the modeled currents agree fairly well with the observations having an error of less than 5*cm/s* at 5 of 8 locations. The largest discrepancies occur at station 001, 033 and 053. For realistic river discharge (2DRR), the model computed currents improve compared to the observations and errors are reduced at all stations, not just the upstream river stations. It should also be noted that errors indicate that the model underestimates current velocity at 6 of the 8 locations. Not surprisingly, modeled currents under no river discharge as compared to the realistic discharge test case yielded comparable results except at the two upstream locations where the 2DNR case had larger errors. Just as with water levels, the velocity signals are damped by the increased bottom friction in the bay and river regions resulting in significant reductions in the velocity magnitude and large errors at all stations. Time series of the velocity magnitude for the 2DCR and 2DRR test cases at three stations are shown in figures 5.19 through 5.21.

Table 5.5. Average velocities for modeled and observed currents and mean algebraic error (MAE) at 8 NOAA current meter sites for all test cases (2DCR, 2DNR, 2DRR, and 2DBF).

Stn	Vavg (m/s)	2DCR	2DCR (MAE)	2DRR	2DRR (MAE)	2DNR	2DNR (MAE)	2DBF	2DBF (MAE)
054	0.1573	0.1380	-0.0193	0.1514	-0.0060	0.1228	-0.0285	0.1108	-0.0465
053	0.4245	0.3151	-0.1093	0.3155	-0.1089	0.2972	-0.1273	0.1399	-0.2846
052	0.4528	0.4024	-0.0505	0.4631	0.0103	0.4574	0.0046	0.1697	-0.2832
033	0.6684	0.4168	-0.2515	0.4330	-0.2354	0.4289	-0.2395	0.3431	-0.3253
023	0.4358	0.3901	-0.0457	0.4048	-0.0310	0.4048	-0.0309	0.3234	-0.1123
005	0.5378	0.5052	-0.0326	0.5409	0.0032	0.5413	0.0035	0.3928	-0.1450
003	0.4909	0.4550	-0.0359	0.4836	-0.0073	0.4837	-0.0072	0.3593	-0.1316
001	0.6184	0.4064	-0.2119	0.4644	-0.1539	0.4647	-0.1537	0.3356	-0.2828

Average 3D velocity values and MAE errors for the three river influx test cases (3DCR, 3DNR, and 3DRR) are computed. The statistical values at 8 NOAA stations are recorded in Table 5.6. When compared with the 2D velocity computations, velocities at station 033 located in the narrow section of the upper bay shows the greatest improvement with a reduction in error to -0.14*m/s* from -0.25*m/s*. This result concurs with the previous M_2 velocity solution in which the 3D model exhibits the most significant improvements in the estuarine region where complex stratification and mixing due to tides and river flux are present. The 3D velocities for which a realistic river discharge is applied (3DRR) has

reduced errors in 5 of 8 locations when compared to velocitie from the constant river flux test case, 3DCR. Time series of the velocity magnitude for the 3DCR and 3DRR test cases at three stations are shown in figures 5.19 through 5.21.

Table 5.6. Average 3D velocities for modeled and observed currents and mean algebraic error (MAE) at 8 NOAA current meter sites for all 3D test cases (3DCR, 3DNR, and 3DRR).

Stn	**Vavg (m/s)**	**3DCR**	**3DCR (MAE)**	**3DRR**	**3DRR (MAE)**	**3DNR**	**3DNR (MAE)**
054	0.1573	0.2216	0.0642	0.1374	-0.0199	0.0914	-0.0660
053	0.4245	0.2858	-0.1387	0.2777	-0.1467	0.2054	-0.2191
052	0.4528	0.3149	-0.1380	0.4722	0.0194	0.3593	-0.0936
033	0.6684	0.5271	-0.1412	0.5545	-0.1139	0.5275	-0.1408
023	0.4358	0.4906	0.0549	0.4885	0.0527	0.4925	0.0567
005	0.5378	0.5449	0.0071	0.6006	0.0628	0.5462	0.0084
003	0.4909	0.5283	0.0374	0.5410	0.0501	0.5297	0.0388
001	0.6184	0.4111	-0.2072	0.4672	-0.1511	0.4120	0.2063

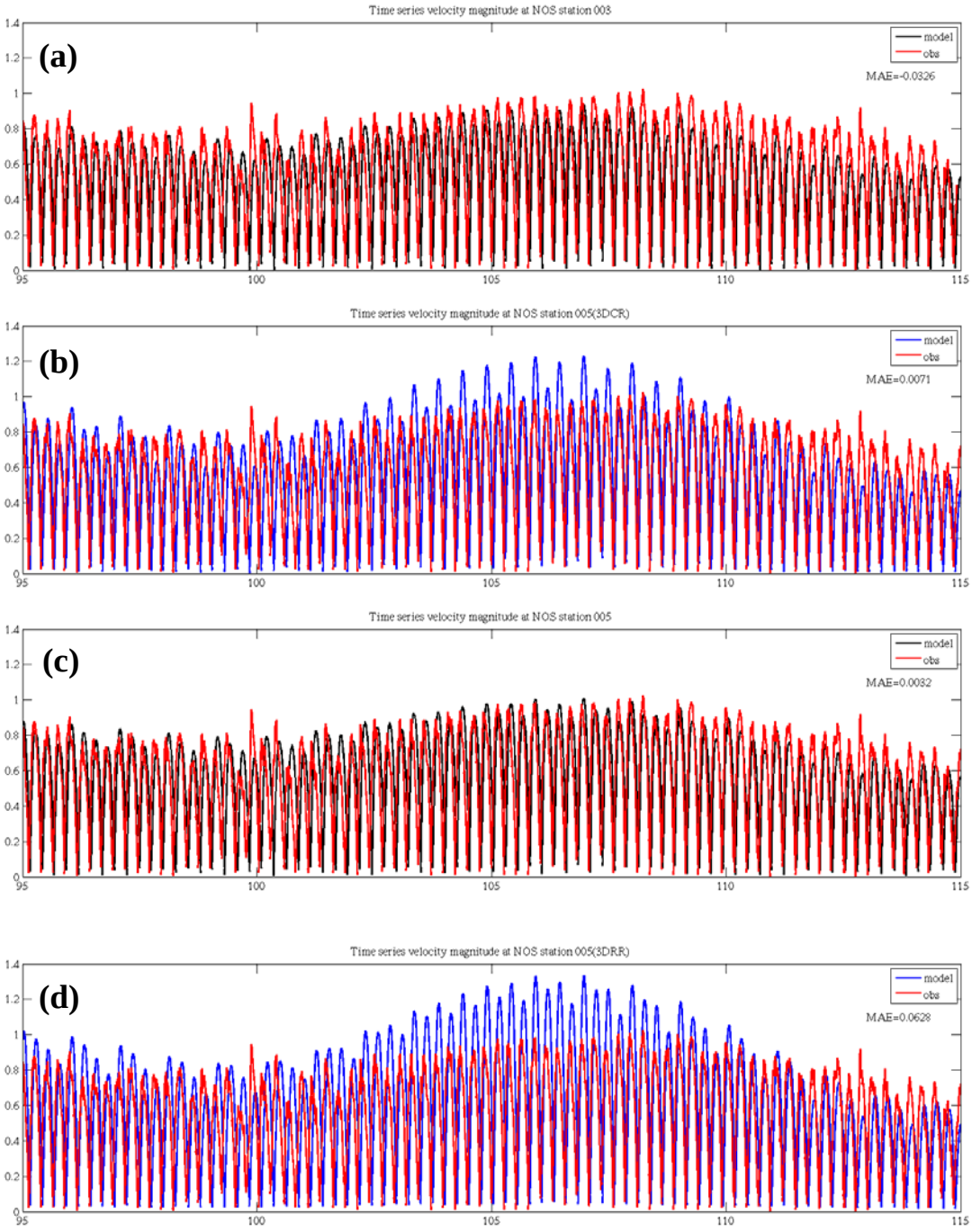

Figure 5.19: Computed (black/blue) and observed (red) current magnitudes at station 005 for the (a) 2DCR, (b) 3DCR, (c) 2DRR and (d) 3DRR experiments.

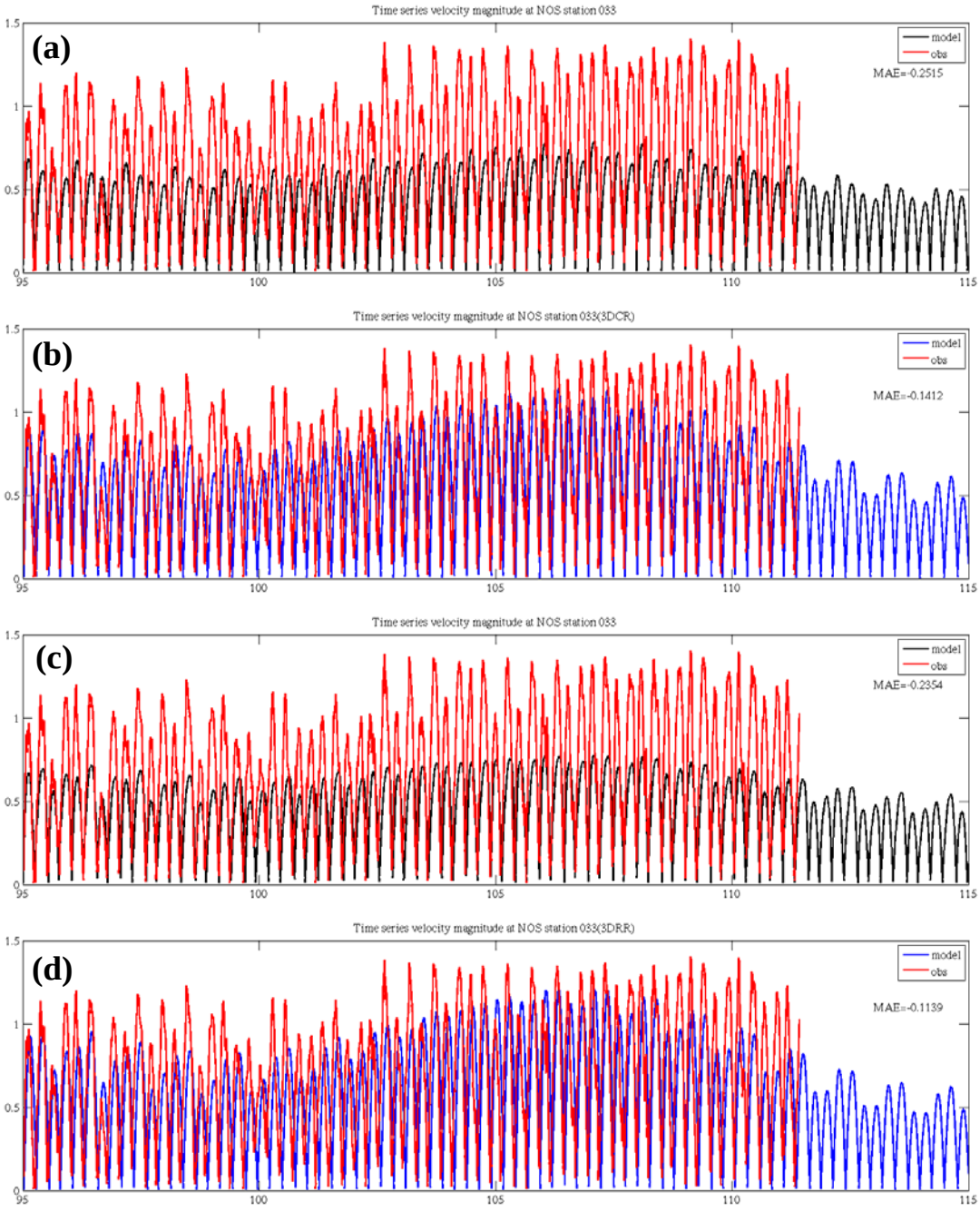

Figure 5.20: Computed (black/blue) and observed (red) current magnitudes at station 033 for the (a) 2DCR, (b) 3DCR, (c) 2DRR and (d) 3DRR experiments.

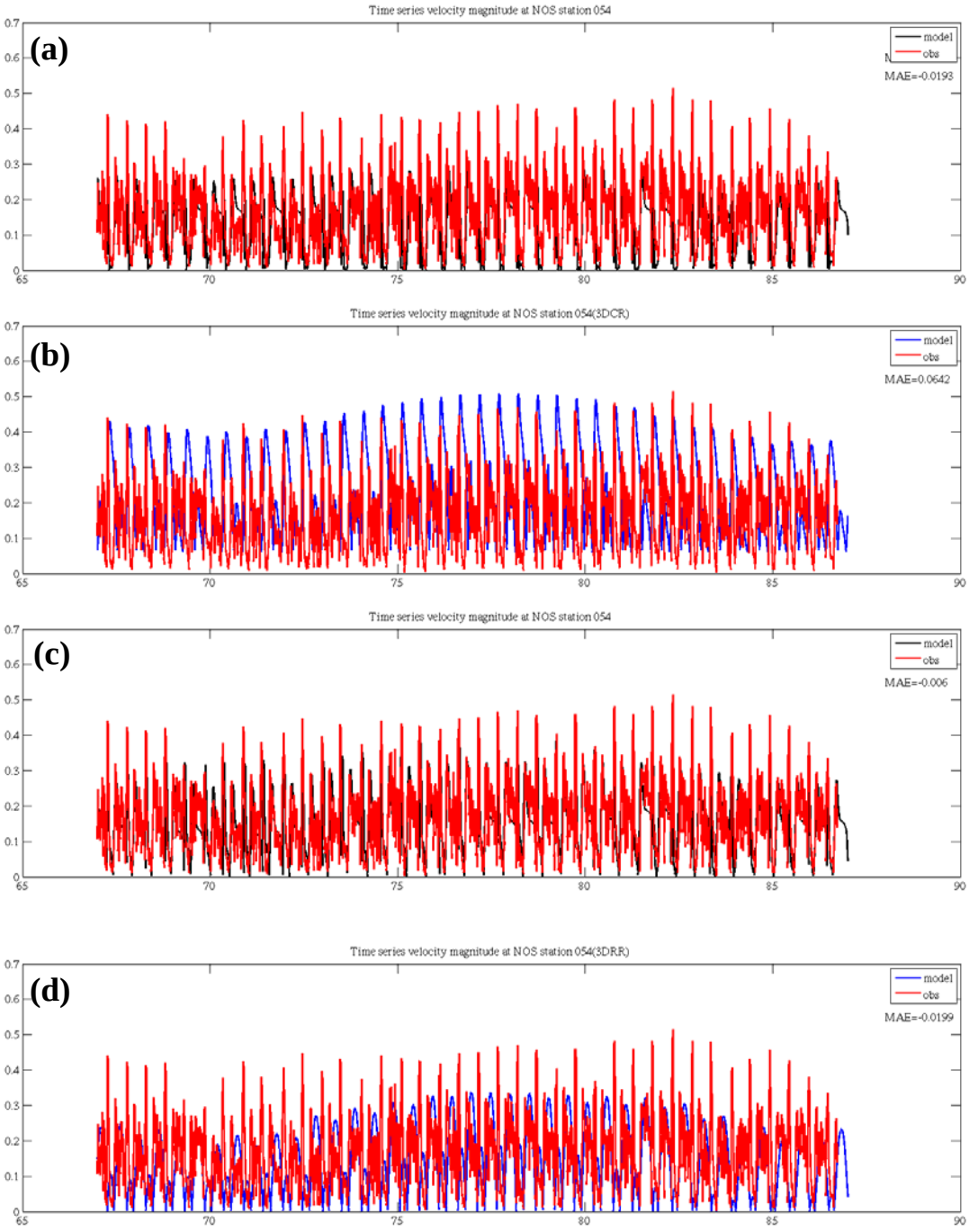

Figure 5.21: Computed (black/blue) and observed (red) current magnitudes at station 054 for the (a) 2DCR, (b) 3DCR, (c) 2DRR and (d) 3DRR experiments.

h. Summary

From the skill assessment of the 2D and 3D model experiments performed in this section, the findings are summarized as follows:

1) Water Level and Current Skill: Given properly specified boundary conditions, the ADCIRC model is able to simulate water level and currents reasonably well in a tidally driven estuary. The 2D modeled water level amplitudes have excellent agreement and indicate little sensitivity to the specified river discharge condition. The 3D modeled elevations also have a high agreement index with the exception of the nonlinear quarter diurnal constituents, M_4 and MN_4. Both 2D and 3D solutions have excellent phase propagation characteristics.

2) Impact of River Discharge: The modeled solutions are quite similar whether a constant discharge or no river discharge is specified. A time-varying realistic river discharge leads to better model water level predictions, particularly in the estuarine region of the bay. Velocity computations are all within 5% error of one another regardless of the river discharge specification.

3) Influence of Wind Stress: The application of wind stress strongly impacts the modeled water level and currents. A typical strong wind event of $12 m/s$ produces a $-25 cm$ to $25 cm$ variation when compared with a no wind, tidal-driven solution. The magnitude of the deviation depends on the wind speed and direction.

4) Sensitivity of Bottom Friction Coefficient: Despite a recommendation in the literature to increase the bottom friction coefficient along the axis of the bay from offshore through the estuarine waters to the head of the river, a significant reduction in the magnitudes of the elevation and currents led to poor comparison with observations. Note that the form of the turbulence closure in the 3D model was not modified from the constant eddy viscosity model. Changes in the form of the vertical mixing could significantly alter the outcome. The interplay between bottom friction and vertical mixing was not explored. The model sensitivity to the specified bottom stress for the model configurations considered here is quite acute.

5) 2D vs.3D Solutions: While the 2D model adequately simulates water level and velocity in the open waters outside the bay and in the river dominated region, the 3D model is required to properly simulate the complex stratification/mixing processes due to tidal-river flux interactions. As such the 3D model computed water level and currents simulation for the case of realistic river discharge out performed the 2D computations. In the cases of no river or a constant river discharge, the 3D model solution did not provide any additional accuracy. The simplistic constant eddy viscosity model used for vertical mixing could have reduced the impact of the 3D computations. Alternate closure formulations while available in ADCIRC were not explored. No spatial bias in the error patterns is discerned. The largest errors (identified with three separate stations) are likely due to under–resolution or misrepresentation of small-scale geometric features in the computational mesh associated with those individual stations.

6. Validation Test Results – Rattray Island Tidal Currents

Tidal flow around Rattray Island (30°00',S, 148°38'E) in the Great Barrier Reef, Australia (figure 6.1a) is an ideal test case for the following reasons: 1) an extensive field survey has obtained in-situ measurements of velocity and elevation (Wolanski et al., 1984), 2) the island lies in well-mixed water so a barotropic model is appropriate and yet, 3) the flow is strongly three-dimensional. Rattray Island is 1500*m* long and 300*m* wide and lies in water approximately 25*m* depth. Rattray Island lies perpendicular to tidal currents and stable eddies develop in the wake of rising and falling tides. The circulation dynamics at Rattray Island feature flow separation and recirculation with the formation of eddies. Turbid water in the wake of Rattray Island suggest sediment-laden water is carried upwards to the surface by vertical transport during the life span of the eddies (Figure 6.1ba).

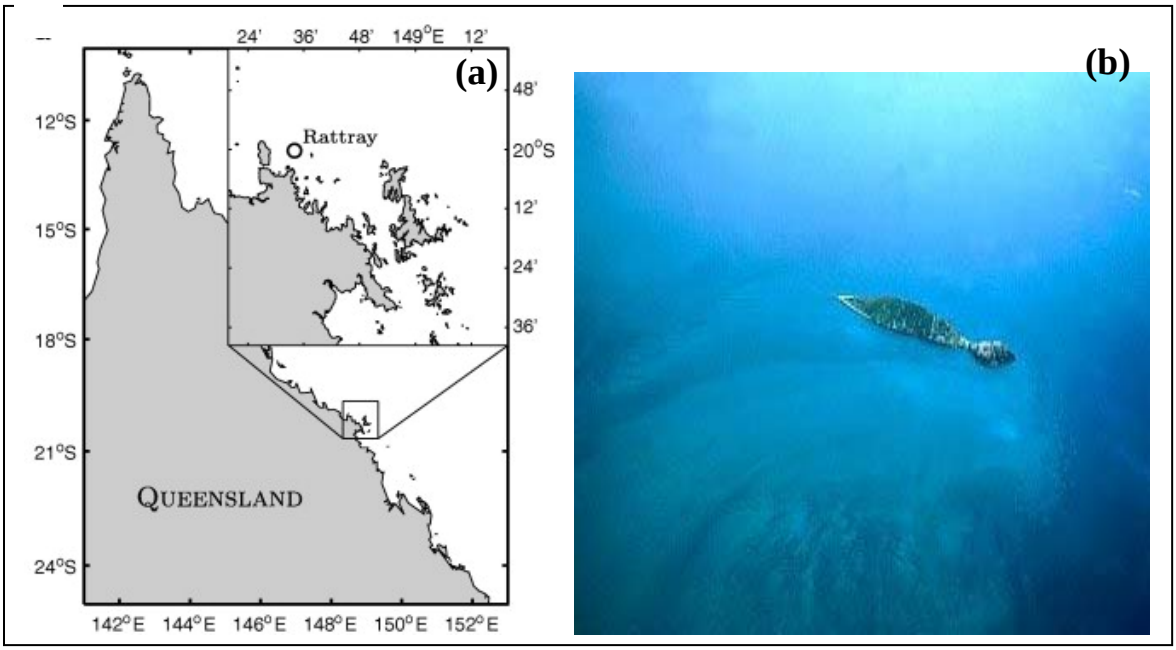

Figure 6.1 (a) Map locating Rattray Island in the Great Barrier Reef, AU (from White et al., 2008) and b) an aerial photo of Rattray Island taken from the east at rising tide (from Blaise and White, 2006).

Twenty-four Aanderaa current meters were deployed along 4 transects in the wake of Rattray Island. Velocities were recorded over the water column every 10 minutes in the wake of Rattray Island (circles in figure 6.2) during a rising tide in December of 1982. Data from current meter 15 is missing and two of the current meters, 25 and 26, recorded continuous 1-min averaged current data for two half-days only. The remaining current meters cover a period of 14 days. Sea level measurements from three tide gauges set in 10*m* of water around the island were recorded for eight days starting Nov 23, 1982 (squares in figure 6.2).

From Wolanski et al. (1984), a 3.5*m* spring tide is experienced at Rattray Island and the rising tide flows to the southeast in figure 6.1a filling the bay. A large time lag, up to two hours, exists between slack water and current reversals. The sea level difference across

Rattray Island is phase locked with tidal currents and is up to 2.5*cm* in amplitude. Sea levels are higher on the upstream side than the downstream side.

Ambient currents follow the sea level fluctuations closely though lagging by approximately two hours. The ambient tidal current reverse direction at an angle of 180^{o}, making the ellipses rectilinear. The largest and smallest ranges of the tidal fluctuations are 3.1*m* and 1.2*m* corresponding to the maximum flood currents at meter 2 of 0.6*m/s* and 0.4*m/s*, respectively. These currents also indicate a weak anti-clockwise rotation of the current, leading to a residual circulation.

Currents are deflected around the island and show the generation of an eddy near the lee of the island that grows progressively in size. Typically, after 1 hour into the flood current cycle, the current direction close to and in the lee of the island (stations 24-26) starts to rotate clockwise until it reached a fixed direction, largely against the ambient current. Progressively (first at stations 5-7 and then stations 12-14) a similar effect is felt downstream. Thus a clockwise circulation is established in the lee of the island. The current structure in the eddy is stable with time. The width (parallel to the long axis of the island) of the eddy along the section of stations 1-8 is roughly equivalent to that of the island and independent of the amplitude of the ambient current. The eddy at most extends to the section of stations 14-21 yielding a maximum eddy length of twice the length of the island.

As for the three-dimensional structure of the currents, observations near station 24 indicate no marked velocity gradients over the water column. However, a clockwise rotation of up to 30^{o} prevailed from surface to bottom.

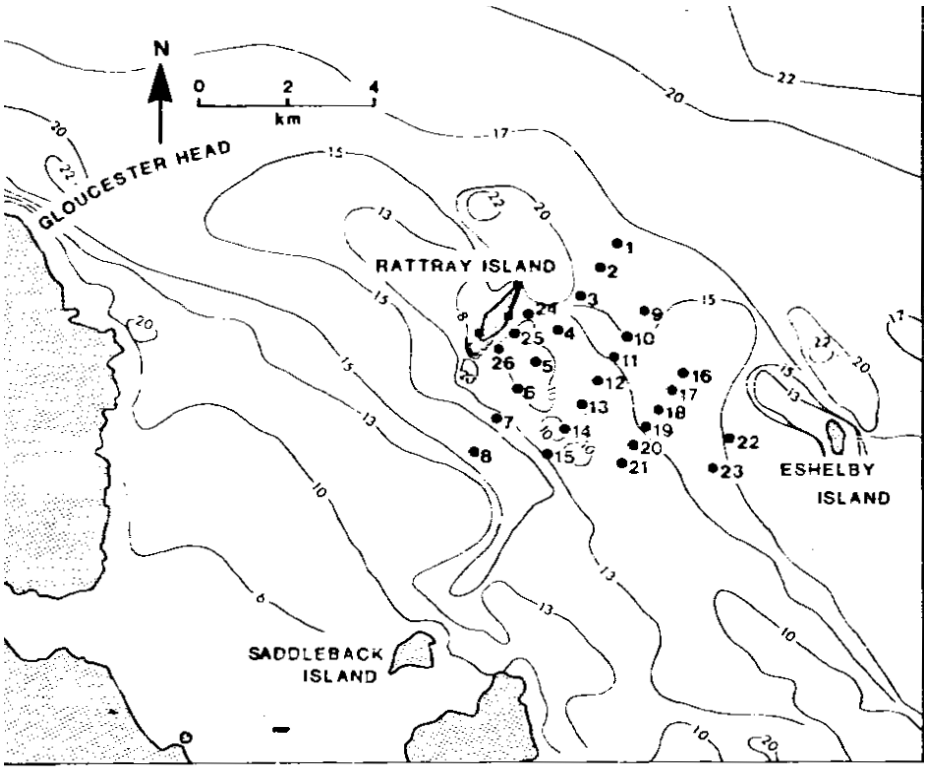

Figure 6.2: A map of tidal gauge and current meter locations deployed in December 1982 in the wake of Rattray Island (from Wolanski et al., 1984).

a. Model Configuration

As part of the Rattray Island benchmark test case, five resolutions of unstructured triangular meshes are provided and detailed in Table 6.1. The domain has been rotated from a northwest to southwest orientation to a north-south orientation so as to minimize the x-component of the far-field velocity which will be used as a boundary condition. The bathymetry data included as part of the benchmark has been interpolated to each mesh. Water depths are quite shallow ranging from $9m$ to $41m$ with an average depth of $25m$ (see figure 6.3).

TABLE 6.1 Specifications of the Rattray Island Benchmark finite element meshes.

Mesh Name	Mesh Parameters		Resolution	
	No. Nodes	No. Elements	Min	Max
01	1554	3024	140	921
02	2531	4973	116	944
03	3098	6096	88	944
04	3845	7555	62	721
05	7084	14024	33	770

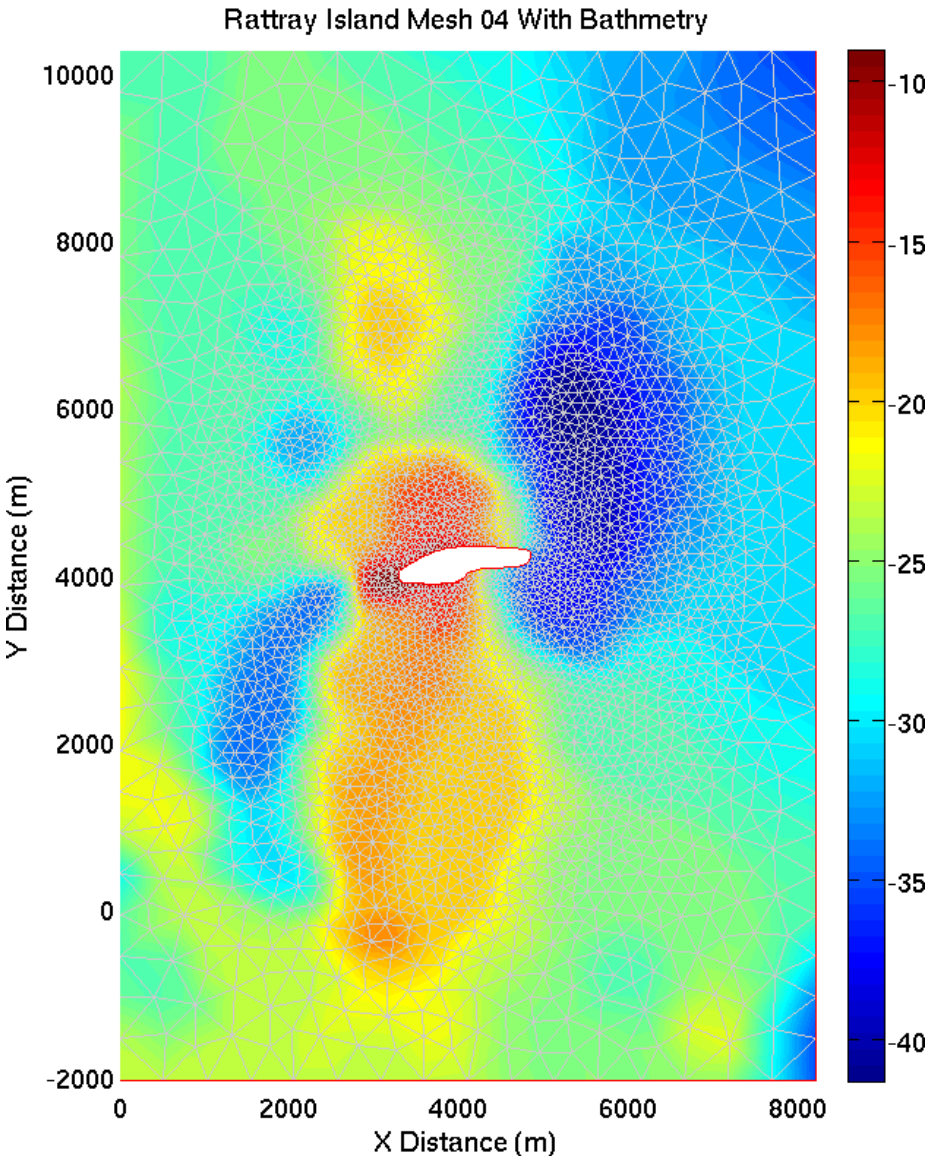

Figure 6.3: Bathymetry (in *m*) and the unstructured finite element mesh (04) domain for the Rattray Island benchmark.

The only applied forcing comes from tidal variations at the open boundaries (referred to as the lower and upper boundaries (along the lines $y = -2000\,m$ and $y = 12,300\,m$). Tidal potential forces are ignored for such a small domain and no surface wind stress is applied. Since tidal ellipses are strongly rectilinear in a direction perpendicular to the elongated sides of the island, closed conditions (IBTYPE = 1) are assigned along the lateral boundaries ($x = 0\,m$ and $y = 8000\,m$) following the recommendations of the benchmark. For the upper and lower open water boundaries, the benchmark suggests using the supplied tidal elevation measured close to the island in combination with the measured velocities from a far field current meter station (i.e. 23). The provided elevation and velocity data start at day 5.11804 and continue for about 8 days. Since the phase lag between the upper and lower boundaries is

less than 20 min (White et al. 2008), uniform conditions are applied at both open water boundaries.

A number of boundary conditions are applied and evaluated to maximize model fidelity as compared to the observed tidal elevations and current magnitudes. The results are discussed below. The first implementation of the open water boundary forcing involved the use of ADCIRC's non-periodic elevation boundary forcing, a fort.19 file, in which the provided hourly elevation time series was applied at the lower and upper boundary nodes. Elevations produced by this model reproduced surface elevation magnitudes fairly well, but produced unrealistically small currents (< 10*cm/s* maximum). For a second implementation of the model boundary forcing a tidal boundary flux was created from a combination of both the elevation and current U and V component time series data provided. Model computations using this flux forcing produced surface elevation time series in which elevation magnitudes exceeded the magnitude of the original tidal elevations (ranging from 0 to about 3 m) by a factor of 3 regardless of the other model input parameters such as vertical eddy viscosity coefficients. Subsequent experiments modified the tidal elevation time series used in the flux computation by subtracting the mean from the entire time series to produce a residual elevation data set. The resulting boundary flux forcing data set is hereafter referred to as the "residual" flux. The modeled surface elevations were reduced significantly without an accompanying reduction in current speed. A related boundary flux was computed using half of the values of the "residual" elevations along with provided current data, named "residual-by-2". The modeled elevations resulting from an application of this latest boundary flux forcing produced an even greater reduction in the range of surface elevations, but also reduced the maximum current speed. To all boundary flux forcing, a 12-day linear or hyperbolic tangent ramping function was applied, prior to application in the model. As a result, the model's internal hyperbolic ramp function was not applied. This latter ("residual-by-2") and most successful boundary flux forcing was assigned through the fort.20 file to the northern and southern boundaries using the boundary type, IBTYPE = 22.

Damping of the velocities when using a flux-specified boundary condition have been observed in other ADCIRC applications, particularly if the solution reflects off the open ocean boundary and energy is unable to radiate out of the domain. In later versions of ADCIRC, a flux-specified, radiative boundary condition is available to eliminate this issue (IBYTPE = 52). Sensitivity tests on the lateral boundary specification indicated that in changing from an impermeable (IBTYPE = 0) to a radiative boundary (IBTYPE = 30), the computed elevations experience a dramatic decrease in maximum elevation range, from 9.7*m* to 2.7*m*. Secondly, in comparing the model response to flux forcing specified through an essential (IBTYPE = 2) or a natural boundary condition (IBTYPE = 22), the essential boundary condition was found to be more restrictive leading to a greater potential for model instabilities. While highly advective flows can be strongly influenced by the selection of the GWCE weighting parameter, TAU0, more recent versions of the ADCIRC model allow for spatially varying TAU0 values to be computed internally in the model based on local velocity values. However, it was determined that the availability of this feature would not lead to significant alterations of the Rattray Island computed elevations and currents.

The ADCIRC model fort.15 input file parameter specifications for the 3D barotropic with flux forcing is configured using the Makef15 GUI. The default settings in the Makef15 GUI were changed in the following manner:

- Activate the non-fatal error override, NFOVER = 1
- The coordinate system is Cartesian, ICS = 1
- The model is run in 3D barotropic mode, IM = 1
- Wetting and drying is inactive but the nonlinear finite amplitude terms are on, NOLIFA = 1
- All advective terms are activates, NOLICA = 1 and NOLICAT = 1
- Specify a spatially constant Coriolis parameter, NCOR = 0
- No meteorological forcing is applied, NWS = 0
- No ramp function is used, NRAMP = 0 (ramping of the forcing is handled externally)
- A smaller GWCE weighting parameter is specified, TAU0 = 0.005
- The length of simulation is set to 20 days, RNDAY = 20.0
- The ramp period set to a duration of 0 days, DRAMP = 0.0
- The minimum depth, H0, is set to 3.0m, H0 = 3.0
- The central projection points are specified for the model domain, SLAM0,SFEA0 = -88.5, 29.0, respectively.
- Parameters for the nonlinear quadratic bottom friction coefficient are specified, CF = 0.05
- The lateral eddy viscosity coefficient is set to 5, ESL = 5.0
- A constant Coriolis factor is computed, CORI = 0.0000498665369
- Select station elevation output, NOUTE = 1 for just under 8 days (TOUTSE = 12.0, TOUFE = 20.0 model days) every 10 minutes (NSPOOLE = 300)
- Identify 26 elevation station locations, NSTAE = 26
- Select station velocity output, NOUTV = 1 for just under 8 days (TOUTSV = 12.0, TOUFV = 20.0 model days) every 10 minutes (NSPOOLV = 300)
- Identify 26 velocity station locations, NSTAV = 26
- Select global elevation output, NOUTGE = 1 for just under 8 days (TOUTSGE = 12.0, TOUFGE = 20.0 model days) every 10 minutes (NSPOOLGE = 300)
- Select global velocity output, NOUTGV = 1 for just under 8 days (TOUTSGV = 12.0, TOUFGV = 20.0 model days) every 10 minutes (NSPOOLGV = 300)
- Quadratic slip is selected, ISLIP = 2
- Surface and bottom roughness are specified, Z0S = 0.01, Z0B = 0.005
- A uniform vertical grid with 21 levels is specified, IGC = 1, NFEN = 21
- A vertical eddy viscosity code for a constant is selected, IEVC = 1, and the value is EVCON = 0.001 (the minimum EV value is not used for IEVC = 1)
- Select 3D station velocity output, I3DSV = 1 for just under 8 days (TO3DSVS = 12.0, TO3DSVF = 20.0 model days) every 10 minutes (NSPO3DSV = 300)
- Identify 26 velocity station locations, NSTA3DV = 26
- Select 3D global velocity output, I3DGV = 1 for 8 days (TO3DGVS = 11.9994, TO3DGVF = 20.0 model days) every hour (NSPO3DGV = 1800)

To summarize, a fully nonlinear 3D model simulation extends for 12 days during which the externally ramped forcing flux is applied to the lower and upper boundaries. The simulation then continues for an 8 day period that coincides with elevation and current meter observations. The horizontal mesh is the highly refined 04 mesh whose resolution ranges from 62m to 721m. The vertical grid is composed of 21 uniform vertical levels. The

turbulence closure is a simple constant vertical eddy viscosity mixing coefficient with a value of 0.001 and quadratic slip conditions apply at the sea bed. A time step of 2 seconds and a minimum depth of 3 meters is specified.

b. Predictor-Corrector Time Stepping Performance

The Rattray Island benchmark provided an opportunity to test the predictor-corrector (P-C) time stepping algorithm for a non-wetting and drying problem. Note applications with wetting and drying are limited by the propagation speed of the wetting front. The wetting front cannot advance more than a single element per time step. As a consequence, the predictor-corrector time stepping is not usually an appropriate choice under wetting and drying conditions.

The Rattray Island benchmark was run in a 2D mode for tests of the predictor-corrector time stepping. Recall from Section 1 that the predictor-corrector algorithm allows larger time steps to be taken by the model for a give application and is activated by setting a negative value for the time step. For Rattray Island, the non P-C application has a time step of 2.0 seconds. The model was run for successive multiples of the time step (i.e. 4*s*, 8*s*, 12*s*, 16*s*, 20*s*). The error analysis is conducted over 1152 time steps so that in total there are 281,088 data values included in the error analysis. The percent error for elevation is computed as the absolute value of the non P-C elevation minus the P-C computed elevation at 244 evenly distributed station locations (figure 6.4) throughout the mesh. No percent error is calculated for velocity values since the velocity components are so small. Results are recorded in Table 6.2. Note that model computations using P-C with time steps above 12s became unstable. The elevation differences in Table 6.2 between P-C and non-P-C are less than 10% for 90% of the 1152 time steps contained in the analyses at 244 stations. So for the Rattray Island benchmark, the P-C time stepping option allows an increase in time step by a factor of 6 without degradation of the computed solution.

TABLE 6.2: Errors associated with the predictor-corrector time stepping for the Rattray Island benchmark.

Percent Elevation Differences: (No P-C minus P-C)							
		% Elevation Error		V % Current Error U			
Increase	Delt	Min	Max	Min	Max	Min	Max
2x	4s	2.1e-07	19.2	0	0.0020	4.7e-09	0.01
4x	8s	8.3e-07	17.7	0	0.0023	1.6e-10	0.01
6x	12s	2.6e-07	20.7	0	0.0026	3.6e-10	0.01

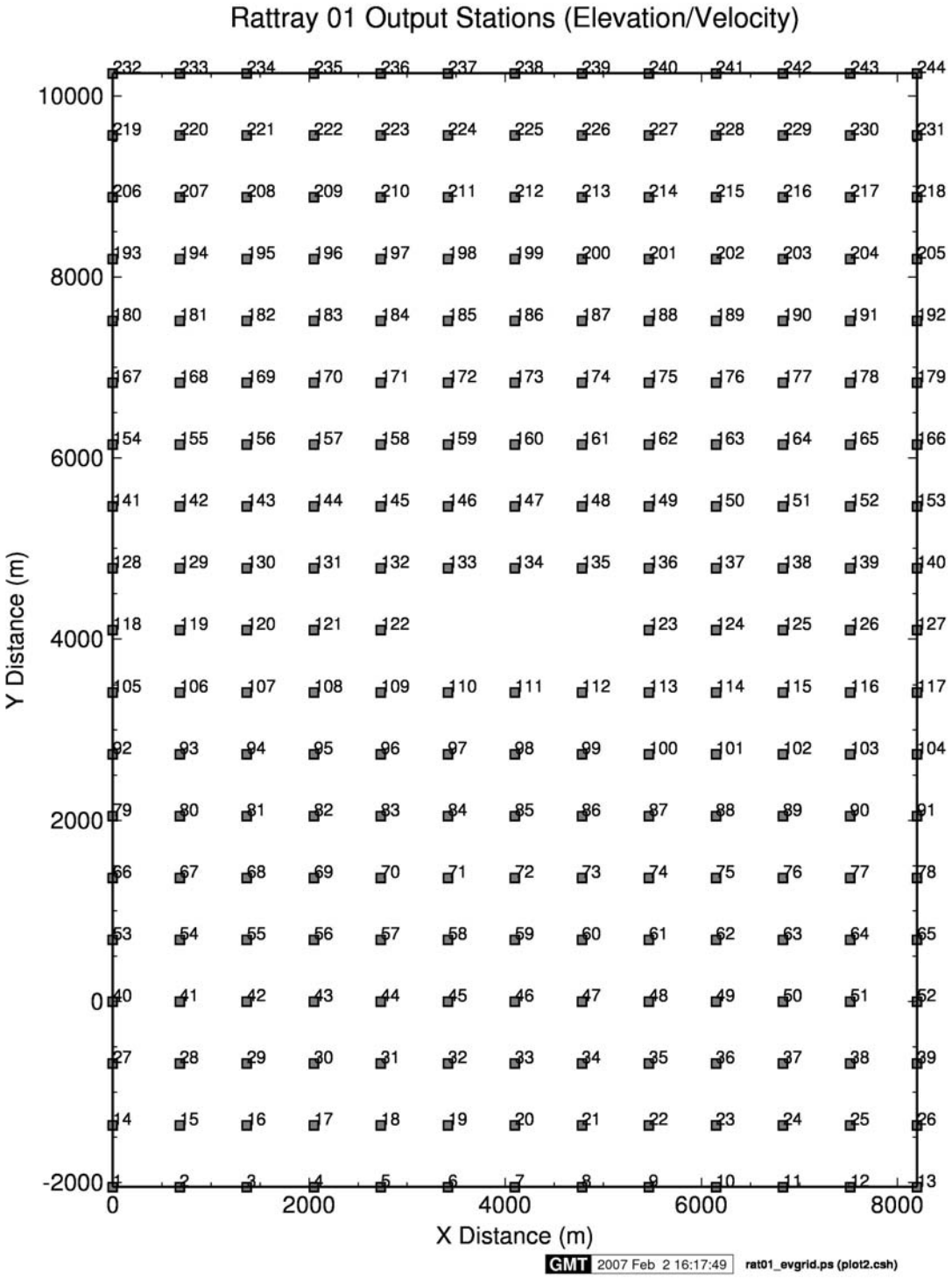

Figure 6.4: The regular grid of 244 stations at which modeled elevation and velocity solutions from P-C and non P-C time stepping are compared.

c. 3D Currents

The modeled flow pattern on 28 November 1982 is shown in figure 6.5 at 11*hrs*, 13.3*hrs*, 17.3*hrs*, and 19.5*hrs* into the simulation. At the rising tide (figure 6.5a) flow towards the north side of the island separates and flows around the tips gaining strength to approximately 0.2*m/s*. A stable eddy then forms in the southern lee of the island with clockwise rotation. A second eddy forms to the southwest the island rotating counter-clockwise. Asymmetry of the eddies is due to the bathymetric variation. The magnitude of the currents is similar to the free stream velocity and ranges from 0.2-0.1*m/s*. Just over two hours later (figure 6.5b) the eddy has grown in size to twice the width of the island. The long lag time reported by Wolanski et al (1984) is confirmed here and 4 hours later at 17.3*hrs* into the simulation the tide has reversed and eddy formation is underway in the wake of the island, now to north. A similar two eddy system of counter-rotating circulation is set-up. Current magnitudes are somewhat reduced for the falling tide over that of the rising tide. The modeled currents do not seem to reach the maximums of 0.6*m/s* and 0.4*m/s* as reported by Wolanski et al (1984).

Vertical profiles of the currents at all current meter locations are shown at the same times, 11*hrs*, 13.3*hrs*, 17.3*hrs*, and 19.5*hrs* in to the simulation on 28 November 1982 in figure 6.6. At station locations in and around eddy formation on the rising tide (figure 6.6a and figure 6.6b), stations 24, 25, and 26 and stations 4, 5, and 6, the slight velocity gradients disappear as the eddy grows in size. At stations in the far field away from the immediate eddy formation, e.g., stations 11, 12, 17, and 18, a boundary layer is present in the velocity profile. Currents on the non-wake side of the island are uniform over the water column (figure 6.6d).

Currents, both modeled and observed, located 5m below the surface are compared at the current meter stations on 28 November 1982 at 18.2*hrs* and 20.5*hrs* and on 29 November 1982 at 0.5*hrs*, and 2.6*hrs* in figure 6.7. The modeled currents agree well with observations in direction and magnitude at the rising tide (figure 6.7a) but the model begins the tide reversal earlier than that measured (figure 6.7b). Currents from the model on the non-wake side of the island are shifted in direction from the measured current particularly at locations away from the island (figure 6.7c). Once again we observe the model leading the phase on the tide reversal (figure 6.7d).

For completeness another tidal cycle of horizontal currents, corresponding vertical profiles and model-data comparisons at current meter locations are included in figure 6.8, figure 6.9 and figure 6.10, respectively, for 04 December 1982 at 3.6 *hrs*, 5.6 *hrs*, 7.6 *hrs*, 9.6 *hrs*, 11.6*hrs*, and 13.6*hrs.*

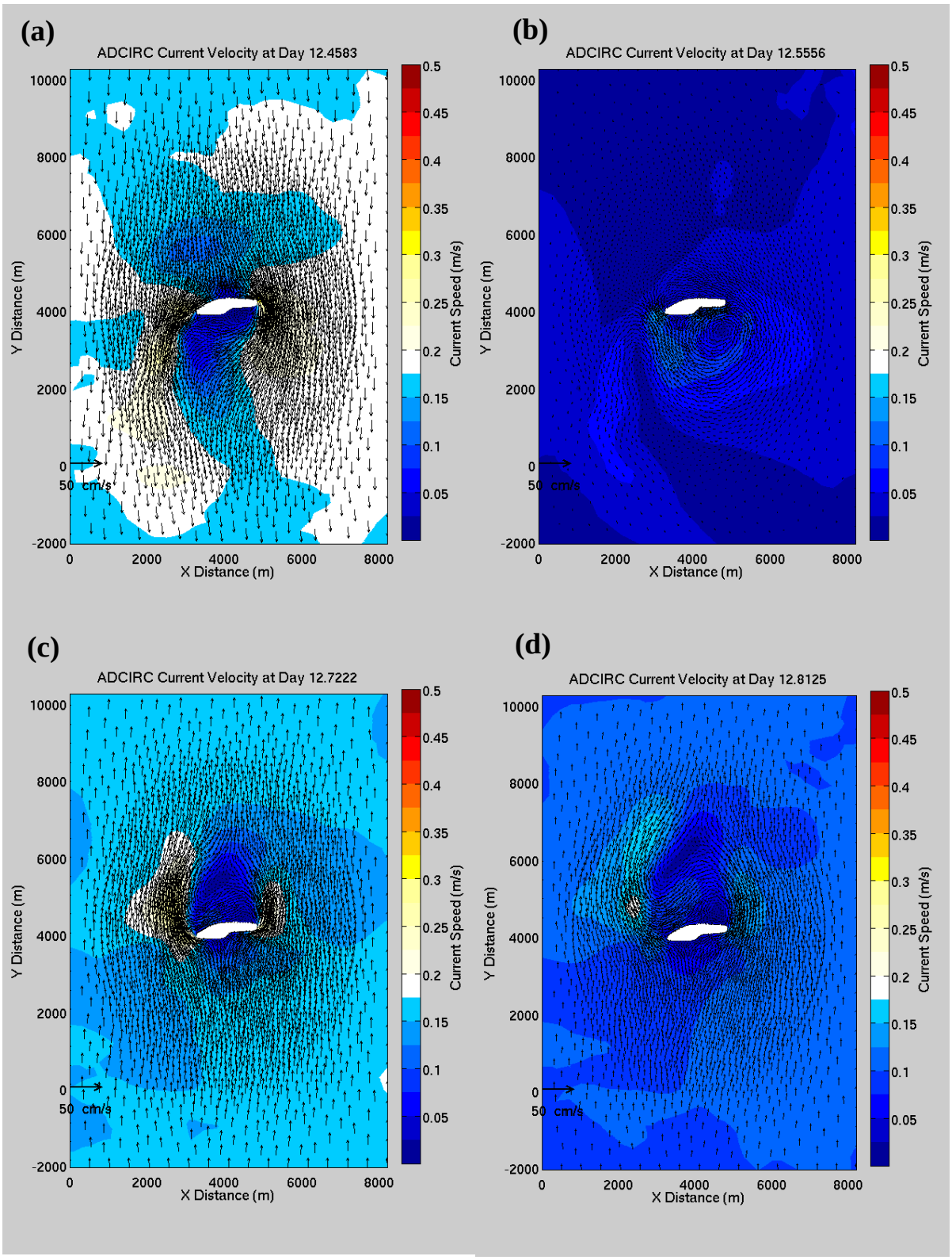

Figure 6.5: Computed currents on 28 December 1982 at (a) 11*hrs*, (b) 13.3*hrs*, (c) 17.3*hrs*, and (d) 19.5*hrs*.

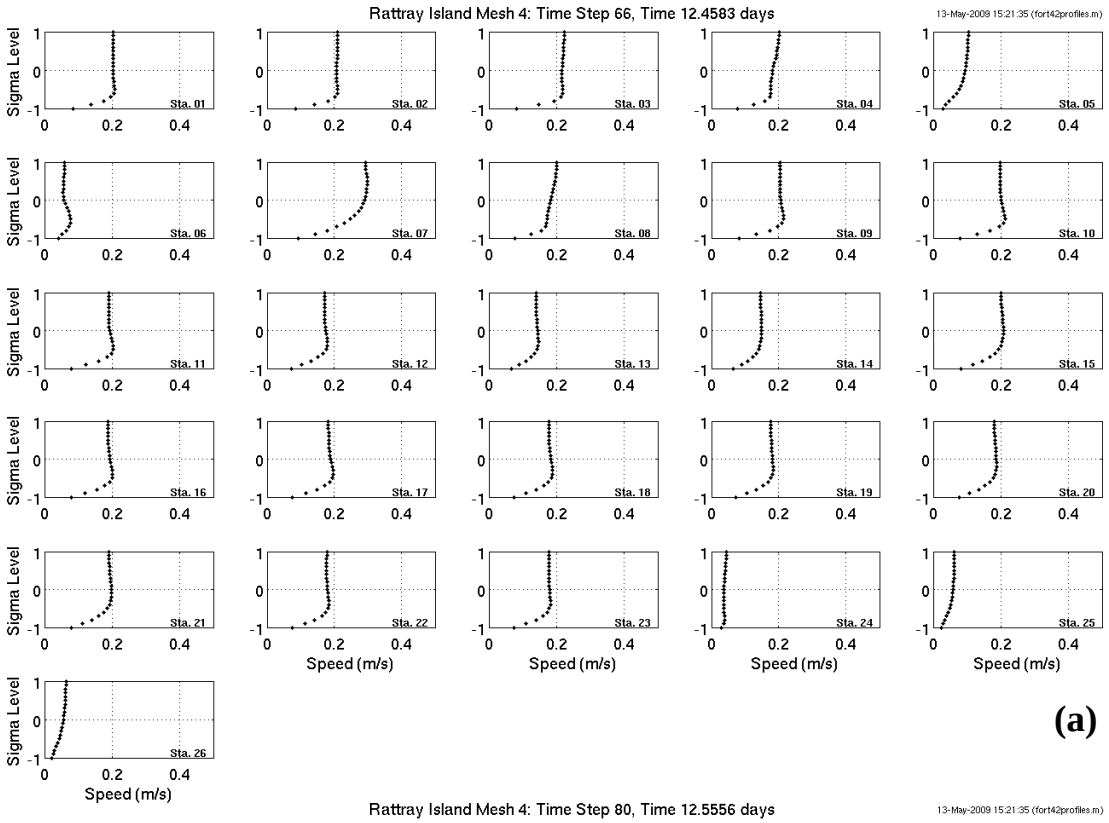

(a)

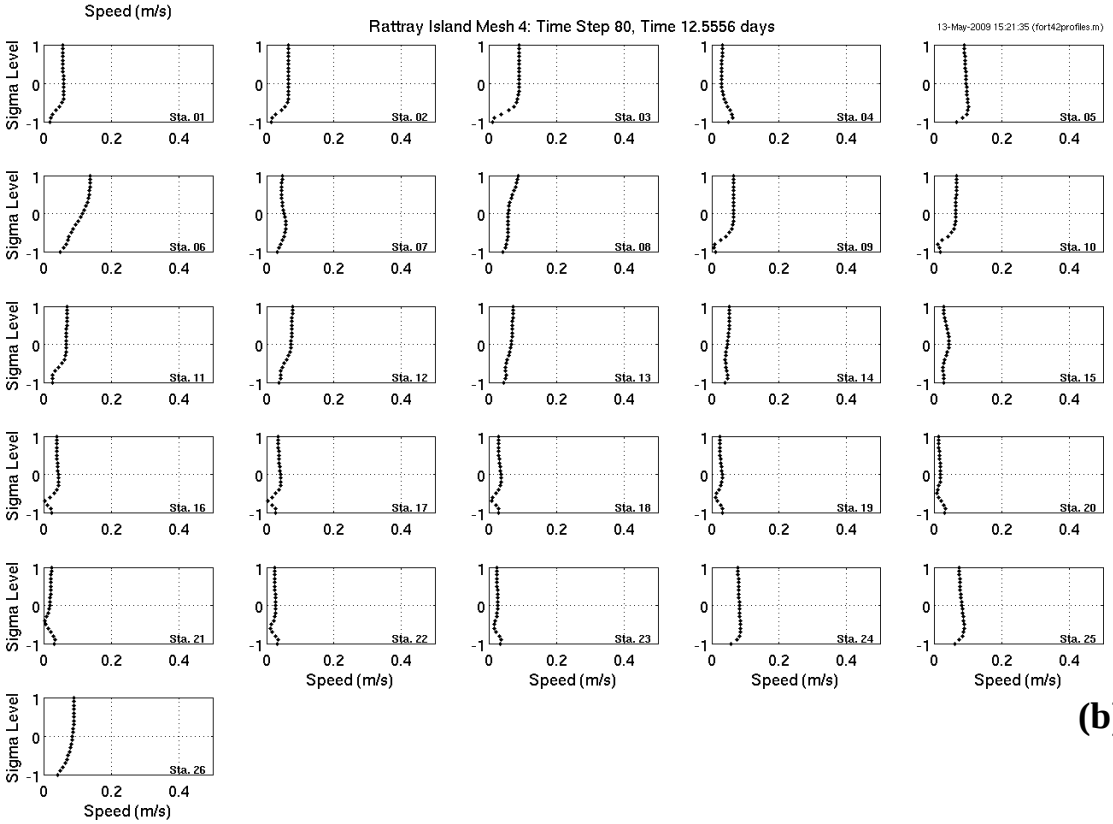

(b)

Figure 6.6 Vertical profiles of the modeled currents at each of the 26 current meter locations on 28 November 1982, (a) 11*hrs* and (b) 13.3*hrs*.

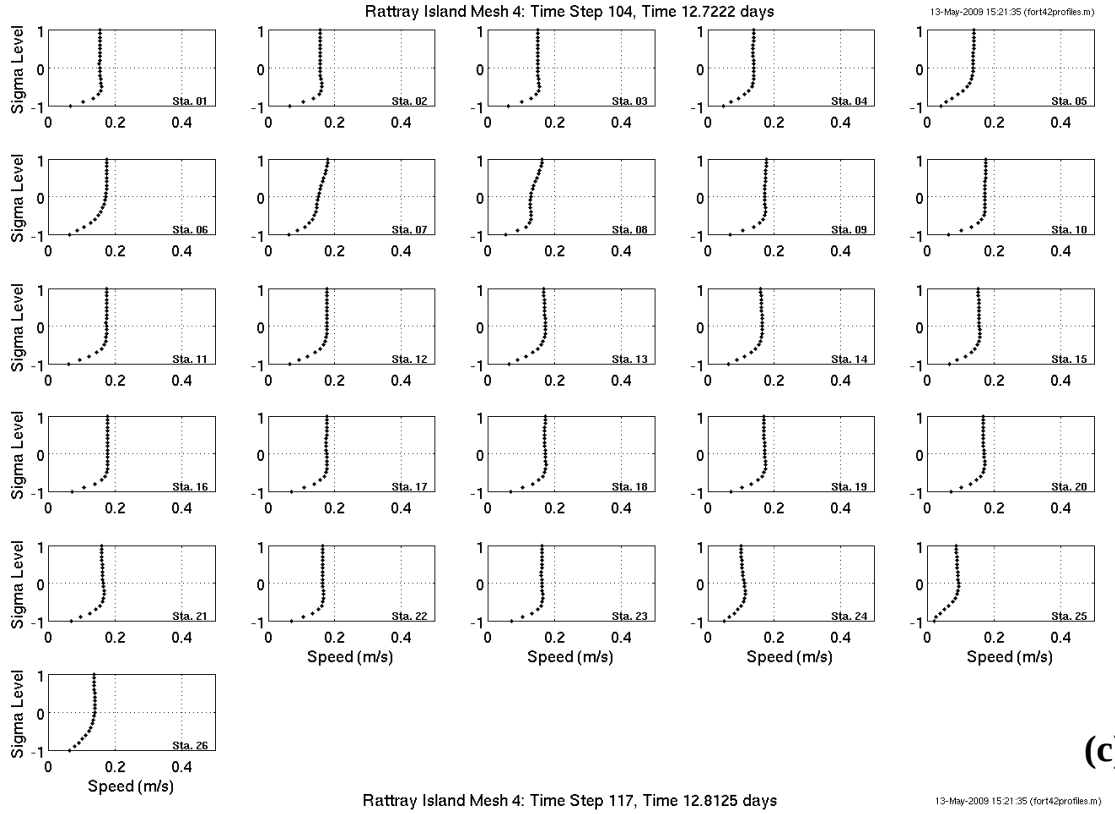

(c)

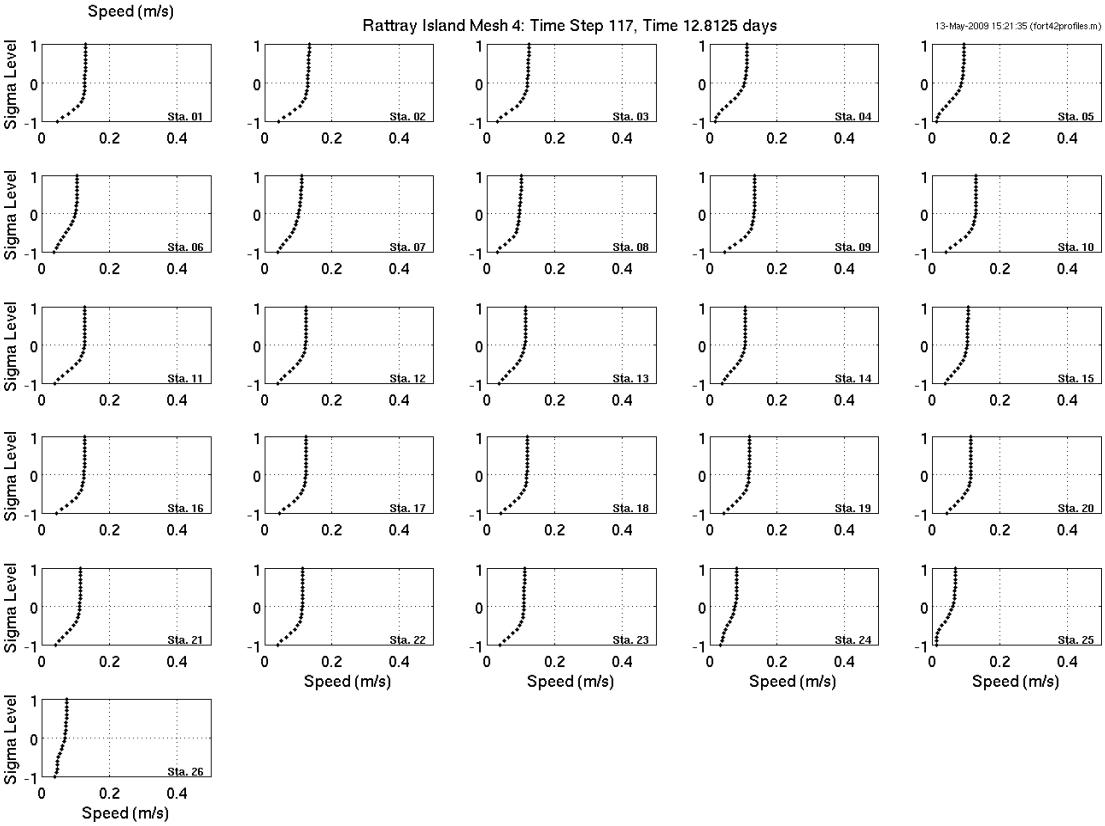

(d)

Figure 6.6 Vertical profiles of the modeled currents at each of the 26 current meter locations on 28 November 1982, (c) 17.3*hrs* and (d) 19.5*hrs*.

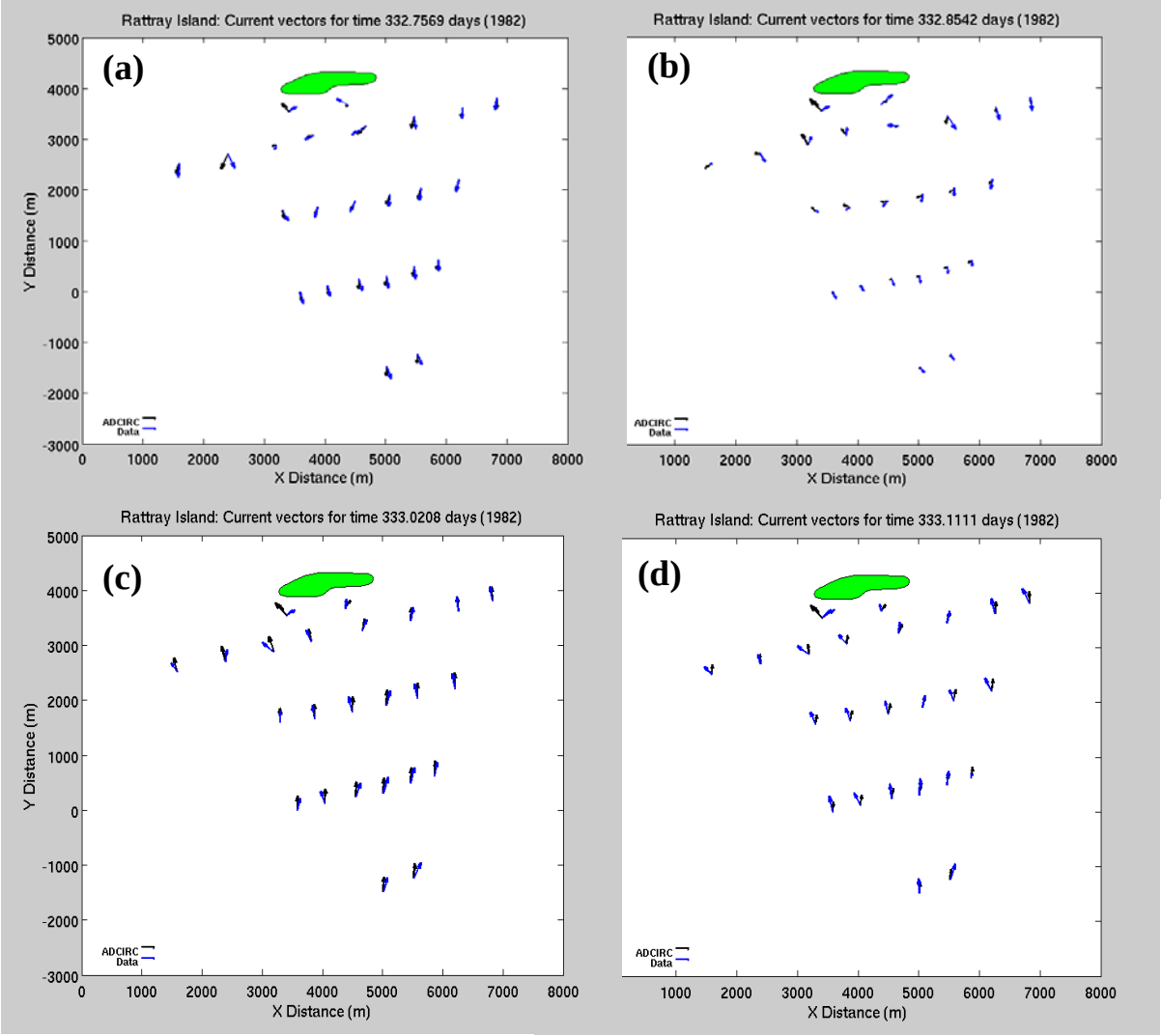

Figure 6.7: Modeled (black) and observed (blue) currents at 26 current meter stations on 28-29 November 1982 at (a) 18.2*hrs*, (b) 20.5*hrs*, (c) 0.5*hrs*, and (d) 2.6*hrs*.

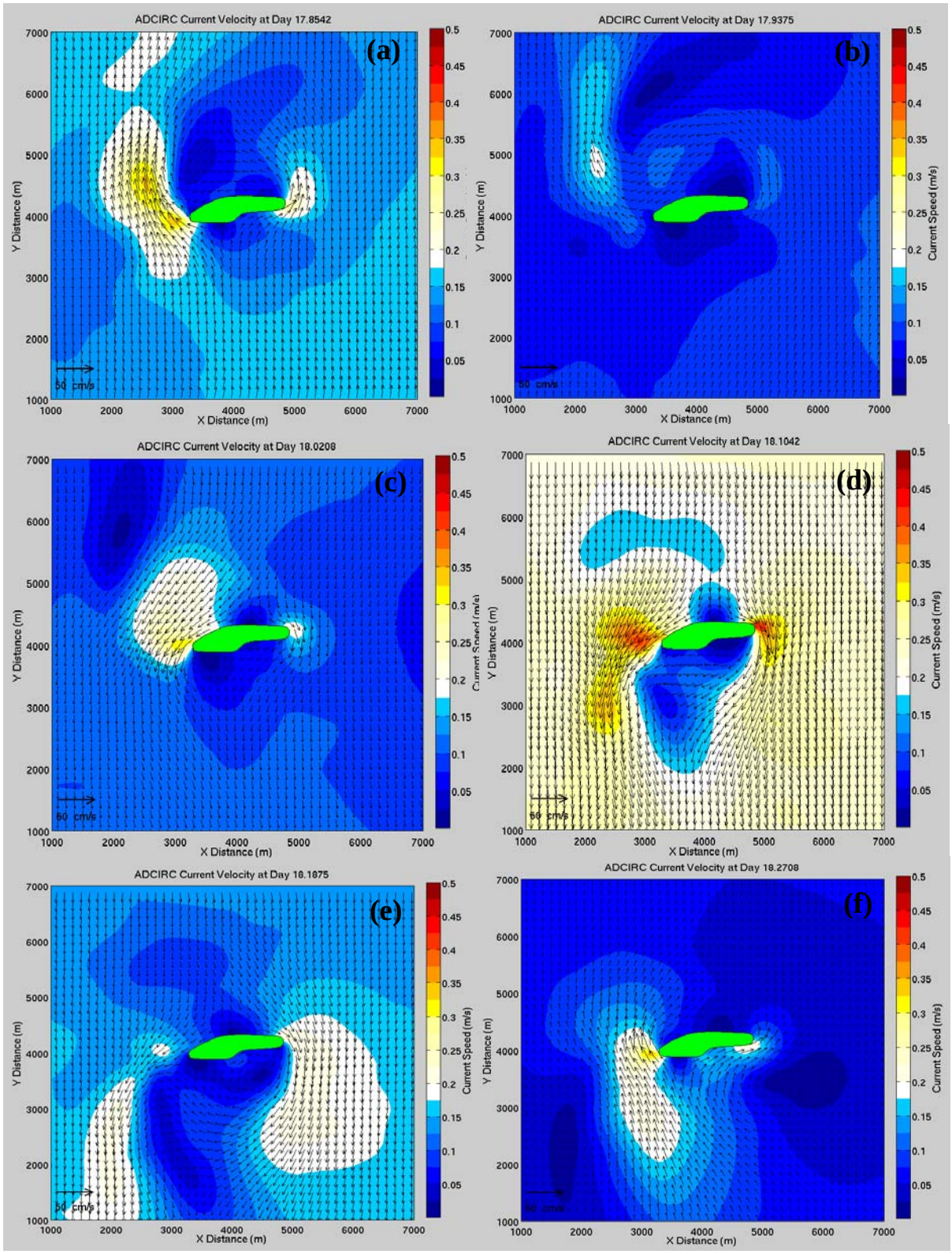

Figure 6.8: Computed currents on 04 December 1982 at (a) 3.6 *hrs*, (b) 5.6 *hrs*, (c) 7.6 *hrs*, (d) 9.6 *hrs*, (e) 11.6*hrs*, and (f) 13.6*hrs*.

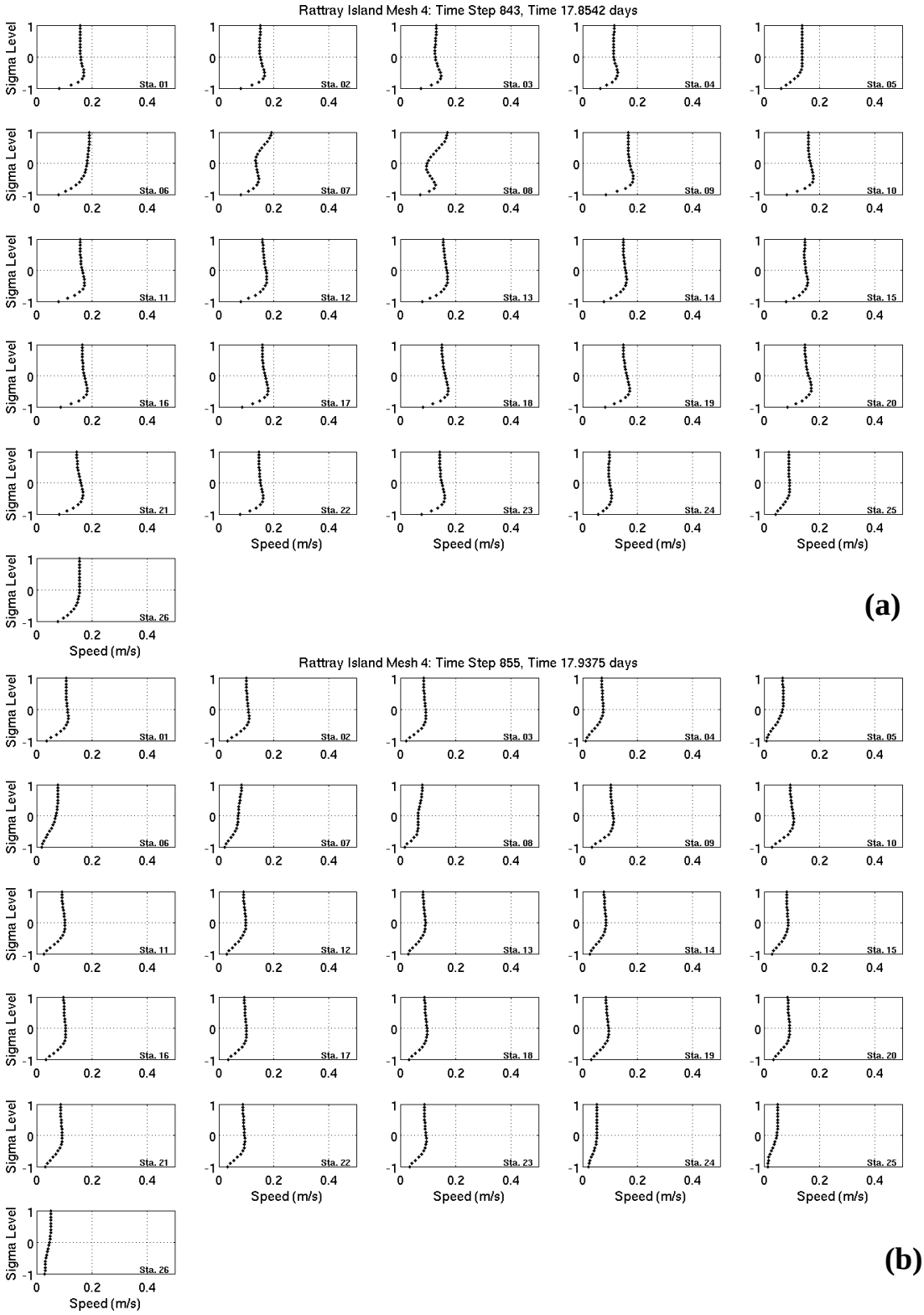

Figure 6.9: Vertical profiles of the modeled currents at each of the 26 current meter locations on 04 December 1982, (a) 3.6 *hrs* and (b) 5.6 *hrs*.

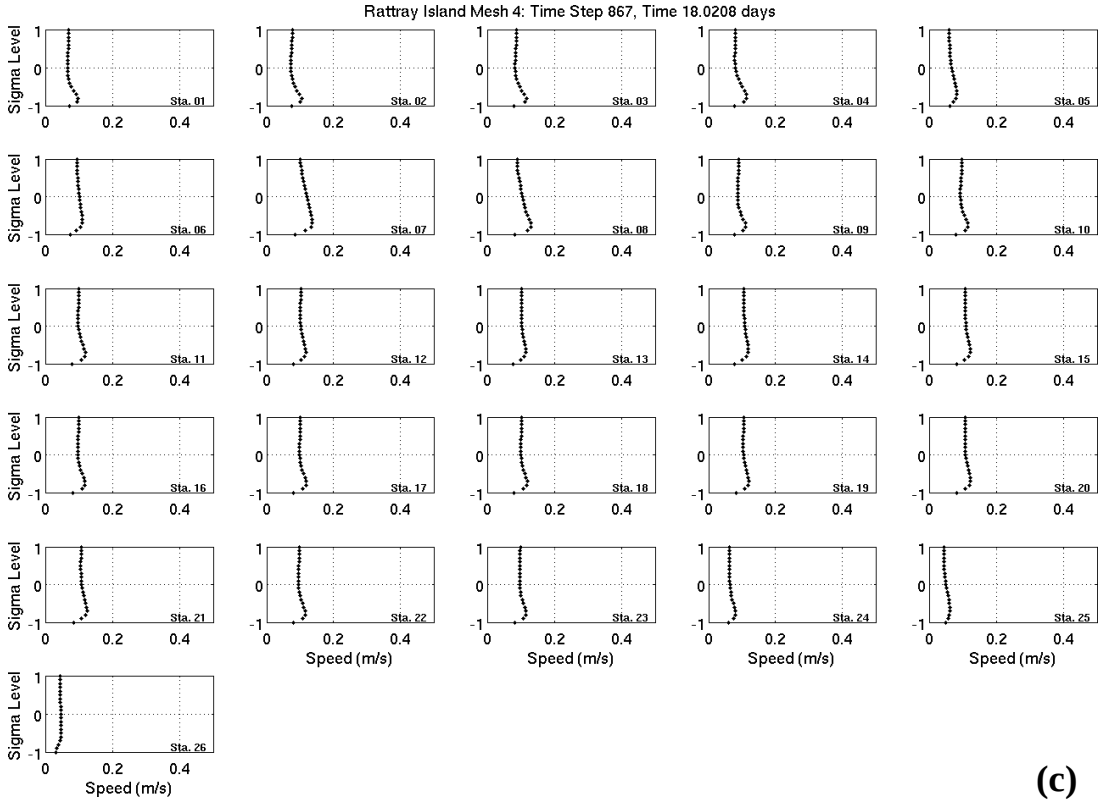

(c)

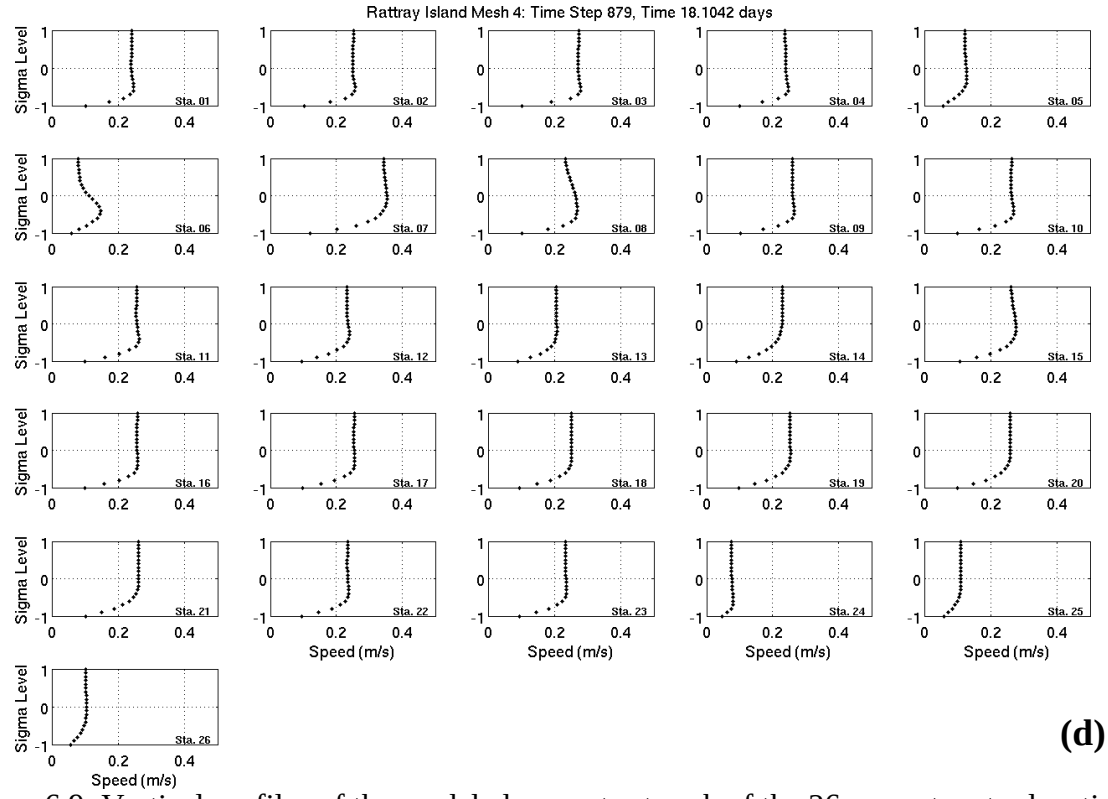

(d)

Figure 6.9: Vertical profiles of the modeled currents at each of the 26 current meter locations on 04 December 1982, (c) 7.6 *hrs* and (d) 9.6 *hrs*.

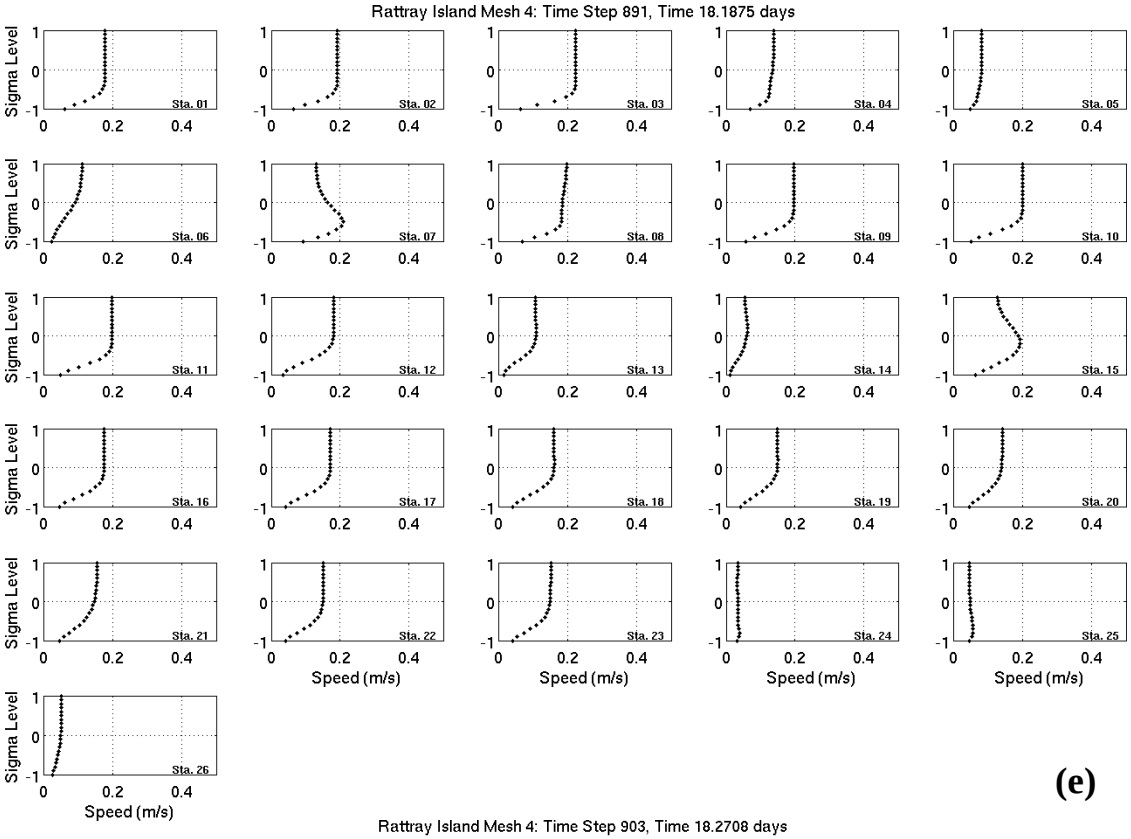

(e)

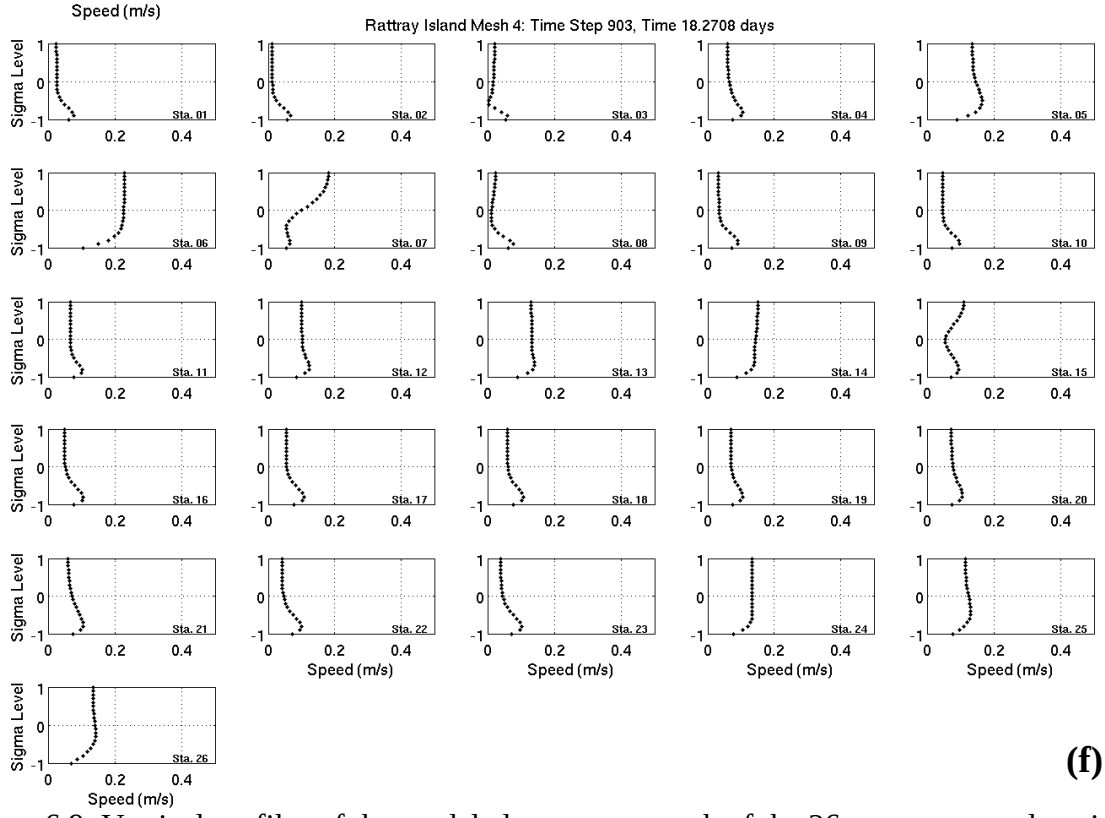

(f)

Figure 6.9: Vertical profiles of the modeled currents at each of the 26 current meter locations on 04 December 1982, (e) 11.6*hrs*, and (f) 13.6*hrs*.

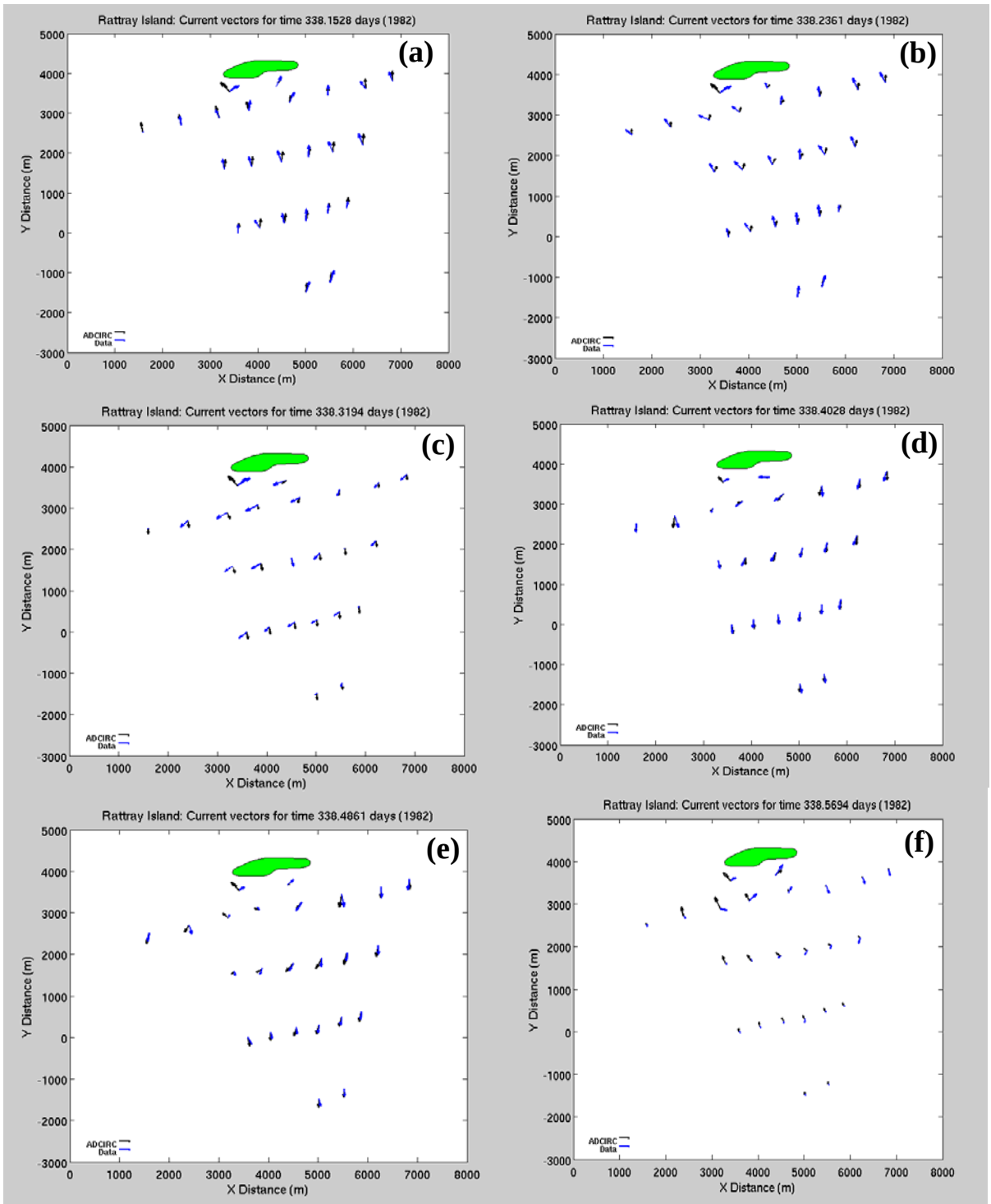

Figure 6.10: Modeled (black) and observed (blue) currents at 26 current meter stations on 04 December 1982 at (a) 3.6 *hrs*, (b) 5.6 *hrs*, (c) 7.6 *hrs*, (d) 9.6 *hrs*, (e) 11.6*hrs*, and (f) 13.6*hrs*.

d. Summary

The application of ADCIRC to the Rattray Island benchmark demonstrates that the model has skill not only in the replication of asymmetric eddy formation in the wake of an island on the rising and falling tide but also the expected vertical structure of the currents. The computed magnitudes of the tide and tidal current were not able to match the observations. This is largely thought to be an artifact of the boundary condition specification of the benchmark itself and especially in the context boundary types available within the ADCIRC model.

To summarize the Rattray Island experience: 1) the selection of boundary forcing data and boundary type is particularly important for small domains, and 2) boundary effects can be minimized by pushing open boundaries away from primary circulation features in such a way that energy can radiate away from the localized region of interest.

While some experimentation was conducted with regard to the form of the 3D turbulence closure and the associated parameter values, a rigorous study was deemed beyond the scope of the present validation testing. It is known however that the model results are sensitive to the bottom friction parameterization and the turbulence closure (vertical eddy viscosity). Recently a significant level of effort has been applied to improve the 3D computations in the model. Recent versions of the code, i.e. v47 and higher, have made bug corrections and systematic improvements to the Mellow-Yamada 2.5 turbulence closure implementation within ADCIRC with the specific goal to make it more robust in shallow water. For example, the turbulent length scale initialization has been modified and new limits defined for the minimum and maximum value of the turbulent length scale. Additional modifications have targeted the bottom drag coefficient calculation.

Lastly, more recent versions of the ADCIRC model, v47 and higher, have available a radiative flux specified boundary condition. This boundary type would likely lead to better model performance for small domain, shallow water problems like Rattray Island.

7. Validation Test Results – Forecasting for MREA07

Sea trials conducted in the shallow Gulf of LaSpezia in collaboration with the NATO Undersea Research Center (NURC) as part of the Marine Rapid Environmental Assessment 2007 (MREA07) provided an opportunity to test and evaluate all aspects of the software under transition to NAVOCEANO as well as the performance of the model predictions themselves. The developed enabling software, MeshGUI, Makef15, and Makef22 were all used to set up a 2D ADCIRC model simulation for the region. Scripting software was then created to run the ADCIRC model in a simulated “real-time” prediction scenario, producing marine environmental forecasts for the two-week period spanning observational cruises in the summer of 2007. Below we describe implementation of the enabling software for the Gulf of La Spezia, define parameters of the “real-time” ADCIRC forecast simulations and compare the model to observations taken as a part of the coastal experiment, POET (Predictive Oceanographic Experimental Trial).

The MREA07 focused on the Gulf of La Spezia located on the eastern side of the Ligurian coast (northwest Italy) (Figure 7.1). Delimited by the Tino and Palmaria islands on the west and by Punta Bianca peninsula on the east, the Gulf is surrounded by mountains. Northwest–southeast oriented, it is 5 km wide while its length is about 10 km. A dam (length of 2.2 km) separates the Gulf in two areas: inside the dam there is the harbor having a mean

depth of about 10–11 m; outside the dam, representing transition to the open sea, is deeper and has an irregular bathymetry. Depth of the Gulf progressively increases in a westward direction: the maximum depth (about 25 m) is in proximity of Palmaria and Tino islands, where the bathymetry becomes very steep. Two passages, at the dam ends, permit exchange between the inside and outside part of the Gulf. The western opening is wider (360 m) and deeper (15–16 m) than the eastern one (180 m width and 11–12 m depth). While the main connection with the open sea is through the Gulf open boundary and the passage between Palmaria and Tino islands, some exchange is also possible through the Portovenere channel (between land and Palmaria island), although the channel is very narrow (150 m wide) and very shallow (the sill depth is 3 m).

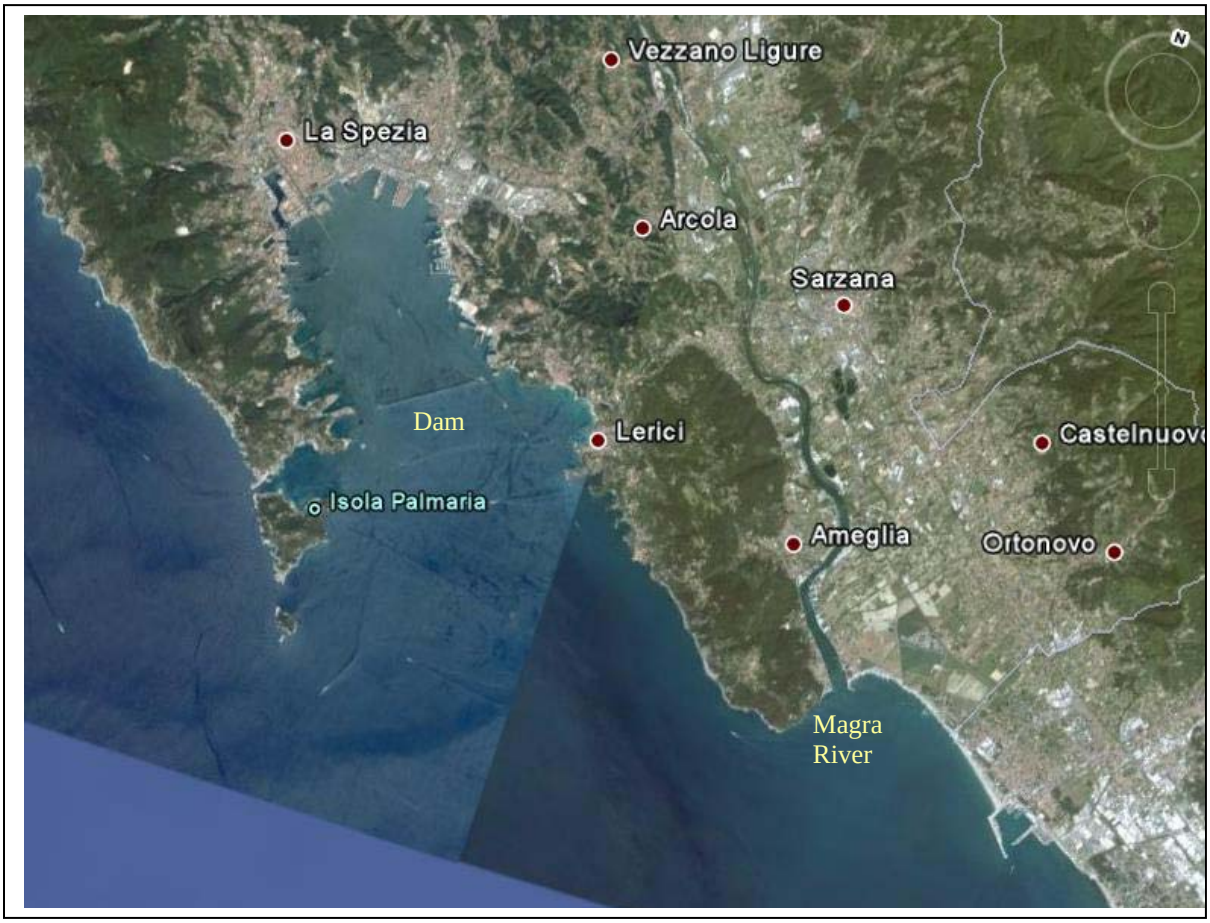

Figure 7.1. A map of the Gulf of La Spezia.

a. Model Configuration

To model the Gulf of La Spezia using ADCIRC, a new unstructured mesh is created using the MeshGUI tool. Required inputs to the MeshGUI tool include an ordered list of coastal outline segments and bathymetry. The coastal outline was extracted from the World Vector Shoreline database (http://rimmer.ngdc.noaa.gov/) and provided by NURC through

the MREA07 collaboration. Bathymetric data is of nominal 3 km resolution and is a sub-sampled composite from Italian and French hydrographic databases, also provided by NURC through the MREA07 collaboration (Figure 7.2). A strategy that places the open ocean boundary away from Gulf of La Spezia coastal waters is used such that the model domain includes all of the offshore and nearshore waters and embayments circumscribed by the seaward boundary and the coastline shown in figure 7.3. Upstream portions of the Magra River were truncated from the mesh to omit extremely shallow depths (less than 1 m) from the modeled region. The westernmost and southern boundaries are configured as a straight line to facilitate the extraction of boundary forcing data from the nested Navy Coastal Ocean Model (NCOM). Other grid generation parameters specified within MeshGUI are the maximum offshore resolution of 200 *km* and the number of refinements, set to 4. The resulting mesh (figure 7.3) has 24,740 nodes and 47,369 triangular elements and spatial resolution ranging from 16 *m* to 181 *m*. This mesh was cast in the form of a fort.14 grid file.

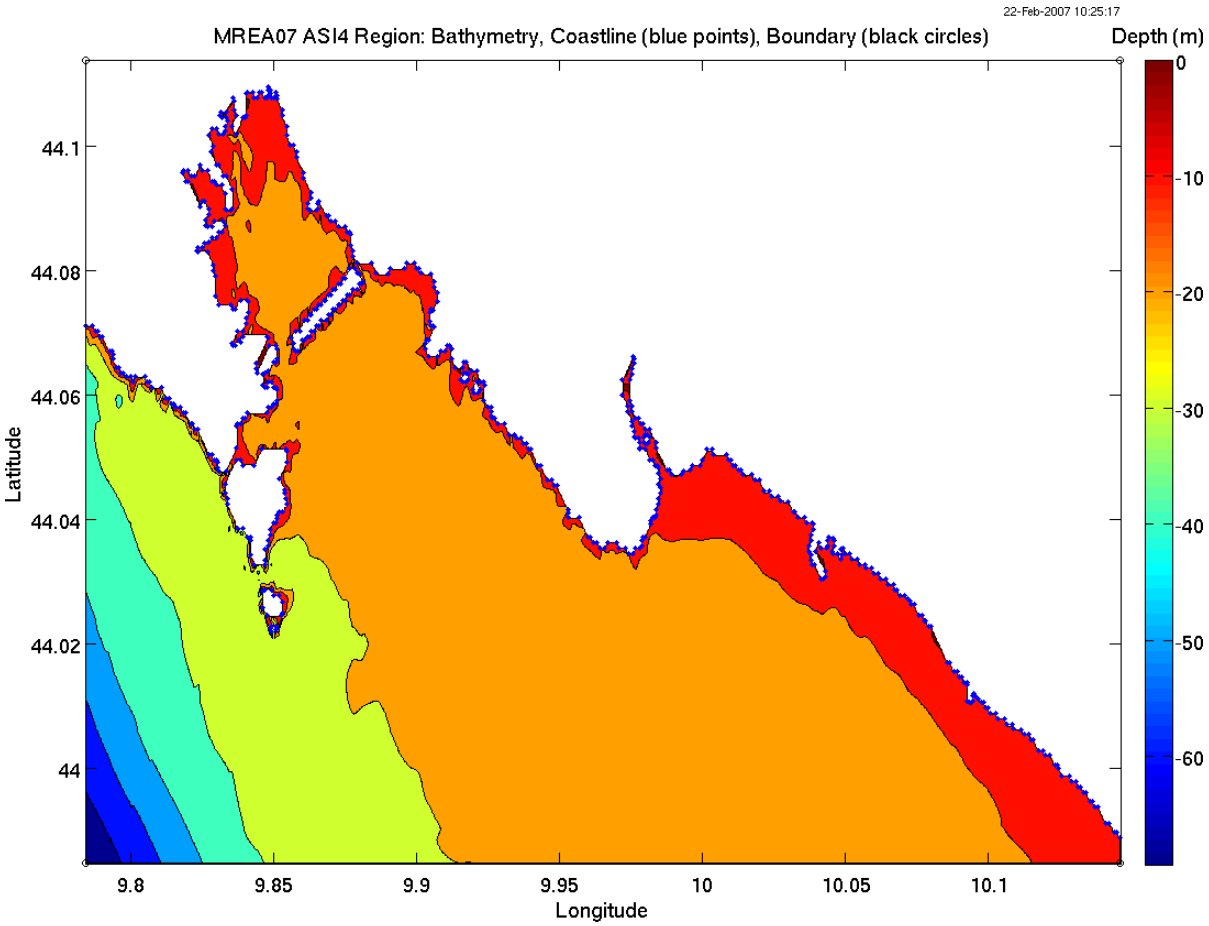

Figure 7.2. Bathymetry contours for the Gulf of La Spezia.

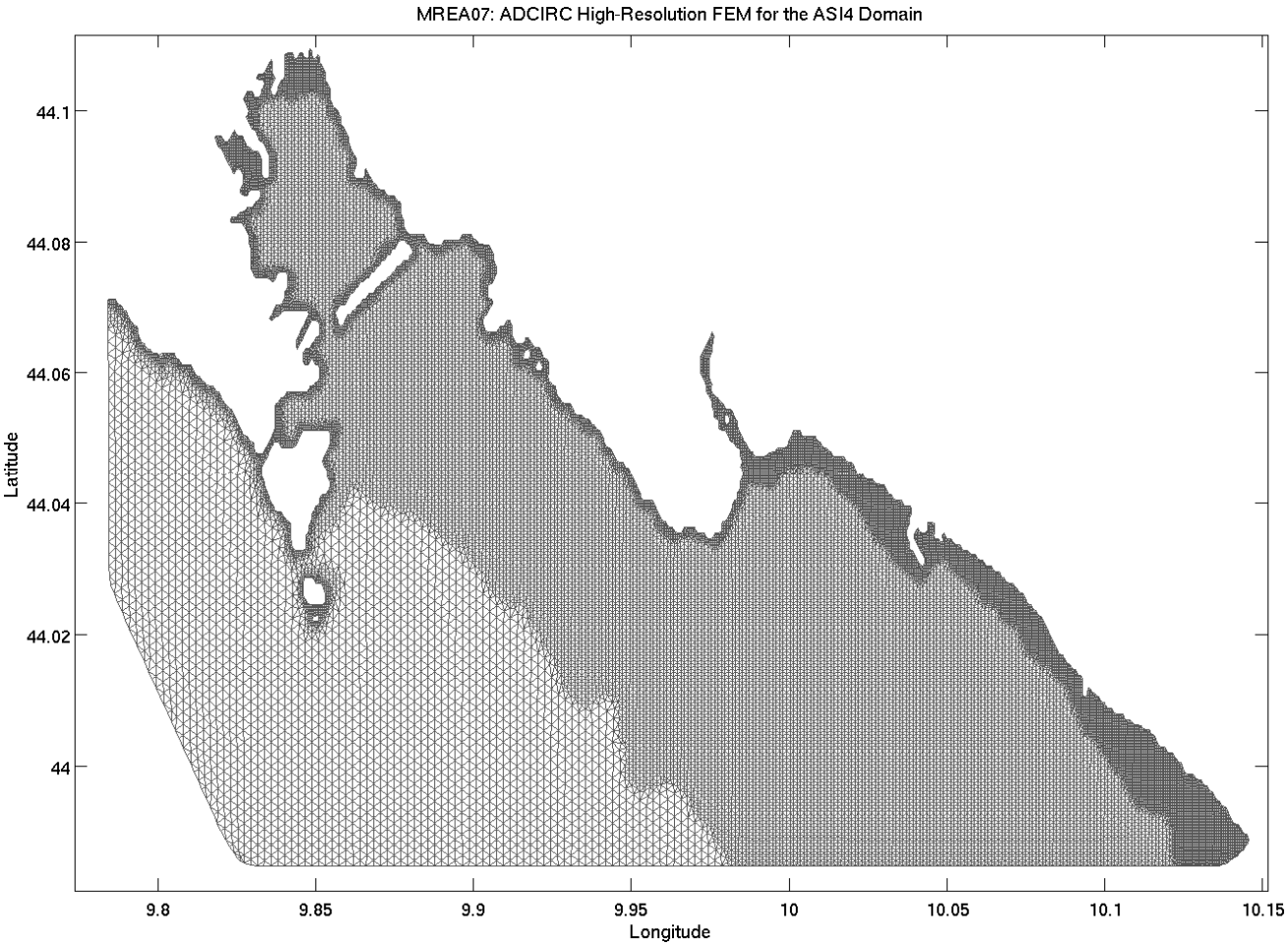

Figure 7.3. The Gulf of La Spezia unstructured mesh created by MeshGUI. Resolution ranges from 16 *m* to 181 *m*.

Determination of the appropriate forcing for the model is the next step. Entering into the model domain are three sources of discharge (figure 7.4), daily outflow from the ENEL power plant equal to 30 m^3/s, the ENEL cooling pump daily discharge, also 30 m^3/s, and the daily climatological average discharge for the Magra River shown in figure 7.5 for June and July. Discharge into the model domain (specified as IBYTPE 22) enters through a fort.20 file which is created outside of the Makef15 GUI. Forcing for the open ocean boundaries as previously mentioned is taken from the innermost 3 *km* nest of a 3-level nested NCOM model of the Ligurian Sea, that includes La Spezia Bay. The nested domains of the NCOM MREA07 implementation are shown in figure 7.6. The NCOM model included surface forcing from heat flux, wind and pressure derived from the Coupled Ocean Atmosphere Mesoscale Prediction System (COAMPS), Europe_2, at 27 km resolution. Tides for the NCOM model are applied at the open water boundaries of the second nest (9 *km*) using values from the Oregon State global tidal database (Egbert and Erofeeva, 2003). Tidal variability for the innermost NCOM model nest is forced only through the NCOM solution of the second nest. Daily surface elevation and U (eastward) and V (northward) current components available at 1-hour intervals are extracted from the NCOM model from the 24-hr hindcast (ADCIRC analysis) and the 48-hr forecast period. NCOM current components

within the uppermost 40 m were depth-averaged to obtain a velocity that was consistent with the 2D version of ADCIRC.

A normal specified flux (IBTYPE = 2) is applied along the southern boundary of the ADCIRC model domain. Along this boundary, NCOM elevation and velocities previously extracted at the NCOM grid points (shown as red squares in figure 7.4) are interpolated onto the nearest neighbor ADCIRC mesh nodes (shown as blue crosses in figure 7.4). Flux values are computed using standard relationships between elevation, velocity, and the normal flux through a segment to obtain the normal flux per unit width in units of m^2/s. Along the western boundary, radiation boundary conditions are selected (IBTYPE = 30) to allow non-modeled energy to exit the domain (no actual forcing values are applied). Figure 7.7 clearly delineates the boundary types specified over the ADCIRC model domain.

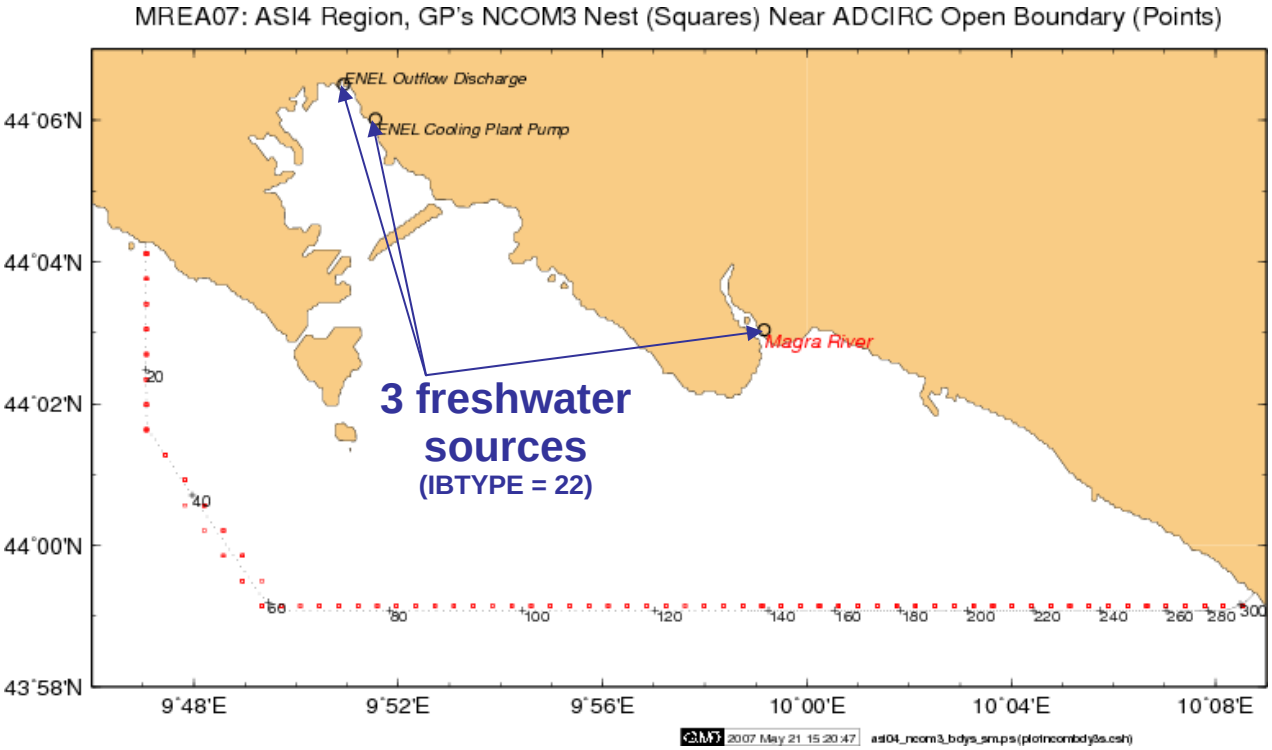

Figure 7.4. Freshwater discharge locations of the ENEL Outflow, the ENEL Cooling Plant Pump, and the Magra River. The ENEL daily discharges are each specified as 30 m^3/s.

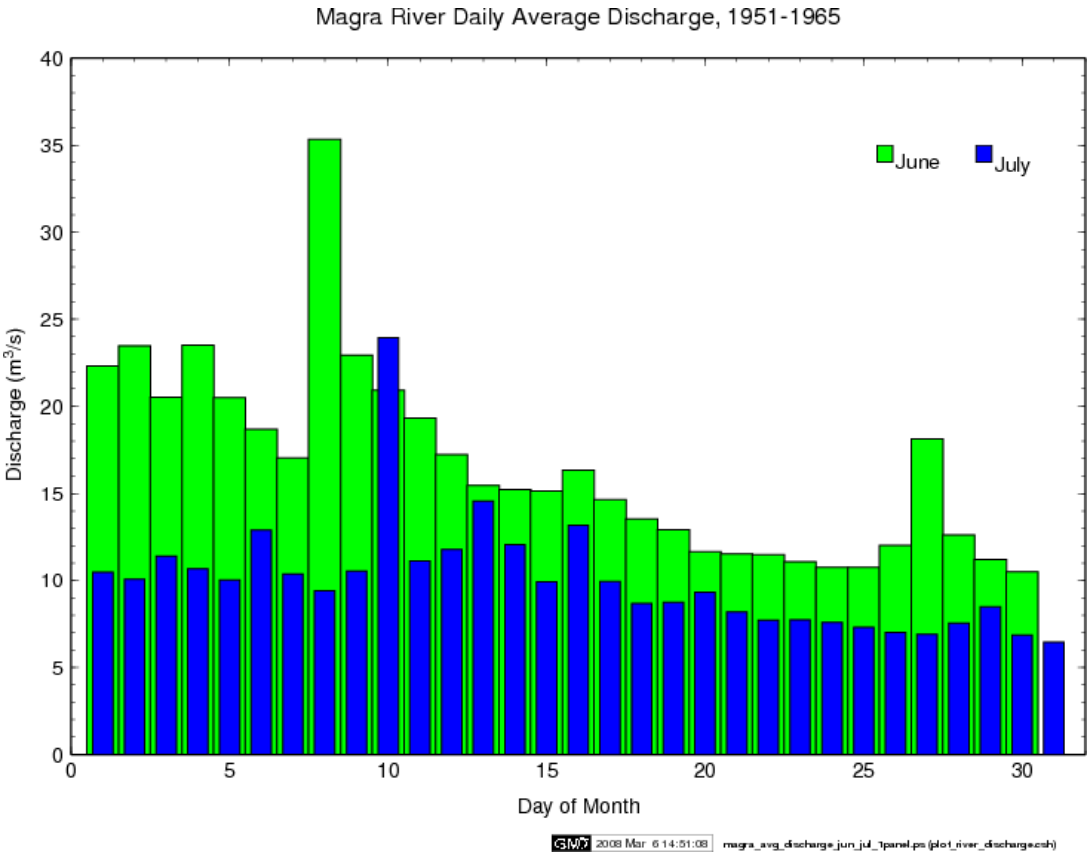

Figure 7.5. Climatological (1951-1965) daily average discharge values for the Magra River during the months of June and July.

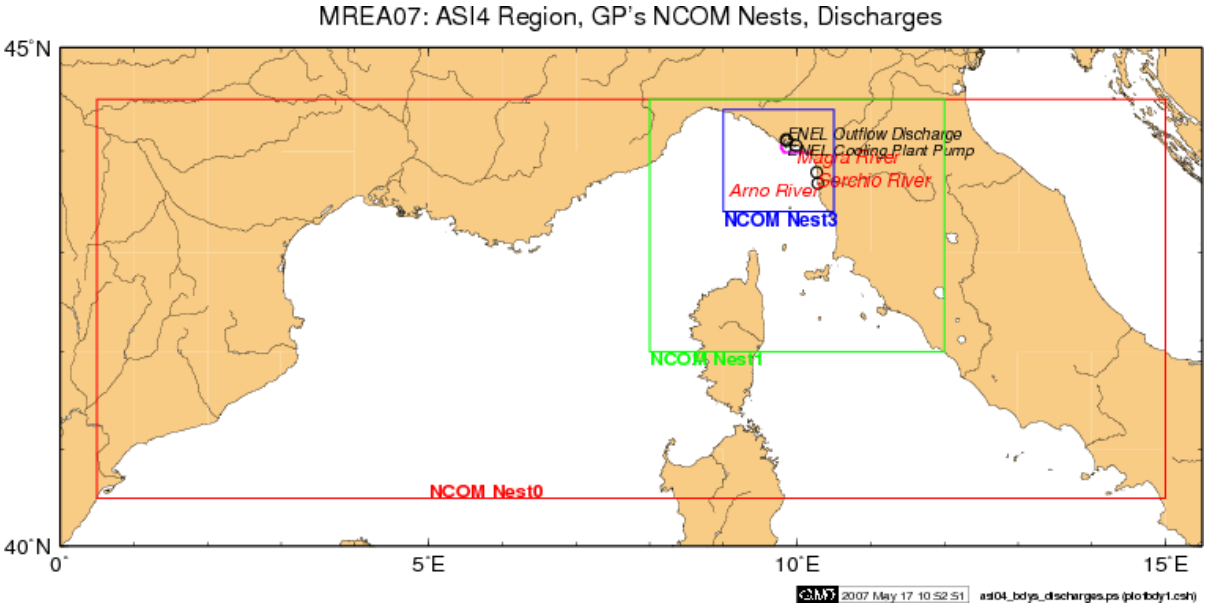

Figure 7.6. NCOM model nests of km (red), km (green) and km (blue) in the Ligurian Sea. Elevation and currents were applied from the NCOM3 nest to the ADCIRC southern boundary.

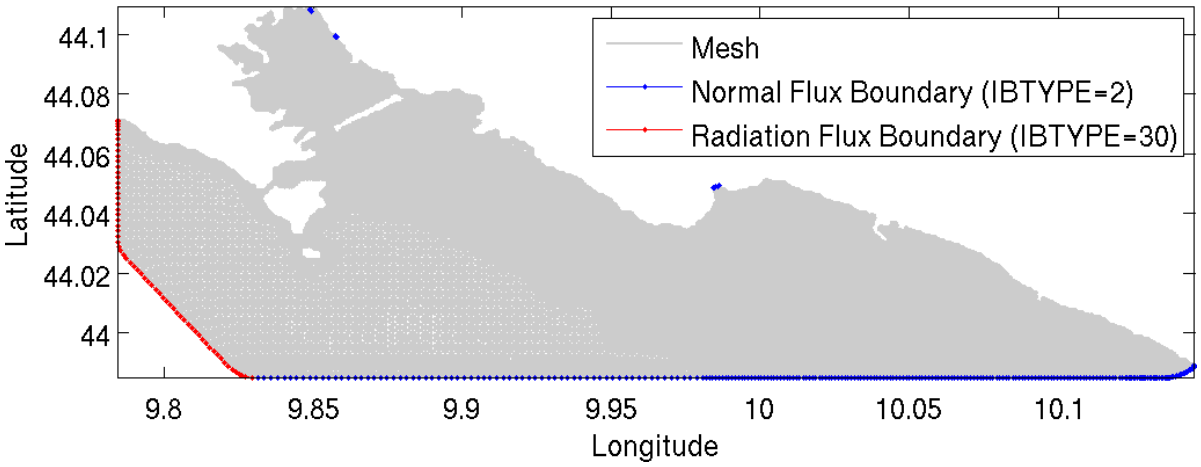

Figure 7.7. Boundary type specifications for the ADCIRC model domain. Radiation conditions (IBTYPE = 30) are depicted in red while the normal flux boundary (IBTYPE = 30) is depicted in blue.

Surface meteorological forcing is applied using the highest resolution products available at the time of the MREA07, the ALADIN products made available to MREA07 collaborators by EPSHOM, the French Navy's Hydrographic and Oceanographic Department. The ALADIN products for mean sea level pressure, wind magnitude, and wind direction have 0.1 degree resolution with the data arriving in two parts: the first part contained hourly forecasts from 1 to 12 hr, and the second contained three-hourly forecasts from 15 to 48 hr (figure 7.8). Note that there was no analysis at 0 hr. The second part of the data set was interpolated to hourly intervals, and a "pseudo analysis" was created by interpolating between the current day's hour 1 forecast and the previous day's hour 23 forecast. In this manner, a data set at each day's 0 hr was created to provide continuous temporal coverage. This continuous time series of ALADIN wind products were processed by the Makef22 software to create the fort.22 meteorological forcing file for the ADCIRC model simulation. The Makef22 utility handed the data read, interpolation of the data from a regular rectangular grid onto the ADCIRC finite element mesh, and export of the interpolated data to a fort.22 formatted file. The ramping of the wind forcing for the initial 15-day ramp-up period is also handled by the Makef22 software.

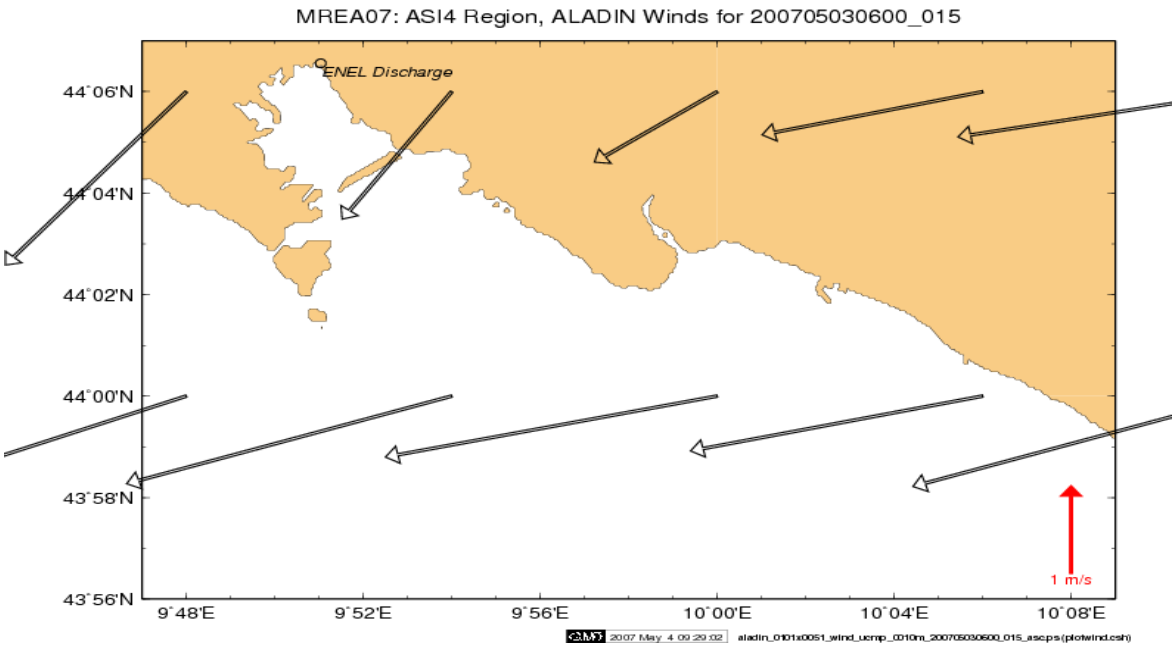

Figure 7.8. ALADIN wind vectors over La Spezia Bay. Resolution is 0.1 degree with an hourly frequency over the first 12 hours and 3-hourly frequency out to 48 hours.

The final step in the preparation of an ADCIRC model simulation is the creation of the parameter and periodic forcing file, fort.15. The Makef15 GUI was applied for this purpose. The default settings in the Makef15 GUI were changed in the following manner:

- Activate the non-fatal error override, NFOVER = 1
- Wetting and drying and the finite amplitude term contributions are disabled, NOLIFA = 0
- Specify a spatially constant Coriolis parameter, NCOR = 0
- Activate tidal potential forcing, NTIP = 1
- Time step is reduced to 1 sec, DTDP = 1.0
- The reference time is set to the time after ramping, REFTIM = 15.0
- The length of simulation is set to 19 days, RNDAY = 17.0
- The ramp period is set to a duration of 15 days, DRAMP = 15.0
- The central projection points are computed for the model domain, SLAM0,SFEA0
- A constant Coriolis factor is computed, CORI = 0.0000252202771
- Assign 1 tidal potential constituent, NTIF = 1
- Tidal potential constituent, TIPOTAG = M2
- Input the date at the start of the simulation to compute the nodal factors (June 1, 2007)
- Select global elevation output, NOUTGE = -1 for 2 days (TOUTSGE = 15.0, TOUFGE = 17.0 model days) every hour (NSPOOLE = 3600)
- Select global velocity output, NOUTGV = -1 for 2 days (TOUTSGV = 15.0, TOUFGV = 17.0 model days) every hour (NSPOOLV = 3600)

- Output a hotstart at the 24th hour of the forecast period, NHSTAR = 1, NHSINC = 1378800 (model day = 15.958333)

All of the needed input files for an ADCIRC model simulation are described, fort.14, fort.15, fort.20, and fort.22. To summarize, the model configuration will produce water levels and 2D currents subject to surface wind and pressure forcing, discharge from two locations at the ENEL power plant as well as the Magra River, and offshore oceanic forcing represented by the NCOM model solution. Tidal potential forcing within the ADCIRC domain is also included and Coriolis effects remain constant over the domain. The only nonlinearity activated in the model is the bottom stress term. The predictive forecast system configured using these input files is outlined in the next section.

b. Predictive System

The objective of the MREA07 model forecast system was to generate 48 hour forecasts of elevation and 2D currents for the Gulf of La Spezia over the period 18 June 2007 to 1 July 2007. To do this an initial model run was conducted to spin-up the tidal solution within the domain. As mentioned in the previous section, this run started on 1 June 2007 applying a hyperbolic ramp function that lasted for 15 days. After ramping a 2-day forecast begins. At the 23rd hour of the forecast period a model solution is written as a hotstart file (fort.67) (model day 15.9583333). This field is used to initialize the next day 48-hour forecast. Each subsequent forecast run includes one hour prior to forecast to allow the interpolation and application of the analysis ALADIN wind and pressure fields valid 1 hour into the forecast. This out-of-sync timing of the meteorological forcing requires that the model fields be output prior to the start of the forecast during a time which had valid meteorological forcing, i.e. 1 hour before the start of a forecast run. Linear interpolation between the 23rd hour of the previous day forecast and 1 hour into the current day forecast result in a seamless application of the meteorological forcing. These 2-day + 1 hour model simulations continue through the 1th of July 2007, the time at which NCOM model availability ceased.

For successive model forecast runs, the following parameters in the fort.15 files were changed via a script:

- The length of simulation is incremented by 1, RNDAY = RNDAY+1
- Times for global elevation output are incremented by 1, TOUTSGE = TOUTSGE+1, TOUTFGE = TOUTFGE+1
- Times for global velocity output are incremented by 1, TOUTSGV = TOUTSGV+1, TOUTFGV = TOUTFGV+1
- Timestep for hotstart file generation is incremented by 1 day or NHSINC = NHSINC + 86400 (no. of timesteps per day)

The 49-hour forecast ADCIRC model simulation was executed in parallel on 5 AMD dual-core Opterons, model 252, having a single-core speed of 2.6 GHz. The wallclock time for a single forecast run was 1 hr 15 min on average. This amounts to 0.00255 CPU sec per time step per processor for this 24,740 node grid model.

c. 2D Currents

As part of the Predictive Oceanographic Environmental Trial (POET) a vessel mounted RDI 300 kHz ADCP was used to collect data along the water column in the external part of the Gulf, along five tracks (figure 7.9). The ADCP cell size was 1 m and the sampling rate was 15-sec. Ten minute positions along the ADCP tracks are shown as red circles in figure 7.9. No detiding procedure has been applied due to the smallness of tidal signal. The cruise began on at 13:23 GMT in the north western corner. A zigzag track was followed to maximize spatial coverage until ending nearly 3 ½ hours later at 16:48 GMT in the south east corner waters bounded by Tino Island to the west and the Punta Bianca peninsula to the east.

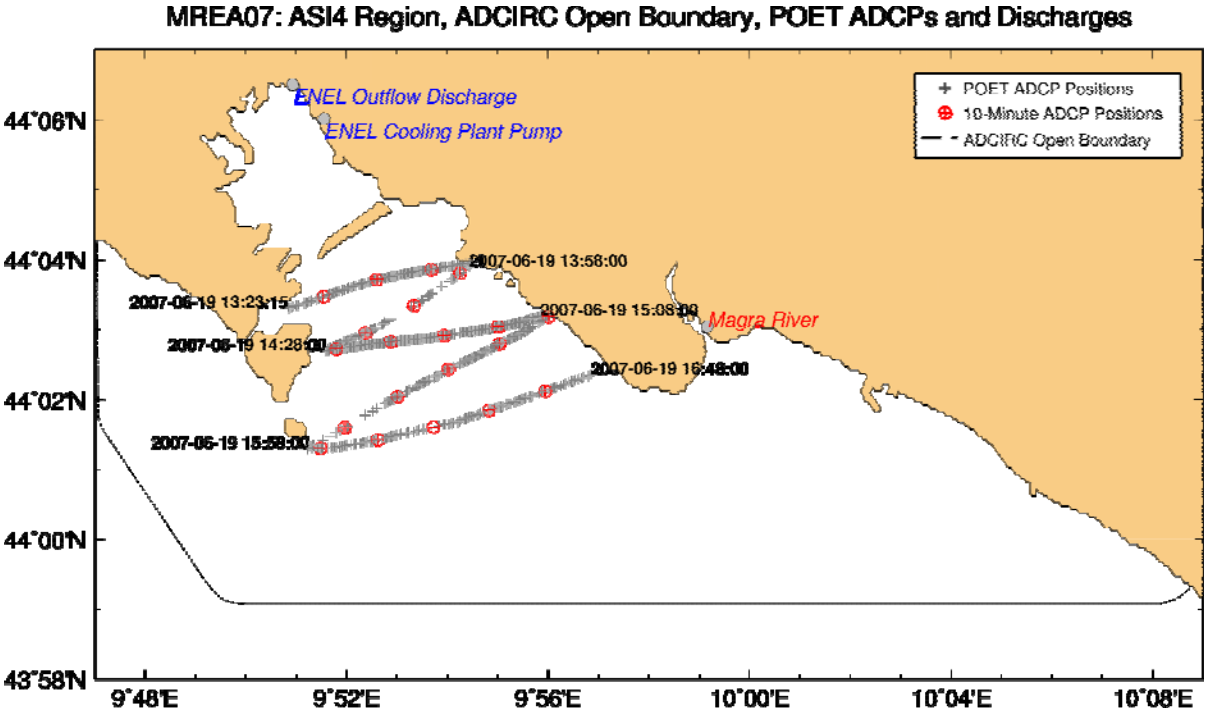

Figure 7.9. Map of the ADCP tracks from the POET experiment on 19 Jun 2007. Red circles indicate 10-minute intervals.

Data drop outs ranged from 30 sec to 4 min 15 sec with 139 data gaps greater than 15 sec. To perform meaningful model-data comparisons using such data it was necessary to first perform a time interpolation on the data. A ½ hour moving average was applied to smooth the data to better match the hourly frequency of the model output. Lastly, the current observations were depth-averaged so that direct comparisons with the 2D ADCIRC modeled currents could be made. This processing of the U and V components of the current observations is shown in figure 7.10 where the interpolated data is depicted by red lines and the ½ hour averaged data is displayed in blue.

The magnitude and direction as well as U and V components of the ADCIRC currents (red) are compared to the observed currents (blue) as shown in figures 7.11. The computed differences are plotted on the same graphs in black with the magnitudes indicated

on the right-hand scale. The trend exhibited by the observations in both current magnitude and by component is closely followed by the modeled values. Some variability of the observations is not captured by the 1-hour frequency of the model data. Statistical representation of the model-data error is provided by figure 7.12. The model-data correlation with respect to current magnitude is over 0.97 while the U and V component correlation values are 0.94 and 0.92, respectively. The largest error clearly enters through the modeled current direction which is inversely related and largely un correlated to observations. From the time series of direction in figure 7.13, most of the directional error occurs during the first two, northernmost legs of the ADCP transects.

Comparisons of the ALADIN wind speed, direction and air pressure to the ENEA meteorological station data (figure 7.14) clearly indicate that the wind directions produced by the ALADIN model are not realistic. The ENEA meterological station is located along the eastern shoreline across from the dam. The wind field error would be cause for significant error in the modeled currents. Note also that the two northernmost ADCP segments would be using the ALADIN winds that are coming from the land while remaining three southernmost ADCP segments would be using ALADIN wind values that were computed over the water. This is a consequence of the rather coarse resolution of the ALADIN winds for the shallow coastal region under study.

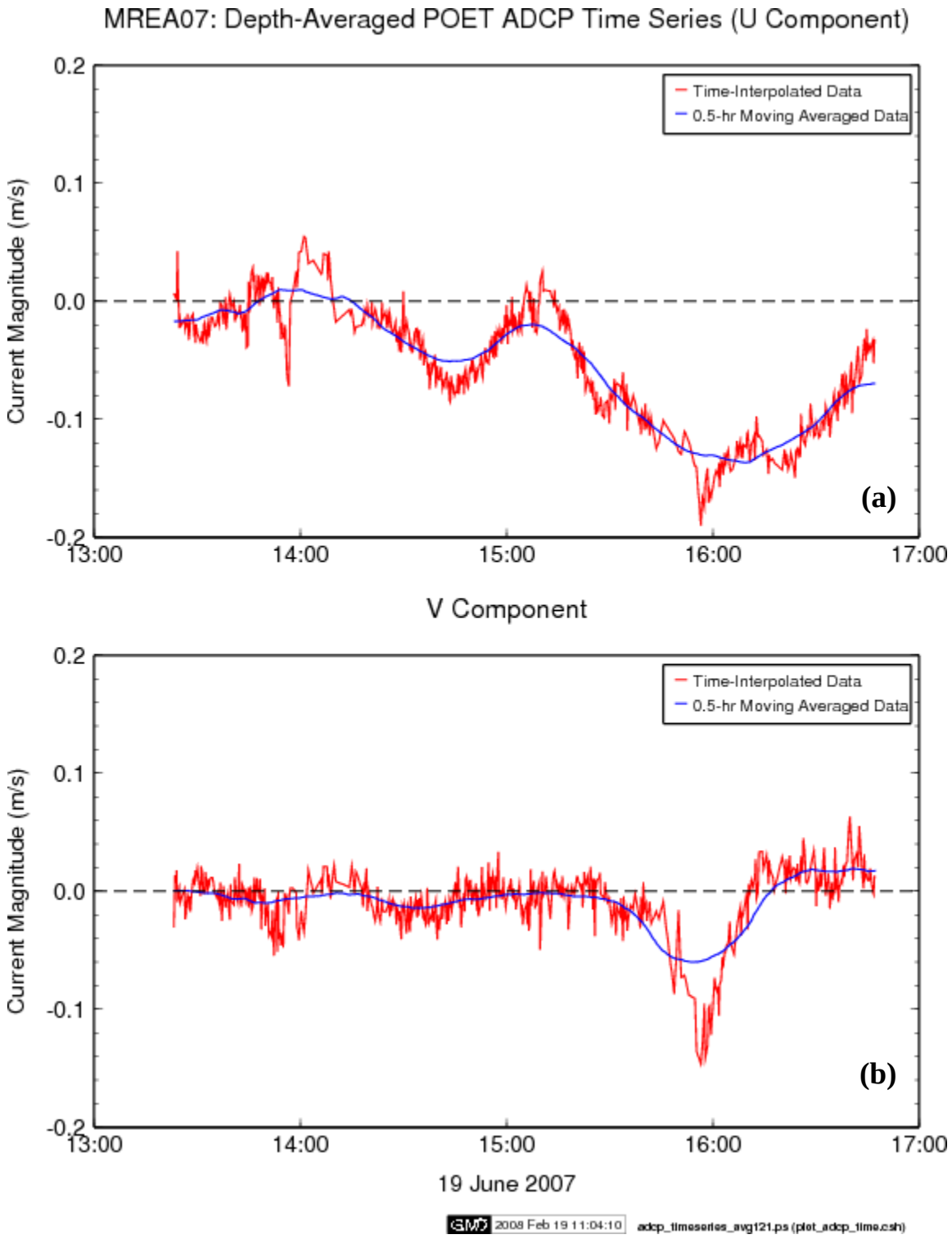

Figure 7.10. Time-interpolated (a) U and (b) V components of the current observations (red) and the ½ hour moving averaged data (blue).

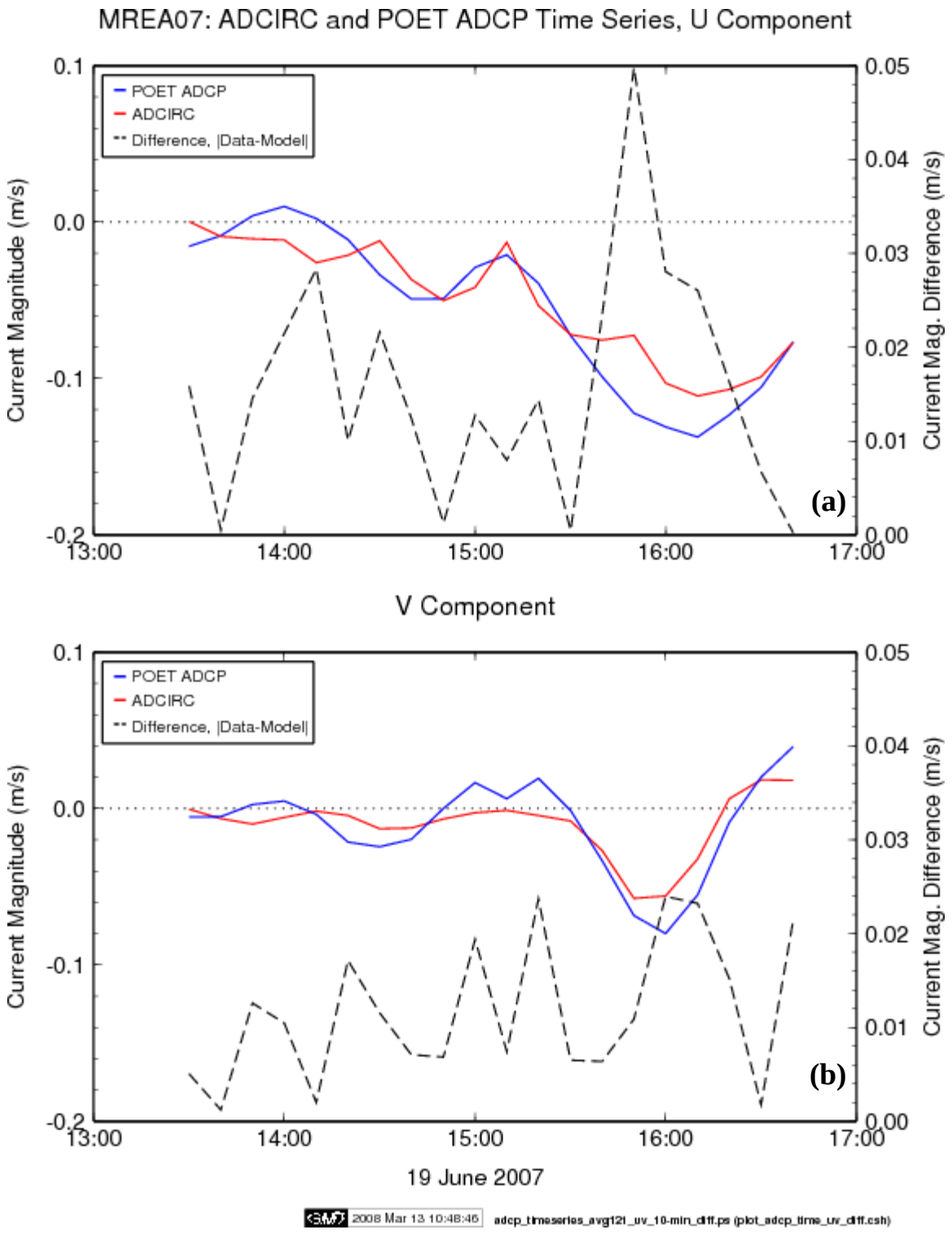

Figure 7.11. Modeled (red) and observed (a) U and (b) V components of the current; the difference is shown in black (right-hand scale).

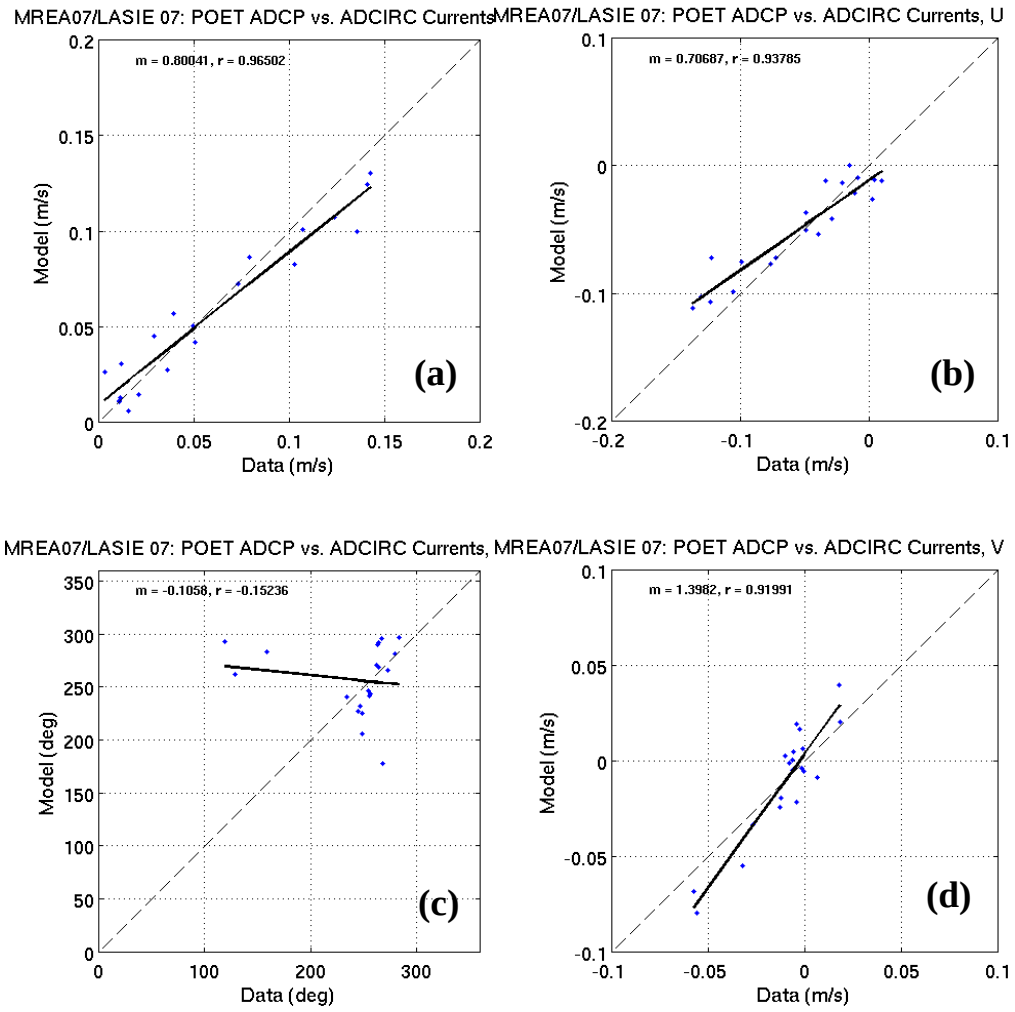

Figure 7.12. Model vs. observed currents (a) magnitude, (b) U component, (c) direction, and (d) V component of the current; correlations are given in the upper left of each panel.

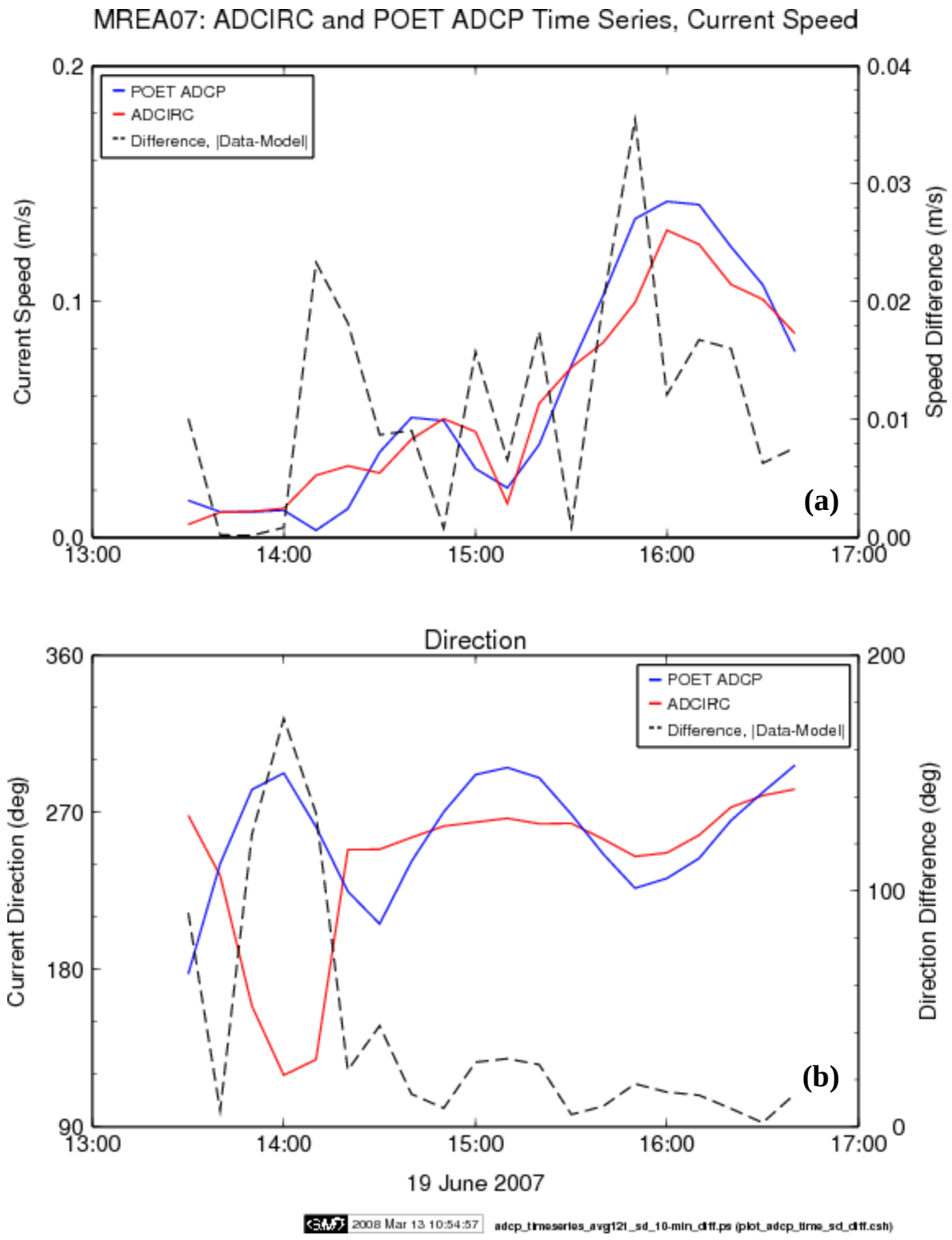

Figure 7.13. Modeled (red) and observed (a) speed and (b) direction of the current; the difference is shown in black (right-hand scale).

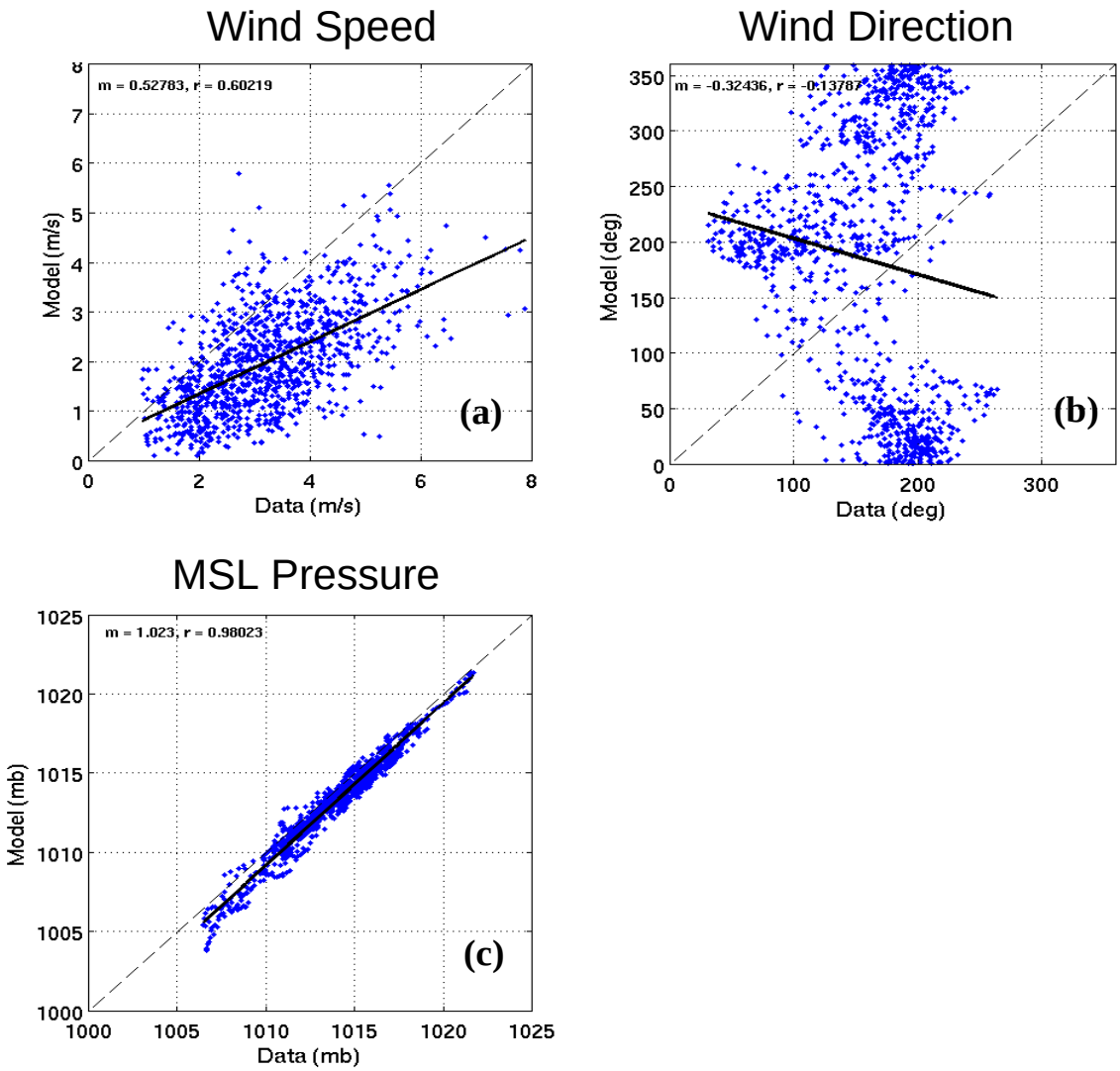

Figure 7.14. Model vs. observed winds (a) speed, (b) direction, and (c) mean sea level pressure; correlations are given in the upper left of each panel.

d. Summary

The MREA07 exercise provided an opportunity to demonstrate application of the enabling software, MeshGUI, Makef15, and Makef22, to set-up the ADCIRC model for a new geographical region. The finite element mesh and the associated grid file, fort.14, were created, as well as the model parameter and periodic forcing file, fort.15 and the meteorological forcing file, fort.22. The model once configured was run in a forecast mode for two weeks in June, 2007 with forcing applied from real-time meteorological model (ALADIN) and regional oceanic products (NCOM). Model-data comparisons for 2D currents collected from an ADCP survey lend confidence to the modeled currents and highlight their sensitivity to the surface wind forcing.

8. References

Blain, C. A., 1997. Development of a data sampling strategy for semi-enclosed seas using shallow water model, *J. Atm. Oceanic. Tech.,* 14, 1157-1173.

Blain, C. A., R. H. Preller, and A. P. Rivera, 2002. Tidal Prediction using the Advanced Circulation Model (ADCIRC) and a Relocateable PC-based System. *Oceanography*, 15(1), 77-87.

Blain, C. A., J.J. Westerink, R. A. Luettich, 1994. The influence of domain size on the response characteristics of a hurricane storm surge model. J. Geophys. Res., 99, 18467-18479.

Blaise, S., and L. White, 2006. Development of a marine modelling benchmark: tidal circulation around Rattray Island. *Second-generation Louvain-la-Neuve Ice-ocean Model*, Universite Catholique de Louvain, http://www.climate.be/SLIM/Benchmarks

Dietrich, J.C., R.L. Kolar and R. A. Luettich, 2004. Assessment of ADCIRC's Wetting and Drying Algorithm, *Proceedings of the XV International Conference on Computational Methods in Water Resources,* Miller, C.; Farthing, M.; Gray, W., and Pinder, G. *(ed.), 2*, 1767-177.

Dietrich, J.C., R. L. Kolar, and Westerink, J.J., 2006. Refinements in Continuous Galerkin Wetting and Drying Algorithms, *Estuarine and Coastal Modeling,* Spaulding, M. *(ed.)*, *ASCE,* 637-65.

Dresback, K.M. and Randall L. Kolar, 2001. Implicit time-marching algorithm for shallow water models based on the generalized wave continuity equation, *Int. J. Numer. Meth. Fluids*, 36, 925–945.

Dresback, K.M, Randall L. Kolar and J. Casey Dietrich, 2004. A 2D implicit time-marching algorithm for shallow water models based on the generalized wave continuity equation, *Int. J. Numer. Meth. Fluids*, 45, 253–274 (DOI: 10.1002/_d.697).

Egbert, G.D., and S.Y. Erofeeva, 2003. Efficient inverse modeling of barotropic ocean tides. *J. Atmos. Oceanic Tech*., 19, 183-204.

FEMA, 2006. Louisiana Hurricane Katrina Surge Inundation and Advisory Base Flood Elevation Map Panel Overview, Federal Emergency Management Agency, January, 2006.

FEMA, 2005. Mississippi Hurricane Katrina Surge Inundation and Advisory Base Flood Elevation Map Panel Overview, Federal Emergency Management Agency, November, 2005.

Feyen, J.C. and Z. Yang, 2007. Generation of Synoptic Water Level and Depth-Averaged Velocity Time Series on the Delaware Bay for Use in Model Coupling, In *Proceedings of the 10th International Conference on Estuarine and Coastal Modeling*, 339-357.

Holland, G., 1980: An analytic model of the wind and pressure profiles in hurricanes. *Mon. Wea. Rev.,* 108, 1212-1218.

Kapolnai, A., F. Werner, and J. Blanton, 1996. Circulation, Mixing, and Exchange Processes in the Vicinity of Tidal Inlets: A Numerical Study, *Journal of Geophysical Research,* 101, 14253-14268.

Kinnmark, I.,1986. The Shallow Water Wave Equations: Forumulations, Analysis and Application, *Springer-Verlag, 15*, 18.

Kolar, R.L., J.P.Looper, J.J. Westerink, and W.G. Gray, 1998. An improved time marching algorithm for GWC shallow water models, In *CMWR XII Volume 2: Computational Methods in Surface Flow and Transport Problems*, Burganos VNI, Karatzas GP, Payatakes AC, Brebbia CA, Gray WG, and Pinder, GF (eds), Computational Mechanics Publications: Southampton, 379–385.

Lefevre, F., F. H. Lyard, C. Le Provost, E.J.O. Schrama, 2002. FES99: A Global Tide Finite Element Solution Assimilating Tide Gauge and Altimetric Information, *Journal of Atmospheric and Oceanic Technology,* 19, 1345-1356.

Luettich, R.A. and J.J. Westerink, 1995. An Assessment of Flooding and Drying Techniques for Use in the ADCIRC Hydromdynamic Model: Implementation and Performance in One-Dimensional Flows, *U.S. Army Engineers Waterways Experiment Station.*

Luettich, R.A. and J.J. Westerink, 1999. Elemental Wetting and Drying in the ADCIRC Hydrodynamic Model: Upgrades and Documentation for ADCIRC Version 34.XX
U.S. Army Engineers Waterways Experiment Station.

Powell, M.D., S.H. Houston, L.R.Amat, and N. Morisseau-Leroy, 1998: The HRD real-time hurricane wind analysis system. *J. Wind Engineer. and Indust. Aerodyn.* 77 & 78, 53-64.

Veeramony, J. and Blain, C. A., 2001. Barotropic Flow in the vicinity of an idealized inlet: Simulations using the ADCIRC model, *Naval Research Laboratory,* NRL/FR/7320-01-9977, *Department of the Navy*, March 9, 2001.

Walters, R.A., 1997. A model study of tidal and residual flow in Delaware Bay and River, *J. of Geophysical Res.*, 102, 12689-12704.

Westerink, J.J., R.A. Luettich , J.C. Feyen, J.H. Atkinson, , C. Dawson, H.J. Roberts, M.D. Powell, J.P. Dunion, E.J. Kubatko, H. Pourtaheri, "A Basin to Channel Scale Unstructured Grid Hurricane Storm Surge Model Applied to Southern Louisiana," *Monthly Weather Review*, 136, 3, 833-864, 2008.

White, L., E. Deleersnijder, and V. Legat, 2008. A three-dimensional unstructured mesh finite element shallow-water model, with application to the flows around an island and in a wind-driven, elongated basin, *Ocean Modeling*, 22, 26-47.

Wolanski, E., Imberger, J., Heron, M., 1984. Island wakes in shallow waters, *Journal of Geophysical Research*, 89 (C6), 10553–10569.

Xie, L., L. Pietrafesa, and M. Peng, 2004. Incorporation of a mass-conserving inundation scheme into a three dimensional storm surge model, *Journal of Coastal Research, 20*, 1209-1223.